THERMODYNAMIC STUDIES OF MINERALS UNDER MANTLE CONDITIONS

by

Wenjun Yong

A dissertation submitted in partial fulfillment
of the requirements for the degree of
Doctor of Philosophy
(Geology)
in The University of Michigan
2008

Doctoral Committee:

Professor Eric J. Essene, Chair
Professor Rodney C. Ewing
Professor Anthony H. Francis
Professor Youxue Zhang

2008

To Ying and our families

ACKNOWLEDGMENTS

I would like to express my sincere gratitude to my advisor, Eric J. Essene, for his intellectual guidance and financial support throughout my Ph. D study at the University of Michigan. I have benefited a lot from his broad knowledge and scientific spirit, which as I can foresee, will continue to influence me in my future academic career. I would also like to thank my former and present committee members: Youxue Zhang, Rod Ewing, Lars Stixrude and Anthony Francis for their constructive comments on the manuscripts presented in this thesis. Special thanks go to Youxue for offering me such a wonderful opportunity to pursue my Ph.D at University of Michigan.

I am grateful to Tony Withers from University of Minnesota. Not only did he teach me how to use these high pressure facilities, but also his enthusiasm made me really love and enjoy doing experiments. Marc Hirschmann is also greatly appreciated for his generosity to let me use his high pressure lab at University of Minnesota. I would like to thank Edgar Dachs from University of Salzburg for his cooperation in measuring the low-temperature heat capacity data.

I would like to thank all the other people who have contributed to my dissertation in various ways. Carl Henderson, Yang Chen, Roland Rouse, Lixing Jin, Ni Sun, Katie Davis and Fuxiang Zhang helped me on the analytical techniques required for sample characterization, such as EMPA, SEM, XRD and Raman. Zhengjiu Xu and Qiong Liu helped me on the glass synthesis process. Tony Withers, Cyril Aubaud, Emily Baxter, Shushu Chen and Lauren Larkin are all appreciated for their great hospitality during my

visits to Minneapolis.

My officemates and classmates, including Huaiwei Ni, Hejiu Hui, Yang Chen, Matt Mannon, Steven Ownby, Zeb Page, Lixing Jin, Lin Ma, Xiqiao Xu, Ni Sun, Maodu Yan, Qiong Liu, Yuehan Lu and Tie Sun, are all appreciated for their friendship. They made my life in Ann Arbor more enjoyable and happier. Special thanks go to Hejiu Hui, Huaiwei Ni and Ya Gao, who generously offered their help when I needed them most.

My deepest and warmest thanks go to my wife, Ying Zhao, and our families for their love and support over these years.

TABLE OF CONTENTS

LIST OF FIGURES

Figure

LIST OF TABLES

Table

LIST OF APPENDICES

Appendix

CHAPTER I

INTRODUCTION

Studying the thermodynamic properties of minerals and their phase equilibria under mantle conditions is important to mantle petrology and metamorphic petrology. Not only can the composition and structure of the Earth's mantle be better constrained, but also the tectonic history of ultra-high pressure (UHP) metamorphic rocks, including the pressure-temperature-time (P-T-t) path, can be better constrained. Generally speaking, there are two independent ways to study the phase equilibria of silicates under mantle conditions: either by doing high pressure and high temperature phase equilibrium experiments, or through thermodynamic calculation. Although doing phase equilibrium experiments is the most common way, thermodynamic calculation is used in this dissertation because it has two major advantages over the experiments. Compared with phase equilibrium experiments which are usually done at high temperatures, the thermodynamic calculation can cover the whole temperature range. Secondly, the slope of the phase transition boundary can be determined more precisely by thermodynamic calculation, especially for sluggish reactions involving silicates.

Unfortunately, pure thermodynamic studies of phase transitions under mantle

conditions are extremely difficult to undertake because of the lack of low-temperature heat capacity data of many mantle phases. Heat capacity is a fundamental, material-specific thermodynamic property, which provides the most precise way to obtain the entropy value, another critical property requisite for thermodynamic modeling of the phase relations in the Earth's interior. On the other hand, these high pressure phases must be synthesized experimentally, and the minimum amount of sample needed for low-temperature heat capacity measurement by conventional low-temperature adiabatic calorimetry (low-TAC), which is 10-30 grams in general, would take hundreds of experimental runs just to make enough samples, hence prohibiting the heat capacity measurement in practice. However, the recently developed heat capacity option of the Physical Properties Measurement System (PPMS, produced by Quantum Design®), based on heat-pulse calorimetry (HPC), which can give precise low-temperature heat capacity measurements of milligram-sized samples, provides an excellent solution to the dilemma. In this dissertation, PPMS is used to measure the low-temperature heat capacity data of some selected mantle phases, and the phase equilibria related to them are studied thermodynamically.

The low-temperature heat capacity data of K-hollandite ($KAlSi_3O_8$), a phase isostructural to hollandite ($BaMn_8O_{16}$) and Si-wadeite ($K_2Si_4O_9$), a phase isostructural to wadeite ($K_2ZrSi_3O_9$) are reported in Chapter II and Chapter III, respectively. These two phases were selected because both of them are related to sanidine, one of the most abundant minerals of the continental crust. Sanidine or its polymorphs can be transported

into UHP condition along with the subducted slab, where it will transform to Si-wadeite and K-hollandite. The Si-wadeite forms in the coesite stability field and K-hollandite in the stishovite stability field, so they may serve as index minerals further delineating the pressures of UHP metamorphic rocks. In addition, ^{40}K is an important heat source in the evolutionary history of the Earth, and previous experimental studies showed that Si-wadeite and K-hollandite are stable phases at conditions corresponding to the Earth's upper mantle and transition zone (Ringwood et al. 1967; Kinomura et al. 1975; Yagi et al. 1994; Urakawa et al. 1994). Therefore these two phases may be the potential reservoir of potassium in the upper mantle and transition zone. However, the phase equilibria related to K-hollandite and Si-wadeite are still not well constrained in terms of the slope of the reactions. The purpose of this research is to accurately study the phase boundaries in the system $K_2O-Al_2O_3-SiO_2-H_2O$ by thermodynamic calculation with the help of newly measured heat capacity data of K-hollandite and Si-wadeite. The results of Chapter II have been published in *Physics and Chemistry of Minerals* (Yong et al. 2006). Chapter III has been published in *Contributions to Mineralogy and Petrology* (Yong et al. 2008).

Chapter IV is a calorimetric study of γ-Fe_2SiO_4, the high pressure polymorph of fayalite, which is one end-member of olivine, the most abundant mineral in the Earth's upper mantle. The motivation of this study lies in the fact that the phase transitions in the $(Mg,Fe)_2SiO_4$ system are generally considered to play an important role in the formation of seismic discontinuities in the Earth's mantle. Therefore studying the thermodynamic properties of γ-Fe_2SiO_4 would help better understand the phase transitions in the

$(Mg,Fe)_2SiO_4$ system, hence better constraining the composition and structure of the Earth's mantle. Pure γ-Fe_2SiO_4 was synthesized using a multi-anvil device at 8.5 GPa and 1,273K. The heat capacity option of PPMS was used to measure the low-temperature heat capacity of γ-Fe_2SiO_4 from 5 to 303 K and a broad λ-transition at 11.8 K, presumably due to paramagnetic−antiferromagnetic transition is documented. This chapter has been published in *Physics and Chemistry of Minerals* (Yong et al. 2007).

The possible geological applications of the data for K-hollandite, Si-wadeite and γ-Fe_2SiO_4 are briefly discussed in Chapter V. The drawbacks in thermodynamic studies of minerals under deep mantle conditions are also summarized in this chapter. Two projects that are outside the scope of this dissertation have been attached as appendices.

REFERENCES

Kinomura N, Kume N, Koizumi M (1975) Stability of $K_2Si_4O_9$ with wadeite type structure. Proc 4th Inter Conf High Pressure Sci Tech, pp 211–214

Ringwood AE, Reid AF, Wadsley AD (1967) High–pressure $KAlSi_3O_8$, an alumino-silicate with sixfold coordination. Acta Cryst 23:1093–1095

Urakawa S, Kondo T, Igawa N, Shimomura O, Ohno H (1994) Synchrotron radiation study on the high-pressure and high-temperature phase relations of $KAlSi_3O_8$. Phys Chem Minerals 21:387–391

Yagi A, Suzuki T, Akaogi M (1994) High pressure transitions in the system $KAlSi_3O_8$ – $NaAlSi_3O_8$. Phys Chem Minerals 21:12–17

Yong W, Dachs E, Withers AC, Essene EJ (2006) Heat capacity and phase equilibria of hollandite polymorph of $KAlSi_3O_8$. Phys Chem Minerals 33:167–177

Yong W, Dachs E, Withers AC, Essene EJ (2007) Low-temperature heat capacity and thermodynamic properties of γ-Fe_2SiO_4. Phys Chem Minerals 34:121–127

Yong W, Dachs E, Withers AC, Essene EJ (2008) Heat capacity and phase equilibria of wadeite-type $K_2Si_4O_9$. Contr Mineral Petrol 155: 137–146

CHAPTER II

HEAT CAPACITY AND PHASE EQUILIBRIA OF HOLLANDITE POLYMORPH OF $KAlSi_3O_8$

ABSTRACT

The low-temperature heat capacity (C_p) of $KAlSi_3O_8$ with a hollandite structure was measured over the range of 5–303 K with a physical properties measurement system (PPMS). The standard entropy of $KAlSi_3O_8$ hollandite is 166.2 ± 0.2 $Jmol^{-1}K^{-1}$, including an 18.7 $Jmol^{-1}K^{-1}$ contribution from the configurational entropy due to disorder of Al and Si in the octahedral sites. The entropy of $K_2Si_4O_9$ with a wadeite structure (Si-wadeite) was also estimated to facilitate calculation of phase equilibria in the system K_2O–Al_2O_3–SiO_2. The calculated phase equilibria obtained using Perple_x are in general agreement with experimental studies. Calculated phase relations in the system K_2O-Al_2O_3-SiO_2 confirm a substantial stability field for kyanite-stishovite/coesite-Si-wadeite intervening between $KAlSi_3O_8$ hollandite and sanidine. The upper stability of kyanite is bounded by the reaction kyanite (Al_2SiO_5) = corundum (Al_2O_3) + stishovite (SiO_2), which is located at 13-14 GPa for 1100-1400 K. The entropy and enthalpy of formation for K-cymrite ($KAlSi_3O_8 \cdot H_2O$) were modified to better fit global best-fit compilations of thermodynamic data and experimental studies. Thermodynamic calculations were

undertaken on the reaction of K-cymrite to $KAlSi_3O_8$ hollandite + H_2O, which is located at 8.3–10.0 GPa for the temperature range 800-1600 K, well inside the stability field of stishovite. The reaction of muscovite to $KAlSi_3O_8$ hollandite + corundum + H_2O is placed at 10.0–10.6 GPa for the temperature range 900–1500 K, in reasonable agreement with some but not all experiments on this reaction.

INTRODUCTION

Ringwood et al. (1967) first discovered that potassium feldspar transforms into a hollandite structure when pressure exceeds 12 GPa. The K atoms in $KAlSi_3O_8$ hollandite are accommodated in tunnels formed by double chains of edge-sharing $(Si,Al)O_6$ octahedra (Ringwood et al. 1967; Yamada et al. 1984; Zhang et al. 1993). Kinomura et al. (1975) found an intermediate-pressure assemblage of kyanite (Al_2SiO_5), coesite (SiO_2), and $K_2Si_4O_9$ with a wadeite structure (Si-wadeite) separating the stability field of sanidine at low pressure and $KAlSi_3O_8$ hollandite at high pressure. This was verified by additional experiments (Urakawa et al. 1994; Yagi et al. 1994). The lower stability of $KAlSi_3O_8$ hollandite was located at pressures of 8-10 GPa for temperatures of 1000-1500 K. With one-fourth of the Si atoms in octahedral sites, the structure of Si-wadeite ($K_2Si_4O_9$) can be considered as three-membered rings of SiO_4 tetrahedra connected by octahedrally coordinated Si atoms (Kinomura et al. 1977; Swanson and Prewitt 1983). Liu (1978) reported $KAlSi_3O_8$ hollandite plus a high-pressure form of $KAlO_2$ forming from kalsilite ($KAlSiO_4$) in the pressure range of 17-30 GPa. Faust and Knittle (1994)

documented the breakdown of a natural muscovite to $KAlSi_3O_8$ hollandite + corundum + H_2O at pressures between 10.9 and 12.0 GPa at around 1073 K. The phase $KAlSi_3O_8$ hollandite has also been reported in hydrated average upper continental crust, MORB, andesite and pelite compositions when pressure is greater than 8 GPa (Irifune et al. 1994; Schmidt 1996; Domanik and Holloway 1996, 2000; Ono 1998; Wang and Takahashi 1999). Electron microprobe analyses of run product hollandite by Domanik and Holloway (2000) show 14-30% deficiencies in the K site that are not matched by excess Si. They inferred that phengite decomposed to $KAlSi_3O_8$ hollandite between 9 and 10 GPa at 900°C. Domanik and Holloway (2000) noted that their hollandite was damaged by the electron beam but did not correct for elemental migration. Their low K site occupancies probably represent an analytical artifact rather than a vacancy substitution. Examination of their assemblages suggests progress of the reaction muscovite + coesite/stishovite = $KAlSi_3O_8$ hollandite + kyanite + fluid, as well as more complex reactions that involve magnesite, garnet and OH-topaz. Konzett and Fei (2000) reported $KAlSi_3O_8$ hollandite as one of the breakdown products at 20-23 GPa and 1773-1973 K in peralkaline and subalkaline rock compositions. Quench experiments by Tutti et al. (2001) showed that $KAlSi_3O_8$ hollandite is still stable at pressure as high as 95 GPa, consistent with previous suggestions that $KAlSi_3O_8$ hollandite is an important host for potassium in the lower mantle (Ringwood 1975; Prewitt and Downs 1998). Occurrences of natural $KAlSi_3O_8$ hollandite and $NaAlSi_3O_8$ hollandite ($NaAlSi_3O_8$ with hollandite structure) have been reported in shocked meteorites (Akaogi 2000; Gillet et al. 2000; Langenhorst

and Poirier 2000; Tomioka et al. 2000; Kimura et al. 2004). Sueda et al. (2004) demonstrated that $KAlSi_3O_8$ hollandite transforms to a new high-pressure phase ($KAlSi_3O_8$ hollandite II) at ~22 GPa at room temperature using in situ X-ray diffraction. They related this transition to the abrupt enrichments of Ca and Na components in $KAlSi_3O_8$ hollandite coexisting with a potassic basalt melt at ~22.5 GPa observed by Wang and Takahashi (1999). In situ X-ray diffraction study by Nishiyama et al. (2005) confirmed that this transition happens at pressures of 20-23 GPa and temperatures of 300-1000 K. Collectively, the experimental studies suggest that $KAlSi_3O_8$ hollandite has an important role in transporting potassium during subduction of oceanic crust into the deep mantle.

The thermodynamic properties of several phases are in need of further study in order to accurately determine the phase equilibria in the system K_2O–Al_2O_3–SiO_2, although some measurements have been made. The enthalpy of Si-wadeite and $KAlSi_3O_8$ hollandite was determined by Geisinger et al. (1987) and Akaogi et al. (2004) using high-temperature solution calorimetry. The high-temperature heat capacity of Si-wadeite was measured by Fasshauer et al. (1998). They generated an internally consistent thermodynamic data set for several phases but did not include $KAlSi_3O_8$ hollandite in their evaluation. Akaogi et al. (2004) measured the high-temperature heat capacity data of $KAlSi_3O_8$ hollandite and reevaluated the phase relations in the system K_2O-Al_2O_3-SiO_2 by combining thermodynamic with experimental data. However, an approach totally independent of the experiments has not been applied to this system because the

lack of low-temperature heat capacity data, and hence lack of entropy and Gibbs free energy, of the high-pressure phases. In this study, the low-temperature heat capacity of $KAlSi_3O_8$ hollandite was measured using a physical properties measurement system (PPMS, produced by Quantum Design®), and the entropy of $KAlSi_3O_8$ hollandite was calculated from the measured heat capacity data. The entropy of Si-wadeite was estimated from Holland (1989), and phase relations in the system K_2O–Al_2O_3–SiO_2 were calculated based on the new thermodynamic data. Several reactions involving $KAlSi_3O_8$ hollandite were also investigated in the system K_2O–Al_2O_3–SiO_2–H_2O.

EXPERIMENTAL PROCEDURES

Sample Synthesis and Characterization

The $KAlSi_3O_8$ hollandite was synthesized using a 1000-ton Walker-type multi-anvil device at the University of Minnesota. Tungsten carbide anvils with 8 mm truncations, cast MgO–Cr_2O_3 octahedra with 14 mm edge lengths and pyrophyllite gaskets were used for this study. $KAlSi_3O_8$ glass from Craig Manning at UCLA was used as the starting material. It was powdered and loaded into a cylindrical Re capsule, which also acts as the furnace. After being held at 14 GPa and 1673 K for 24 hours, the starting material was quenched at 14 GPa and slowly recovered to ambient pressure. Temperature was controlled by a $W_3Re_{97}/W_{25}Re_{75}$ thermocouple oriented vertically with respect to the heater.

The run product was confirmed to be $KAlSi_3O_8$ hollandite by X-ray diffraction

and electron microprobe (EMP) analysis. The tetragonal lattice parameters of the synthesized $KAlSi_3O_8$ hollandite were determined using the Scintag Crystallography program as a = 9.313(3) Å and c = 2.723(3) Å, which are in good agreement with the values, a = 9.315(4) Å and c = 2.723(4) Å, by Zhang et al. (1993) and deviate only slightly from the data, a = 9.3244(4) Å and c = 2.7227(3) Å of Yamada et al. (1984). The EMP analyses were performed using Cameca SX-100, and the avarage values for 25 runs of $KAlSi_3O_8$ hollandite are shown in Table 2.1. The column conditions were: accelerating voltage 15 kV, beam current 4 nA, peak and background counting times each 10 s, and beam scan area 5×5 μm. The low current was used because preliminary analyses showed the sensitivity of hollandite to an electron beam. The standards used for Na, Mg, Fe, Al, Si and K are Tiburon albite, synthetic $MgTiO_3$, synthetic $FeSiO_3$, K-feldspar from St. Gotthard, respectively. The small amounts of Na, Mg and Fe are around the detection limits, and their effects on the heat capacity measurement are negligible. Compared to previous EMP studies on synthetic $KAlSi_3O_8$ hollandite that indicated an apparent deficiency on the K site (Irifune et al. 1994; Schmidt 1996; Domanik and Holloway 1996, 2000; Ono 1998; Wang and Takahashi 1999), the EMP analyses in this study shows no evidence for a vacancy on that site. Less accurate TEM analyses of natural $KAlSi_3O_8$ hollandite from shock metamorphosed meteorites also showed an apparent vacancy on the K site (Langenhorst and Poirier 2000). It will be assumed that the $KAlSi_3O_8$ hollandite in this study is pure and stoichiometric.

Heat Capacity Measurement

The low-temperature heat capacity at constant pressure (C_p) of $KAlSi_3O_8$ hollandite was measured at 1 atm using the heat capacity option of the PPMS at Salzburg University in Austria. Based on heat-pulse calorimetry (HPC), the PPMS is the first commercially available apparatus that can measure the low-temperature heat capacity of samples with milligram mass. Lashley et al. (2003) and Dachs and Bertoldi (2005) provided a detailed description of the PPMS, its use in heat capacity measurements, and an evaluation of measurement errors. The technique is summarized below.

The central part of the PPMS calorimeter is the calorimeter puck, made up of the puck frame and the sample platform that holds the sample. The sample holder is a 4×4 mm wide sapphire platform that has a thermometer and a heater attached to the lower side. Thin Pt wires attached to the sample platform provide the electrical connection and structural support between the platform and the puck frame. The puck is covered with a cap and resides at the base of a sample chamber, the inner part of the PPMS probe that is directly immersed in a liquid helium bath.

In heat-pulse calorimetry (HPC) as employed in the PPMS calorimeter, a known amount of heat is applied to a sample at selected temperatures, and the resultant temperature change is recorded. Two separate measurements, known as "addenda run" and "sample run", are carried out for the quantitative determination of heat capacity. In an addenda run, the heat capacity of the empty sample platform plus some grease applied

to it is determined based on Fourier's law of heat conduction and the law of conservation of energy, as the following equation:

$$P(t) = C_{\mathrm{p}}{}^{pl}\frac{dT_{pl}(t)}{dt} + K_w\left(T_{pl}(t) - T_b\right) \qquad (1)$$

where "pl" stands for platform, $dT_{pl}(t)/dt$ is the thermal response of the platform to which a square pulse of heat $P(t)$ is applied, K_w is the thermal conductance of the wires (in units $W{\cdot}K^{-1}$) and T_b is the temperature of the puck frame. A non-linear least-squares fit to the analytical solutions of equation (1) (Dachs and Bertoldi 2005: their equations 6a, 6b) yields the heat capacity of the empty sample platform, $C_{\mathrm{p}}{}^{pl}$, at the temperature T_{pl}. This procedure is then repeated at the desired temperature with the sample mounted on the sample platform during the sample run. The equations that describe the heat balance conditions in this case are:

$$\begin{cases} P(t) = C_p{}^{pl}\dfrac{dT_{pl}(t)}{dt} + K_w\left(T_{pl}(t) - T_b\right) + K_g\left(T_{pl}(t) - T_s(t)\right) \\ 0 = C_p{}^{s}\dfrac{dT_s(t)}{dt} + K_g\left(T_s(t) - T_{pl}(t)\right) \end{cases} \qquad (2)$$

where K_g is the thermal conductance due to the grease between the sample and the sample platform, T_s and $C_{\mathrm{p}}{}^{s}$ are the temperature and the heat capacity of the sample, respectively. Because T_{pl} can be directly mearured by PPMS, elimination of T_s in equation (2) will generate:

$$\frac{d^2T_{pl}}{dt^2} + \frac{dT_{pl}}{dt}\left[\frac{(C_p{}^s K_w / K_g + C_p{}^s + C_p{}^{pl})K_g}{C_p{}^s C_p{}^{pl}}\right] + \frac{K_w K_g}{C_p{}^s C_p{}^{pl}} T_{pl} = \frac{K_g}{C_p{}^s C_p{}^{pl}}\left[\frac{C_p{}^s}{K_g}\frac{dP(t)}{dt} + P(t) + K_w T_b\right] \quad (3)$$

As C_p^{pl} is already known from the addenda run, the remaining four unknowns: K_g, K_w, T_b and C_p^s, are calculated by applying the same non-linear least square fitting routine to the analytical solution of equation (3) (Dachs and Bertoldi 2005: their equations 10a, 10b) based on the temperature-time response curve measured during the sample run (40-200 data pairs for each measurement at a specific temperature). The standard deviation, σ_{Cp}, of each measurement can also be obtained from this fitting procedure. The heat capacity contribution of the container is subtracted from the total heat capacity to give the net heat capacity of the unknown samples. Dachs and Bertoldi (2005) showed that heat capacity measurements on sealed powders by PPMS were systematically lower than low-temperature adiabatic calorimetry (LTAC) data by 1-2 % in the temperature range between 100 K and 300 K. At 5-20 K, where the absolute values of heat capacity are small, the measured data by PPMS may be up to 50% larger than those measured by LTAC. The entropies at 298.15 K derived from PPMS heat capacity measurements are at maximum 1-2 % lower than those calculated from LTAC experiments (Dachs and Bertoldi 2005).

RESULTS

Heat Capacity and Entropy of $KAlSi_3O_8$ Hollandite

The measured molar heat capacity (C_p) of $KAlSi_3O_8$ hollandite versus temperature is listed in Table 2.2 and shown in Figure 2.1. To obtain the entropy of $KAlSi_3O_8$ hollandite, a general polynomial with $C_p = k_0 + k_1T^{-0.5} + k_2T^{-2} + k_3T^{-3} + k_4T + k_5T^2 + k_6T^3$ was chosen to fit the C_p data in Table 2.2 using the Experimental Data Analyst Package of Mathematica®. The data were split into three temperature regions and each region was fitted individually with some overlap of data. The equation $C_p = k_0 + k_1T^{-0.5} + k_2T^{-2} + k_3T^{-3}$ was used for fitting the high temperature portion of the data, the complete polynomial given above for the intermediate temperature portion and $C_p = k_4T + k_6T^3$ is for fitting at low temperature. The C_p data below 5 K were estimated by a linear extrapolation to 0 K from the lowest measured C_p point in the form of $C_p = k_6T^3$. The resulting C_p coefficients and temperatures at interval boundaries are given in Table 2.3, where the final entropy value varies only insignificantly (only in the second digit) upon choosing a different splitting temperature of the C_p data (Table 2.3, Fit 1 compared to Fit 2). The uncertainty in the entropy at standard temperature and pressure was estimated by a Monte Carlo technique. A detailed description of error estimation is provided in Dachs and Bertoldi (2005). The entropy of $KAlSi_3O_8$ hollandite at 298.15 K calculated by integration of these fitted functions is 147.5 ± 0.2 $Jmol^{-1}K^{-1}$ (error is one standard deviation). The crystal structure refinement of $KAlSi_3O_8$ hollandite shows that Al and Si atoms are fully disordered over the octahedral sites (Yamada et al. 1984; Zhang et al. 1993), thus requiring addition of the configurational entropy, S_0° to the entropy term. The

configurational entropy is calculated as S_0° = −4R(0.25ln0.25+0.75ln0.75) = 18.7 $Jmol^{-1}K^{-1}$. Including this contribution, the entropy obtained for $KAlSi_3O_8$ hollandite at standard temperature and pressure (STP) is 166.2 ± 0.2 $Jmol^{-1}K^{-1}$. That value is in striking disagreement with the value of 65.3 $Jmol^{-1}K^{-1}$ that was estimated by Domanik and Holloway (2000). Their estimate was derived by summation techniques based on a complex dehydration reaction involving phengite in the system KMASH and is likely to have large errors that were not evaluated. The high-temperature C_p data of $KAlSi_3O_8$ hollandite were measured by Akaogi et al. (2004) using differential scanning calorimetry. Their data were used for calculation of the enthalpy and entropy above ambient temperature (Table 3.4). The smooth fit of our C_p data with that of Akaogi et al. (2004) provides strong support for the STP entropy obtained in this study but not for the estimate of Domanik and Holloway (2000).

Entropy of Si-wadeite and Phase Equilibria in K_2O−Al_2O_3−SiO_2 System

High-pressure experimental studies on the phase transitions in $KAlSi_3O_8$ were carried out by Yagi et al. (1994) and Urakawa et al. (1994) on the following reactions:

2 sanidine = Si-wadeite + kyanite + coesite (4)

Si-wadeite + kyanite + coesite = 2 $KAlSi_3O_8$ hollandite (5)

Si-wadeite + kyanite + stishovite = 2 $KAlSi_3O_8$ hollandite (6)

The experimental results are shown in Fig. 2.2. The experiments by Yagi et al.

(1994) were revised by Akaogi et al. (2004) because the original pressure calibration was mainly on the coesite-stishovite transition by Yagi and Akimoto (1976), which is 0.3-0.4 GPa higher than the most recent work by Zhang et al. (1996). The results after recalibration are comparable to the in situ X-ray experiments of Urakawa et al. (1994), which were based on a NaCl pressure scale.

Thermodynamic calculations were undertaken with the computer program Perple_x (Connolly and Kerrick 1987; Connolly 1990) using a modified Holland and Powell (1998) data base, and including the new data from this research for $KAlSi_3O_8$ hollandite and Si-wadeite. Table 2.4 shows the sources of phase properties involved in this study. For the solid phases, the temperature dependence of the molar volume, $V^o(T)$, is given by

$$V^\circ(T) = V^\circ_{298}\left(1 + \int_{298}^{T} \alpha dT\right) \qquad (7)$$

where α and V°_{298} are the thermal expansion and molar volume at standard state, respectively. The pressure dependence of the molar volume was calculated using the Murnaghan equation of state:

$$V(T,P) = V^\circ(T)\left(1 + \frac{K'}{K_T}P\right)^{-\frac{1}{K'}} \qquad (8)$$

where K_T and K' are the isothermal bulk modulus and its pressure derivative, respectively. The compensated-Redlich-Kwong (CORK) equation from Holland and Powell (1991, 1998) was chosen for the PVT-behaviour of H_2O.

Unfortunately, the entropy of Si-wadeite has not been determined calorimetrically. Fasshauer et al. (1998) estimated a value of 232±10 $Jmol^{-1}K^{-1}$ for S°_{298} of Si-wadeite, about 33 $Jmol^{-1}K^{-1}$ larger than that calculated by Geisinger et al. (1987) from spectroscopic data. This is partly supported by the systematically higher C_p observed by differential scanning calorimetry (DSC) at T < 500 K than that derived from vibrational spectroscopy (Fasshauer et al., 1998). Thermodynamic calculations using Perple_x also favor a larger value for S°_{298} of Si-wadeite. The calculated phase relations using $S^{\circ}_{298\,(wad)}$ = 232 ± 10 $Jmol^{-1}K^{-1}$ are shown in Fig. 2.2 (dashed lines). Unfortunately, large discrepancies remain between the calculated phase boundaries and the experimental data of Yagi et al. (1994) and Urakawa et al. (1994). An even larger value for S°_{298} of Si-wadeite is necessitated to fit the experimental data with thermodynamic calculation.

The S°_{298} of Si-wadeite was therefore estimated from Holland (1989) as follows:

$$\begin{aligned} S^{\circ}_{298(wad)} &= (3S^{[4]}_{SiO_2} + S^{[6]}_{SiO_2} + S_{K_2O(a)}) + k[V^{\circ}_{298(wad)} - (3V^{[4]}_{SiO_2} + V^{[6]}_{SiO_2} + V_{K_2O(a)})] \\ &= kV^{\circ}_{298(wad)} + 3(S - kV)^{[4]}_{SiO_2} + (S - kV)^{[6]}_{SiO_2} + (S - kV)_{K_2O(a)} \\ &= 108.44 + 3 \times 17.45 + 10.49 + 79.55 \cong 251 \pm 4 \text{ J mol}^{-1} \text{ K}^{-1} \end{aligned}$$

where k = 1.0 $JK^{-1}cm^{-3}$, which corresponds to solid-solid reactions involving no change in coordination state that have dP/dT = 10 $barK^{-1}$. The values of $(S - kV)^{[4]}_{SiO_2}$ and $(S - kV)_{K_2O(a)}$ can be found in Holland (1989), which are calculated from the regression of a set of 60 experimentally measured entropies and volumes of silicates and oxides. $(S - kV)^{[4]}_{SiO_2}$ and $(S - kV)_{K_2O(a)}$ correspond the tetrahedral coordination for SiO_2 and framework sites such as in feldspars for K_2O, respectively. However, the value of

$(S - kV)^{[6]}_{SiO_2}$, which represents the octahedral coordination for SiO_2, is not included in that study. Here this value was calculated using stishovite data from Holland and Powell (1998) data base. The phase boundary of reaction (4) calculated with the revised entropy of Si-wadeite fits the experimental data of Yagi et al. (1994) and Urakawa et al. (1994) reasonably well (the lower solid line in Fig. 2.2). A small modification from $\Delta H^{\circ}_{f,298}$ = −3801 ± 8 kJmol^{-1} to $\Delta H^{\circ}_{f,298}$ = −3803.5 kJmol^{-1} that is within the error of $\Delta H^{\circ}_{f,298}$ of $KAlSi_3O_8$ hollandite was applied to bring the calculated phase boundaries of reaction (5) and (6) into better agreement with the experimental data of Yagi et al. (1994) and Urakawa et al. (1994) (the upper solid line in Fig. 2.2). The calculated boundary for the decomposition of sanidine into kyanite, coesite, and Si-wadeite in Fig. 2.2 is almost identical to that determined by Akaogi et al. (2004), and reasonable consistency is obtained with the experimental results of Yagi et al. (1994) and Urakawa et al. (1994) above 1100 K. The difference between the experimental data and the calculated phase boundary below 1100 K can be explained either by sluggish reaction rates or by remaining uncertainties in the thermodynamic properties (Akaogi et al. 2004). The phase boundary of Si-wadeite + kyanite + SiO_2 –polymorph (stishovite or coesite) = $2KAlSi_3O_8$ hollandite intersects the coesite-stishovite transition boundary at about 1575 K and 9.5 GPa (Fig. 2.2), which generates reaction (5) at temperatures > 1575 K and reaction (6) at temperatures < 1575 K, respectively. The calculated locus of reactions (5) and (6) is 0.3 – 0.4 GPa higher than that of Akaogi et al. (2004). Choosing 8.7 GPa at 1273 K for the phase boundary from Akaogi et al. (2004) might be a source of the

difference. Nonetheless, the result of this study and that of Akaogi et al. (2004) are consistent with the experimental study of Yagi et al. (1994) and Urakawa et al. (1994) within expected errors of a few kilobars.

Using the estimated values of entropy and the refined enthalpy data of Si-wadeite and $KAlSi_3O_8$ hollandite as well as the modified Holland and Powell (1998) data base, a P-T diagram for the system K_2O-Al_2O_3-SiO_2 was calculated with Perple_x (Fig. 2.3). Fasshauer et al. (1998) suggested that sanidine would disproportionate first to kalsilite ($KAlSiO_4$) + coesite at around 5 GPa when temperature is above 823 K, and this assemblage would remain stable until pressure reaches 6-7 GPa. However, the calculated P-T phase diagram in this study doesn't show a region where reaction (4) is metastable. The reaction kalsilite + sanidine = kyanite + Si-wadeite has been identified both by Fasshauer et al. (1998) and in this study, although the location of the boundary varies somewhat between the two works. For reactions with Si-wadeite, discrepancies between this study and Fasshauer et al. (1998) are mainly caused by different values of S°_{298} for Si-wadeite. A calorimetric determination of S°_{298} of Si-wadeite will be necessary to resolve remaining discrepancies in this system. Additional reactions involving corundum (Al_2O_3), which Fasshauer et al. (1998) didn't include in their study, have also been identified and located provisionally. The reaction kyanite = corundum + stishovite is located at about 13-14 GPa at 1100-1400 K and represents the upper stability of kyanite. The calculated phase boundary is 0.1-0.2 GPa lower than the experimental results of Schmidt et al. (1997) (Fig. 2.3, triangles) at temperatures above 1500 K. The disagreement is certainly

within expected experimental errors, especially those related to pressure calibration of multi-anvil apparatus. Errors in the calculation may derive from difficulties in extrapolating the C_p data of stishovite to such high temperatures.

Phase Equilibria in K_2O-Al_2O_3-SiO_2-H_2O

At high pressures and in the presence of water, K-feldspar reacts to form a hydrated phase $KAlSi_3O_8 \cdot H_2O$, called "K-cymrite" (Massonne 1992) or "sanidine hydrate" (Thompson et al. 1998). A detailed crystal structure study of $KAlSi_3O_8 \cdot H_2O$ by Fasshauer et al. (1997) suggests that it is indeed isostructural with $BaAl_2Si_2O_8 \cdot H_2O$ cymrite, although the Al and Si atoms are highly disordered in $KAlSi_3O_8 \cdot H_2O$ whereas in cymrite the Al and Si atoms are ordered. In this study the informal name K-cymrite will be used for the synthetic phase $KAlSi_3O_8 \cdot H_2O$. Seki and Kennedy (1964) placed the phase boundary of the following reaction at around 1.8–2.8 GPa and 700–1000 K for K-cymrite based on synthesis experiments of the following reaction:

$$\text{sanidine} + H_2O = \text{K-cymrite} \qquad (9)$$

However, experiments by Massonne (1992) on this reaction yielded a much flatter slope at around 2.5 GPa, and this result was confirmed by reversed experiments of Fasshauer et al. (1997), Thompson (1994) and Thompson et al. (1998). Fasshauer et al. (1997) applied a Bayesian method to evaluate the thermodynamic properties of the phases in reaction (9) and derived the standard enthalpy of formation and entropy for K-cymrite. They treated the order-disorder relations of microcline to sanidine with a Landau

formalism following Carpenter and Salje (1994). We recalculated the entropy and enthalpy of formation for K-cymrite to best fit the experimental reversals by Fasshauer et al. (1997) and Thompson et al. (1998). The revised thermodynamic data are shown in Table 2.4 and the best fit phase boundary is shown in Figure 2.4. The revised enthalpy of formation and entropy for K-cymrite are ~5 $kJmol^{-1}$ more negative and ~8 $Jmol^{-1}K^{-1}$ more positive than the respective values of Fasshauer et al. (1997). They added a footnote that their enthalpy of K-cymrite should be changed by –7 $kJmol^{-1}$ to bring the enthalpy of microcline into accord with the data of Robie and

Hemingway (1995). The enthalpy calculated in this study is in disagreement with the revised value of Fasshauer et al. (1997) by +2 $kJmol^{-1}$, a relatively small error for such a calculation. The cause of the large discrepancy in the estimated entropy of K-cymrite is unclear, because the compressibility and thermal expansion data of Fasshauer et al. (1997) for K-cymrite were used in the present calculations. The phase boundary for reaction (9) calculated with the revised values of this study is in agreement with experimental reversals of Fasshauer et al. (1997) and Thompson et al. (1998). It is located at < 3 GPa at T < 1100 K (Fig. 2.4).

The pressure needed for the formation of K-cymrite is less than the peak pressure of many ultrahigh-pressure metamorphic (UHPM) rocks (e.g. Schertl et al. 1991; Sharp et al. 1993; Kaneko et al. 2000; Chopin 2003; Yoshida et al. 2004). In nature the a_{H_2O} may be reduced from unity in the presence of other components such as CO_2 or NaCl, in the

absence of a fluid phase, or in the presence of a melt (e.g., Edwards and Essene 1988; Valley et al. 1990). Reaction (9) is successively shifted to higher pressures as a_{H_2O} is reduced (Fig. 2.4), but even at an a_{H_2O} of 0.5 K-cymrite is still stable at UHPM conditions. It is expected that sanidine will hydrate to form K-cymrite during UHPM processes, although K-cymrite has not yet been reported in nature. Hwang et al. (2004) discovered a new polymorph of K-feldspar, kokchetavite, in the UHPM Kokchetav terrane of Kazahkstan. Reminiscent of the experiment by Thompson et al. (1998), who reported a hexagonal $KAlSi_3O_8$ phase (probably isostructural to kokchetavite) when K-cymrite is dehydrated at T > 1273 K and ambient pressure, Hwang et al. (2004) suggested that kokchetavite could represent the dehydration product of K-cymrite during exhumation. Massonne and Nasdala (2003) also described inclusions in garnets made up of quartz, K-feldspar and micaceous material that possibly formed as pseudomorphs after K-cymrite in a diamondiferous quartzofeldspathetic rock from the Erzgebirge, Germany. K-cymrite probably dehydrates rapidly to sanidine during exhumation of K-rich UHPM rocks, especially in those that attained relatively high metamorphic temperatures (973-1173 K).

Harlow and Davies (2004) inferred a negative P/T slope for the breakdown of K-cymrite based on two experimental runs: 9 GPa at 1473 K and 8 GPa at 1523 K for the reaction

$$\text{K-cymrite} = KAlSi_3O_8 \text{ hollandite} + H_2O \qquad (10)$$

However, the calculated phase transition boundary shows a slight positive P/T slope, which lies 0.4-1.4 GPa higher than the two experimental runs by Harlow and Davies (2004) (Fig. 2.5). A calorimetric study of K-cymrite and reversed experiments are indicated to address this discrepancy and better constrain the phase transition boundary of reaction (10).

Faust and Knittle (1994) documented the breakdown of a natural muscovite, $KAl_3Si_3O_{10}(OH)_2$, to $KAlSi_3O_8$ hollandite at pressures between 10.9 and 12 GPa around 1073 K via the following reaction:

muscovite = $KAlSi_3O_8$ hollandite + corundum + H_2O (11)

The PT location of reaction (11) was calculated with Perple_x and the thermodynamic data in Table 4 (Fig. 2.6). This reaction is located at about 10.1 GPa at 1073 K and 10.5 GPa at 1600 K, ~1-2 GPa lower than the experimental results by Faust and Knittle (1994). Considering the large pressure uncertainties in the laser-heated diamond cell experiments by Faust and Knittle (1994), the calculated phase boundary is considered to be in reasonable agreement with their experiments. The calculated reaction curve has a significantly different slope than that of Sekine et al. (1991) (dashed line in Fig. 2.6). The discrepancy may result from their placement of the then less well constrained reactions (4) and (6), that were used to extrapolate the thermodynamic data of $KAlSi_3O_8$ hollandite. Experimental data on the breakdown reaction of phengite (a K-rich mica) to $KAlSi_3O_8$ hollandite by Schmidt (1996) are in good agreement with our

calculations in this study and are plotted in Fig. 2.6 for comparison (dotted line).

Sekine et al. (1991) and Faust and Knittle (1994) reported two other decomposition reactions of muscovite:

muscovite = K-cymrite + corundum (12)

2 muscovite = Si-wadeite + 2 kyanite + corundum + 2 H_2O (13)

These two reactions are thought to occur at low pressures. However, the present thermodynamic calculations show that reaction (12) only proceeds above 1700 K, and reaction (13) is metastable, as it is located at pressures > ~11 GPa, where muscovite has already dehydrated to $KAlSi_3O_8$ hollandite + corundum + H_2O.

DISCUSSION

The calculated PT locations of reactions (5) and (6) constrain the lower stability limit of $KAlSi_3O_8$ hollandite at 9-10 GPa for T > 1000 K. The occurrence of $KAlSi_3O_8$ hollandite with stishovite in melt veins of the shocked meteorite Zagami (Langenhorst and Poirier 2000) supports this calculation. Although Tutti et al. (2001) showed that $KAlSi_3O_8$ hollandite is stable up to 95 GPa, representing a depth of 2200 km in the mantle, a study by Sueda et al. (2004) puts the upper P-stability limit of $KAlSi_3O_8$ hollandite at 22-24 GPa, where it transforms to a new phase, hollandite II. The locations of reaction (10) and (11) confirm that $KAlSi_3O_8$ hollandite is stable at pressures above 10 GPa. It appears $KAlSi_3O_8$ hollandite is stable down to depths of 400-660 km in the

transition zone of the Earth's mantle, followed by hollandite II at greater depths.

Besides occurrences in shocked meteorites, $KAlSi_3O_8$ hollandite has also been reported as an experimental run product between 8 and 11 GPa in bulk compositions corresponding to average continental crust, subducted terrigenous and pelagic sediment, basalts, and metapelites (Irifune et al. 1994; Domanik and Holloway 1996, 2000; Schmidt 1996; Ono 1998; Wang and Takahashi 1999). However, Si-wadeite has not yet been identified in any of these experiments or in natural occurrences. Wang and Takahashi (1999) argued that K might be selectively partitioned into pyroxene and/or garnet in potassic basalt, thus inhibiting the formation of Si-wadeite in that bulk composition. In the presence of water, reaction (9) will take place at much lower pressure than reaction (4), which also prevents the formation of Si-wadeite from sanidine.

ACKNOWLEDGMENTS

The authors are grateful to C. Manning of UCLA for providing 2 g of sanidine glass for use in this study. They also thank Z. Page and C. Henderson for their help in EMPA analysis, and R.C. Rouse for his help with XRD measurements. The authors acknowledge M. Akaogi and J. Konzett for their constructive reviews of the manuscript. This work was partly supported by Scott Turner Research Grant by the Department of Geological Sciences, University of Michigan to the senior author, and by NSF grants EAR96-28196, 99-11352, 00-87448 and 05-37068 to EJE. NSF grants EAR 03-10142

and 00-79827 to M. Hirschmann for the multianvil device at the University of Minnesota, and support of the Austrian granting agency for the PPMS at the University of Salzburg (grant P15880-N11) are also gratefully acknowledged.

Table 2.1 Average composition of $KAlSi_3O_8$ glass and $KAlSi_3O_8$ hollandite determined by EMP

Phase	SiO_2(wt %)	Al_2O_3	K_2O	MgO	Na_2O	FeO	Sum
$KAlSi_3O_8$ (glass)	64.57	17.63	16.92	0.01	0.01	0.02	99.16
StdDev (wt %)	0.38	0.15	0.48	0.01	0.02	0.03	
Cations per 8 O	3.018	0.971	1.009	0.001	0.001	0.001	5.001
$KAlSi_3O_8$ (hollandite)	64.30	18.34	17.36	0.04	0.04	0.19	100.27
StdDev (wt %)	0.64	0.44	0.32	0.02	0.04	0.09	
Cations per 8 O	2.983	1.003	1.027	0.003	0.004	0.007	4.989

Table 2.2 Heat capacity of $KAlSi_3O_8$ hollandite*

T (K)	C_p ($Jmol^{-1}K^{-1}$)	T (K)	C_p ($Jmol^{-1}K^{-1}$)	T (K)	C_p ($Jmol^{-1}K^{-1}$)
5.06	0.0177(6)	20.87	1.059(20)	86.45	35.52(40)
5.52	0.0231(6)	22.68	1.371(25)	93.95	41.36(43)
6.00	0.031(1)	24.65	1.792(37)	102.17	47.91(44)
6.52	0.038(1)	26.80	2.307(44)	111.41	55.13(46)
7.08	0.049(1)	29.14	2.986(58)	120.78	63.77(46)
7.69	0.059(1)	31.68	3.807(73)	131.31	73.05(48)
8.36	0.078(1)	34.45	4.810(89)	142.77	83.25(51)
9.08	0.096(2)	37.46	6.02(11)	155.22	94.20(50)
9.86	0.123(2)	40.74	7.48(14)	168.72	106.16(51)
10.72	0.158(3)	44.29	9.03(17)	183.49	118.93(51)
11.65	0.195(4)	48.15	11.00(21)	199.47	132.06(53)
12.67	0.247(5)	52.35	13.25(23)	216.98	145.75(54)
13.76	0.310(6)	56.92	15.87(26)	235.83	159.92(59)
14.96	0.395(7)	61.88	18.81(29)	256.48	174.27(55)
16.25	0.500(9)	67.28	22.16(34)	278.71	189.62(67)
17.67	0.638(11)	73.14	26.05(35)	303.10	202.66(70)
19.20	0.818(15)	79.52	30.30(39)		

*The C_p data were measured with PPMS on 17.9 mg sample material.

Table 2.3 Coefficients of the C_p polynomial $C_p = k_o + k_1T^{-0.5} + k_2T^{-2} + k_3T^{-3} + k_4T + k_5T^2 + k_6T^3$ derived by fitting the PPMS C_p data of $KAlSi_3O_8$ hollandite given in Table 2.2*

Formula weight	403.129 g/mol	
Sample weight	17.91 mg	
	Fit 1	Fit 2
k_6	1.3828E-04	1.3828E-04
T_1	5.18	4.63
k_o	3.8615E+00	-5.7192E+00
k_1	-9.3952E+00	1.2055E+01
k_2	4.0668E+01	-3.7451E+01
k_3	-7.4326E+01	5.7584E+01
k_4	-1.5636E-01	3.3438E-01
k_5	3.8436E-03	-1.3217E-02
k_6	8.4027E-05	3.2949E-04
T_2	33.55	24.83
k_2	-5.1104E+02	1.0604E+02
k_4	-7.3461E-02	-1.3806E-01
k_5	7.2435E-03	9.0294E-03
k_6	-1.8727E-05	-3.0671E-05
T_3	122.36	91.31
k_o	6.4504E+02	6.3640E+02
k_1	-8.2990E+03	-8.1129E+03
k_2	3.6393E+06	3.3807E+06
k_3	-1.3325E+08	-1.1687E+08
T_{ref}	298.15	298.15
C_p at 298	200.3(7)	200.2(7)
S°_{298}	147.45(19)	147.49(18)

*At the bottom of the table, heat capacity at 298.15 K and standard entropy S^o are additionally given (numbers in parenthesis is 1 standard deviation and apply to the last digits). Fit 1 and Fit 2 only differ by the choice of temperatures T_1, T_2 and T_3 at which the C_p data have been split into subsets.

Table 2.4 Phase property data used for phase boundary calculation. The numbers in parentheses are 2 standard deviations.

Phase*	$H^\circ_{f,298}$	S°_{298}	$Cp=c_1+c_2T^{-0.5}+c_3T^{-2}+c_4T^{-3}$ (J mol^{-1}K^{-1})			
	(kJmol^{-1})	(Jmol^{-1}K^{-1})	$c_1 \times 10^{-2}$	$c_2 \times 10^{-3}$	$c_3 \times 10^{-6}$	$c_4 \times 10^{-8}$
$KAlSi_3O_8$ (hol)	-3803.50[a]	166.2(0.4)[d]	3.896	-1.823	-12.934	16.307[f]
$K_2Si_4O_9$ (wd)	-4301.2(5.7)[b]	251(8)[e]	4.991	-4.350	0	0[b]
$KAlSi_3O_8{\cdot}H_2O$(kcym)	-4238.00[c]	284.0[c]	4.812	-2.981	-9.931	14.165[g]

Phase*	V°_{298}	$\alpha=a_0+a_1T$ (K^{-1})		K_{0T}	K'_{0T}
	(cm^3 mol^{-1})	a_0x10^5	a_1x10^8	(Gpa)	
$KAlSi_3O_8$ (hol)	71.28[h]	3.300	0[f]	180[l]	4[n]
$K_2Si_4O_9$ (wd)	108.44[i]	2.950	0[j]	90[m]	4[n]
$KAlSi_3O_8{\cdot}H_2O$(kcym)	114.37[g]	1.816	2.129[k]	45.1[g]	1.3[g]

[a] Modified from Akaogi et al. (2004);
[b] Fasshauer et al. (1998);
[c] Modified from Fasshauer et al. (1997);
[d] This study;
[e] Estimated from Holland (1989);
[f] Akaogi et al. (2004); [g] Fasshauer et al. (1997);
[h] Yamada et al. (1984);
[i] Swanson and Prewitt (1983);
[j] Swanson and Prewitt (1986);
[k] Calculated from Fasshauer et al. (1997);
[l] Zhang et al. (1993);
[m] Geisinger et al. (1987);
[n] Assumed.
* All the other phases involved in this study are from a modified Holland and Powell (1998) data base, called hp02ver.dat. More detailed information about hp02ver.dat can be found in http://www.perplex.ethz.ch/

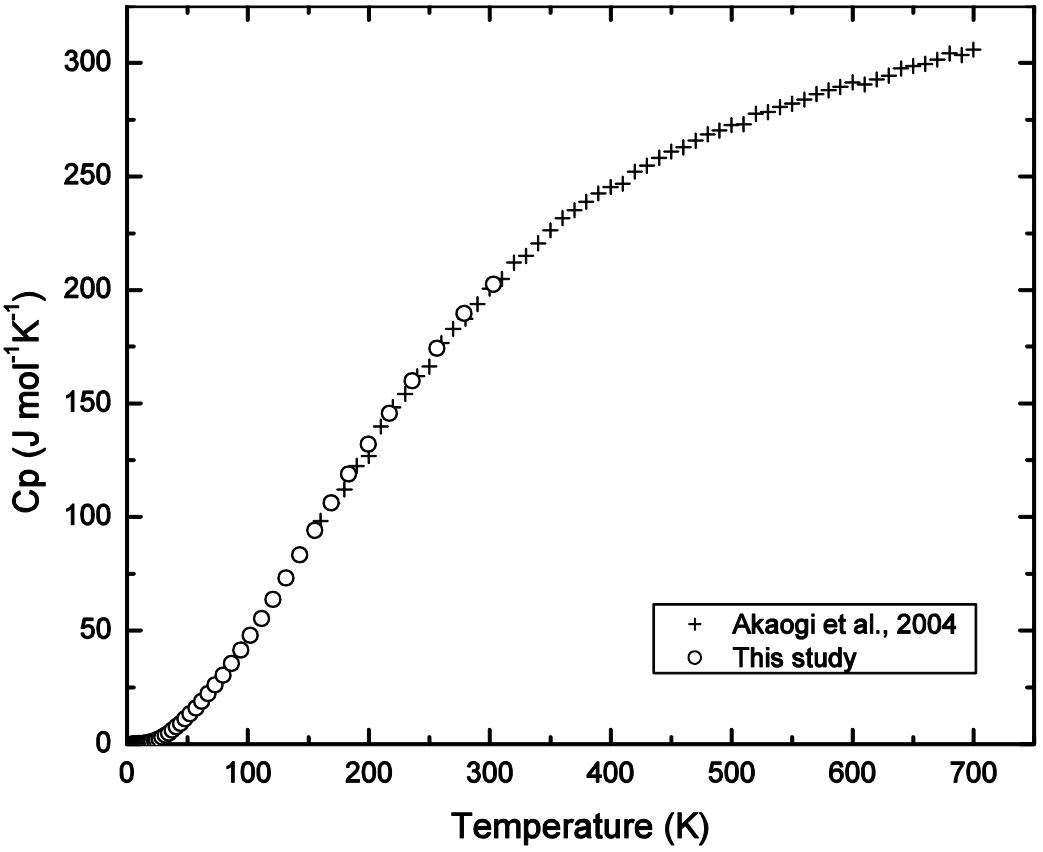

Fig. 2.1 Comparison of the low-T C_p of $KAlSi_3O_8$ hollandite measured using the PPMS calorimeter in this study with high-T C_p data from Akaogi et al. (2004)

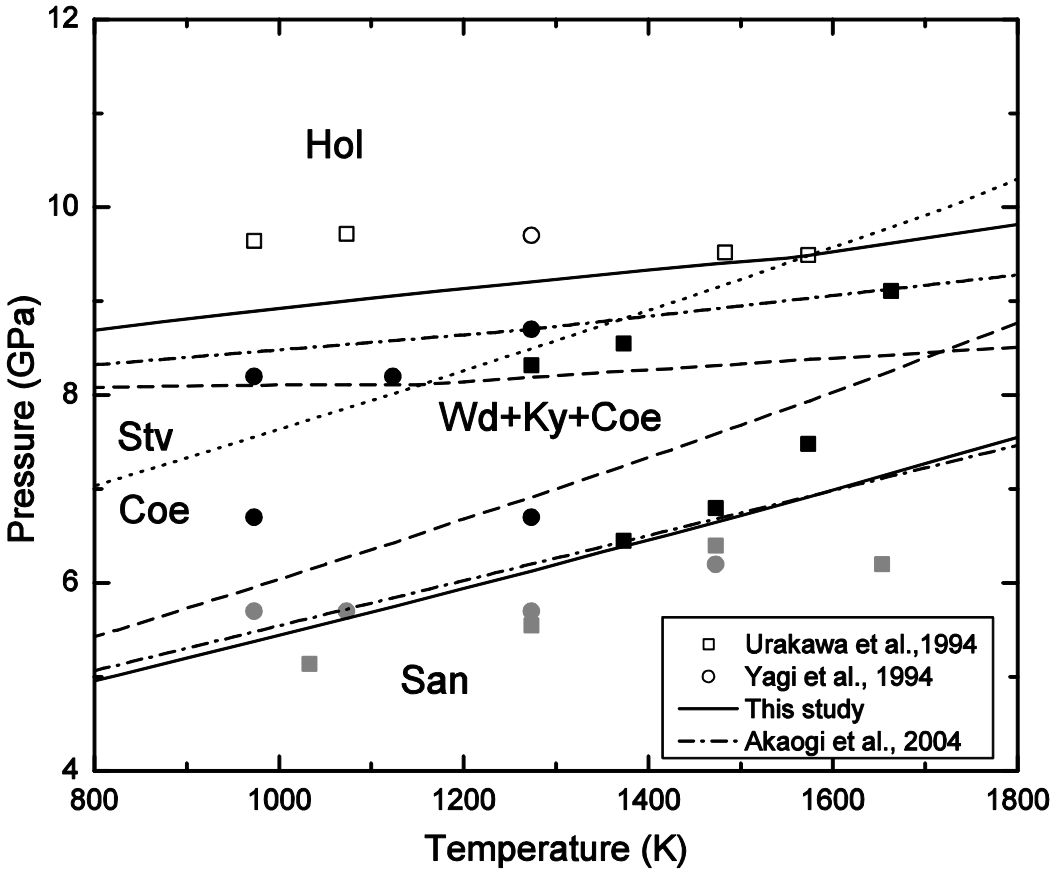

Fig. 2.2 Phase diagram of the system $KAlSi_3O_8$. The *dotted line* represents the coesite-stishovite transition boundary obtained with a modified Holland and Powell (1998) thermodynamic data base. *Dashed lines* show the phase boundaries calculated from $S^o_{298(Wd)}$ = 232 $Jmol^{-1}K^{-1}$ (Fasshauer et al., 1998). The *solid line* represents the phase boundaries calculated from $S^o_{298(Wd)}$ = 251 $Jmol^{-1}K^{-1}$ and modified enthalpy of $KAlSi_3O_8$ hollandite. *Dash-dotted lines* are the phase boundaries of Akaogi et al. (2004). *Circles* represent quench experimental runs by Yagi et al. (1994) after pressure correction, and *squares* are the in situ X-ray experimental runs by Urakawa et al. (1994). *Open, closed* and *shaded symbols* represent hollandite, Si-wadeite+kyanite+coesite (or stishovite), and sanidine, respectively. Hol $KAlSi_3O_8$ hollandite; Wd Si-wadeite; Ky kyanite; Coe coesite; Stv stishovite; San sanidine

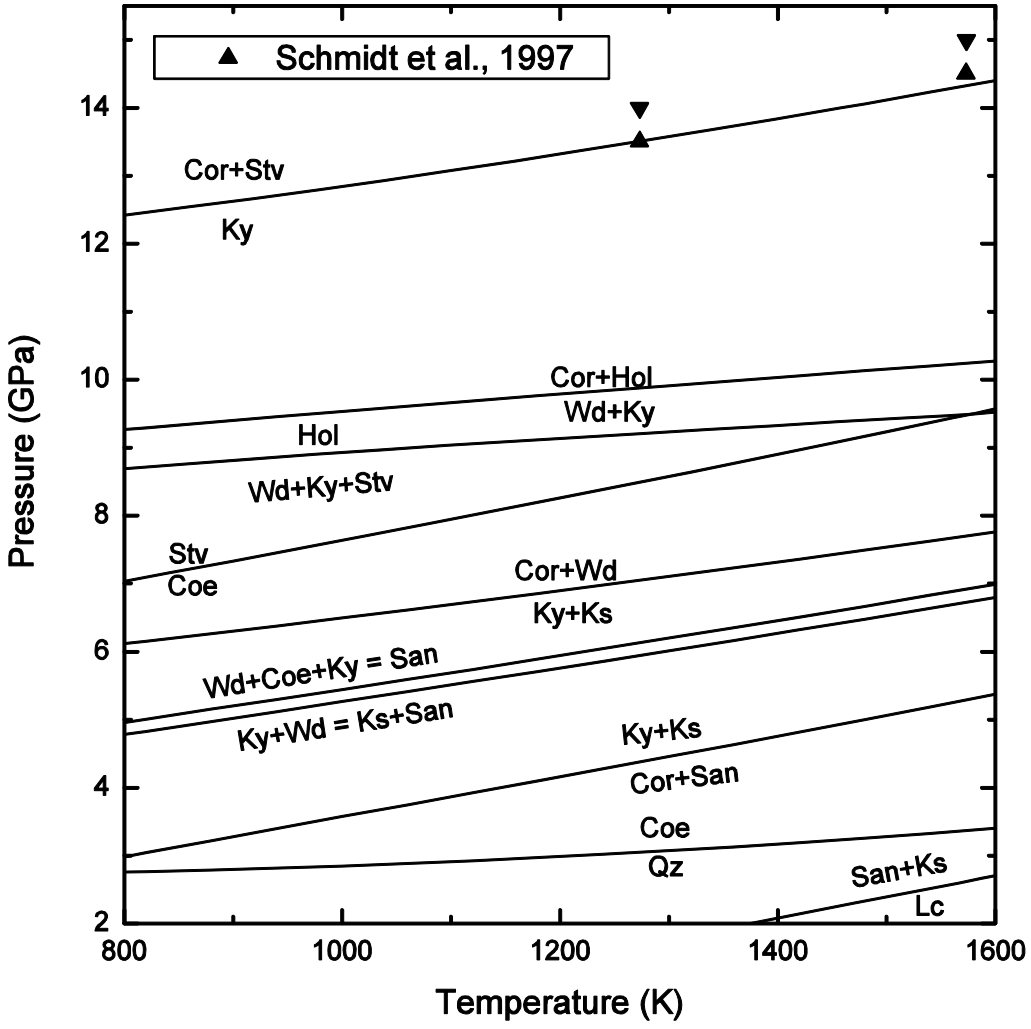

Fig. 2.3 Phase diagram of the system K_2O-Al_2O_3-SiO_2. *Triangles* represent the experimental results of Schmidt et al. (1997). Cor corundum; Ks kalsilite; Qz quartz; Lc leucite

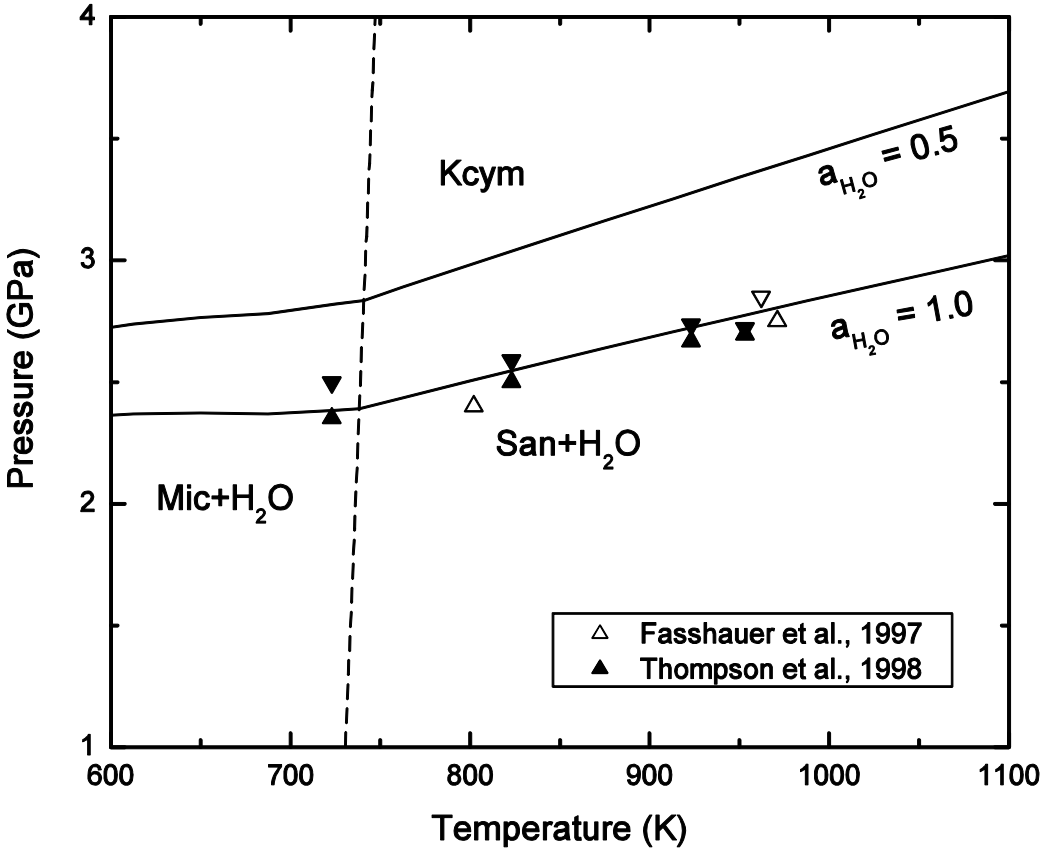

Fig. 2.4 Calculated P-T diagram for the formation of K-cymrite. The *open* and *closed triangles* represent the experimental reversals by Fasshauer et al. (1997) and Thompson et al. (1998), respectively. The *dashed line* represents the microcline-sanidine transition boundary. Kcym K-cymrite; Mic microcline

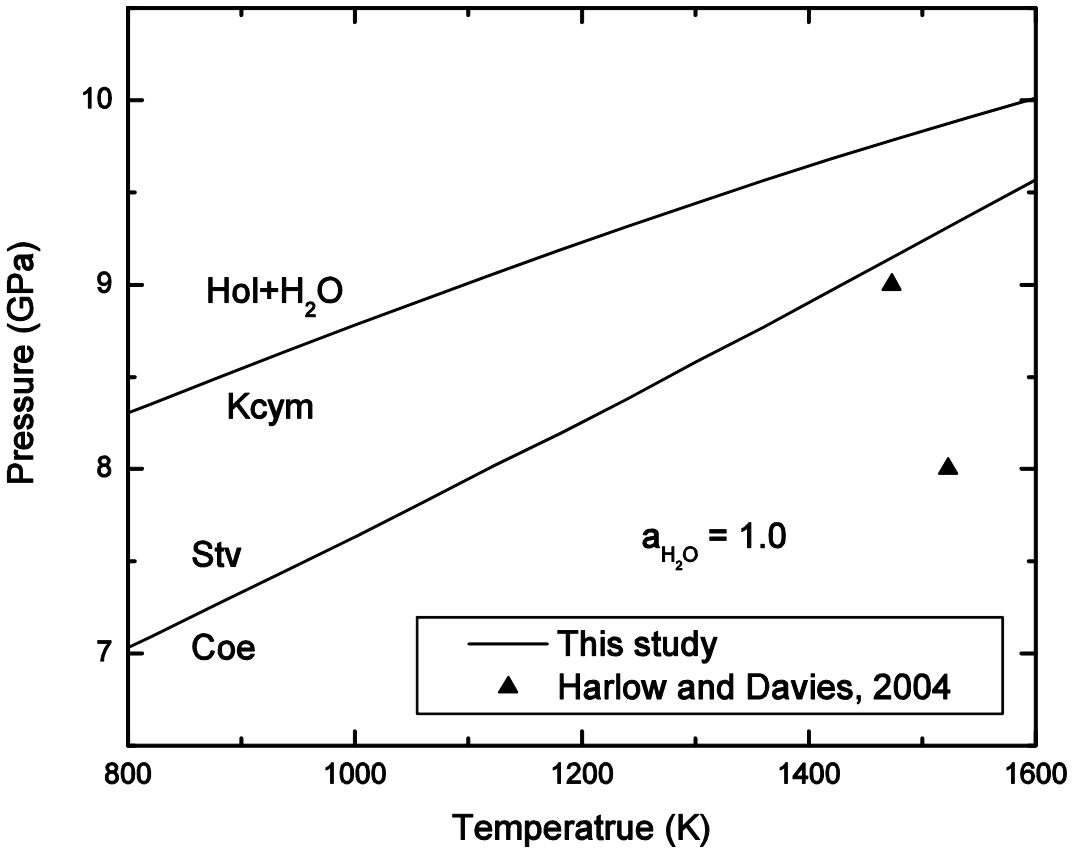

Fig. 2.5 Calculated P-T diagram for the dehydration reaction of K-cymrite into $KAlSi_3O_8$ hollandite. *Closed triangles* represent two experimental runs by Harlow and Davies (2004)

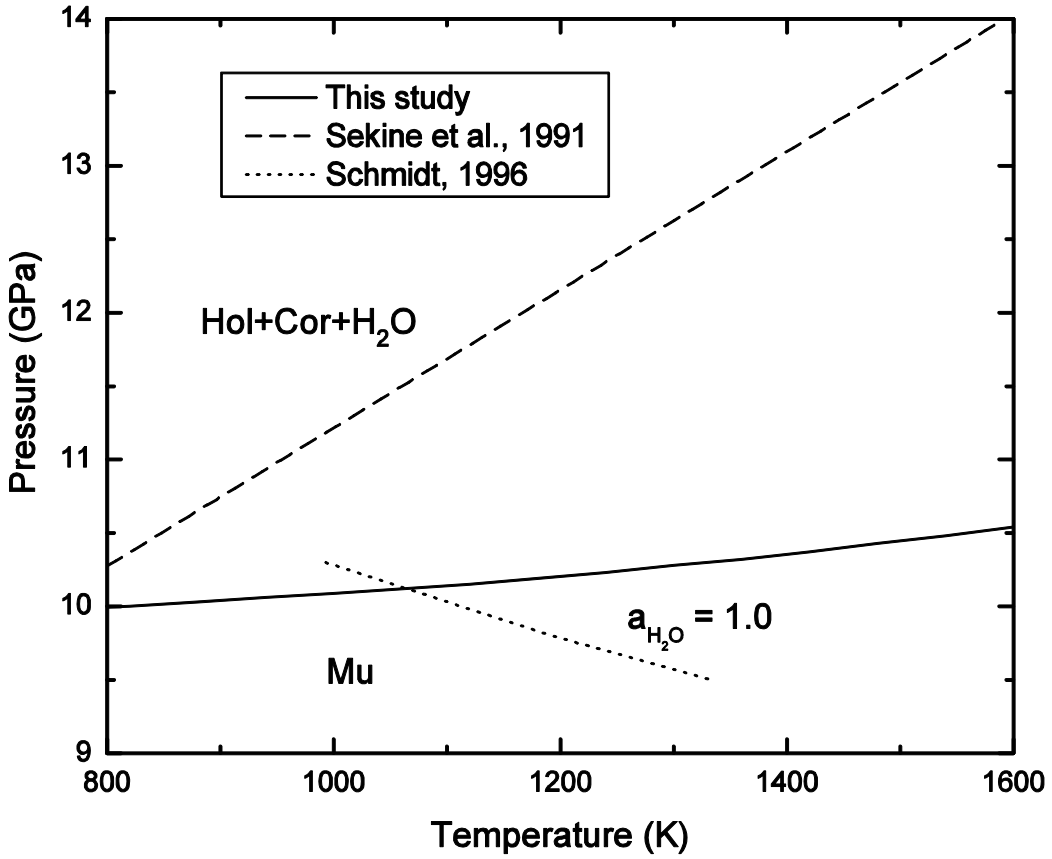

Fig. 2.6 Calculated P-T diagram for the dehydration reaction of muscovite into $KAlSi_3O_8$ hollandite + Al_2O_3 + H_2O. The *solid line* represents the calculated phase boundary in this study. The *dashed line* shows the calculated phase boundary by Sekine et al. (1991). The *dotted line* represents the breakdown reaction of phengite (a K-rich mica) by Schmidt (1996). Mu muscovite

REFERENCES

Akaogi M (2000) Clues from a shocked meteorite. Science 287:1602–1603

Akaogi M, Kamii N, Kishi A, Kojitani, H (2004) Calorimetric study on high–pressure transitions in $KAlSi_3O_8$. Phys Chem Minerals 31:85–91

Carpenter MA, Salje EKH (1994) Thermodynamics of non-convergent cation ordering in minerals: III. Order parameter coupling in potassium feldspar. Am Mineral 79:1084-1098

Chopin C (2003) Ultrahigh-pressure metamorphism: tracing continental crust into the mantle. Earth Planet Sci Lett 212:1–14

Connolly JAD (1990) Multivariable phase diagrams: an algorithm based on generalized thermodynamics. Am J Sci 290:666-718

Connolly JAD, Kerrick DM (1987) An algorithm and computer program for calculating composition phase diagrams. CALPHAD 11:1–55

Dachs E, Bertoldi C (2005) Precision and accuracy of the heat–pulse calorimetric technique: low temperature heat capacities of milligram–sized synthetic mineral samples. Eur J Mineral 17:251–259

Domanik KJ, Holloway JR (1996) The stability and composition of phengitic muscovite and associated phases from 5.5 to 11 GPa: implications for deeply subducted sediments. Geochim Cosmochim Acta 60:4133–4150

Domanik KJ, Holloway JR (2000) Experimental synthesis and phase relations of phengitic muscovite from 6.5 to 11 GPa in a calcareous metapelite from the Dabie Mountains, China. Lithos 52:51–77

Edwards RL, Essene EJ (1998) Pressure, temperature and C-O-H fluid fugacities across the amphibolite-granulite facies transition, NW Adirondack Mtns., NY. J Petrol 29:39–73

Fasshauer DW, Chatterjee ND, Marler B (1997) Synthesis, structure, thermodynamic properties and stability relations of K–cymrite, $KAlSi_3O_8 \cdot H_2O$. Phys Chem Minerals 24:455–462

Fasshauer DW, Wunder B, Chatterjee ND, Höhne GWH (1998) Heat capacity of wadeite–type $K_2Si_4O_9$ and the pressure–induced stable decomposition of K–feldspar. Contr Mineral Petrol 131:210–218

Faust J, Knittle E (1994) The equation of state, amorphization, and high–pressure phase diagram of muscovite. J Geophys Res 99:19,785–19,792

Geisinger KL, Ross NL, McMillan P, Navrotsky A (1987) Potassium silicate ($K_2Si_4O_9$): energetics and vibrational spectra of glass, sheet silicate, and wadeite–type phases. Am Mineral 72:984–994

Gillet P, Chen M, Dubrovinsky L, El Goresy A (2000) Natural $NaAlSi_3O_8$–hollandite in the shocked Sixiangkou meteorite. Science 287:1633–1636

Harlow GE, Davies R (2004) Status report on stability of K–rich phases at upper–mantle conditions. Lithos 77:647–653

Holland TJB (1989) Dependence of entropy on volume for silicate and oxide minerals: a review and a predictive model. Am Mineral 74:5–13

Holland TJB, Powell R (1991) A compensated-Redlich-Kwong (CORK) equation for volumes and fugacities of CO_2 and H_2O in the range 1 bar to 50 kbar and 100 – 1600ºC. Contr Mineral Petrol 109:265–273

Holland TJB, Powell R (1998) An internally consistent thermodynamic data set for phases of petrological interest. J Metam Geol 16:309–343

Hwang SL, Shen P, Chu H-T, Yui T-F, Liou JG, Sobolev NV, Zhang R-Y, Shatsky VS, Zayachkovsky AA (2004) Kokchetavite: a new potassium-feldspar polymorph from the Kokchetav ultrahigh-pressure terrane. Contr Mineral Petrol 148:380–389

Irifune T, Ringwood RE, Hibberson WO (1994) Subduction of continental crust and terrigenous and pelagic sediments: and experimental study. Earth Planet Sci Lett 126:351–368

Kaneko Y, Maruyama S, Terabayashi M, Yamamoto H, Ishikawa M, Anma R, Parkinson CD, Ota T, Nakajima Y, Katayama I, Yamamoto J, Yamauchi K (2000) Geology of the Kokchetav UHP-HP metamorphic belt, Northern Kazakhstan. Island Arc 9:264-283

Kimura M, Chen M, Yoshida Y, El Goresy A, Ohtani E (2004) Back–transformation of high–pressure phases in a shock melt vein of an H–chondrite during atmospheric

passage: implications for the survival of high–pressure phases after decompression. Earth Planet Sci Lett 217:141–150

Kinomura N, Koizumi M, Kume S (1977) Crystal structures of phases produced by disproportionation of K–feldspar under pressure. In: Manghnani MH, Akimoto S (eds) High–Pressure Research: Application in Geophysics. Academic Press, New York, pp 183–189

Kinomura N, Kume N, Koizumi M (1975) Stability of $K_2Si_4O_9$ with wadeite type structure. Proc 4th Inter Conf High Pressure Sci Tech, pp 211–214

Konzett J, Fei Y (2000) Transport and storage of potassium in the earth's upper mantle and transition zone: an experimental study to 23 GPa in simplified and natural bulk compositions. J Petrol 41:583–603

Langenhorst F, Poirier JP (2000) "Eclogitic" minerals in a shocked basaltic meteorite. Earth Planet Sci Lett 176:259–265

Lashley JC, Hundley MF, Migliori A, Sarrao JL, Pagliuso PG, Darling TW, Jaime M, Cooley JC, Hults WL, Morales L, Thoma DJ, Smith JL, Boerio-Goates J, Woodfield BF, Stewart GR, Fisher RA, Phillips NE (2003) Critical examination of heat capacity measurements made on a Quantum Design physical property measurement system. Cryogenics 43:369–378

Liu L (1978) High–pressure phase transitions of kalsilite and related potassium bearing aluminosilicates. Geochemical Journal 12:275–277

Massonne H-J (1992) Evidence for low-temperature ultrapotassic siliceous fluids in subduction zone environments from experiments in the system K_2O-MgO-Al_2O_3-SiO_2-H_2O (KMASH). Lithos 28:421-434

Massonne H-J, Nasdala L (2003) Characterization of an early metamorphic stage through inclusions in zircon of a diamondiferous quartzofeldspathic rock from the Erzgebirge, Germany. Am Mineral 88:883–889

Nishiyama N, Rapp RP, Irifune T, Sanehira T, Yamazaki D, Funakoshi K (2005) Stability and P-V-T equation of state of $KAlSi_3O_8$-hollandite determined by in situ X-ray observations and implications for dynamics of subducted continental crust material. Phys Chem Mineral 32:627–637

Ono S (1998) Stability limits of hydrous minerals in sediment and mid–ocean ridge basalt compositions: implications for water transport in subduction zones. J Geophys Res 103:18,253–18,267

Prewitt CT, Downs RT (1998) High-pressure crystal chemistry. Rev Mineral 37: 283–312

Ringwood AE (1975) Composition and petrology of the Earth's mantle. McGraw-Hill, New York, 618 pp

Ringwood AE, Reid AF, Wadsley AD (1967) High–pressure $KAlSi_3O_8$, an alumino-silicate with sixfold coordination. Acta Crystallogr 23:1093–1095

Robie RA, Hemingway BS (1995) Thermodynamic properties of minerals and related substances at 298.15 K and 1 bar (10^5 Pascals) pressure and at higher temperatures. US Geol Surv 2131, 461 pp 461

Schertl H-P, Schreyer W, Chopin C (1991) The pyrope-coesite rocks and their country rocks at Parigi, Dora Maira massif, western Alps: detailed petrography, mineral chemistry and PT-path. Contr Mineral Petrol 108:1-21

Schmidt M (1996) Experimental constraints on recycling of potassium from subducted oceanic crust. Science 272:1927–1930

Schmidt MW, Poly S, Comodi P, Zanazzi PF (1997) High-pressure behavior of kyanite: Decomposition of kyanite into stishovite and corundum. Am Mineral 82:460–466

Seki Y, Kennedy GC (1964) The breakdown of potassium feldspar, $KAlSi_3O_8$, at high temperatures and high pressures. Am Mineral 49:1688–1706

Sekine T, Rubin AM, Ahrens TJ (1991) Shock wave equation of state of muscovite. J Geophys Res 96:19,675–19,680

Sharp ZD, Essene EJ, Hunziker JC (1993) Stable isotope geochemistry and phase equilibria of coesite-bearing whiteschists, Dora Maira massif, western Alps. Contr Mineral Petrol 114:1-12

Sueda Y, Irifune T, Nishiyama N, Rapp RP, Ferroir T, Onozawa T, Yagi T, Merkel S, Miyajima N, Funakoshi K (2004) A new high-pressure form of $KAlSi_3O_8$ under lower mantle conditions. Geophys Res Lett 31, L23612, doi:10.1029/2004GL021156

Swanson DK, Prewitt CT (1983) The crystal structure of $K_2Si^{VI}–Si^{IV}{}_3O_9$. Am Mineral 68:581–585

Swanson DK, Prewitt CT (1986) Anharmonic thermal motion in $K_2Si^{VI}–Si^{IV}{}_3O_9$. Eos 67:369

Thompson P (1994) The sanidine-'sanidine hydrate' reaction boundary. Mineral Mag 58A:897

Thompson P, Parsons I, Graham CM, Jackson B (1998) The breakdown of potassium feldspar at high water pressures. Contr Mineral Petrol 130:176–186

Tomioka N, Mori H, Fujino K (2000) Shock–induced transition of $NaAlSi_3O_8$ feldspar into a hollandite structure in a L6 chondrite. Geophys Res Lett 278:3997–4000

Tutti F, Dubrovinsky LS, Saxena SK, Carlson S (2001) Stability of $KAlSi_3O_8$ hollandite-type structure in the Earth's lower mantle conditions. Geophys Res Lett 28:2735–2738

Urakawa S, Kondo T, Igawa N, Shimomura O, Ohno H (1994) Synchrotron radiation study on the high-pressure and high-temperature phase relations of $KAlSi_3O_8$. Phys Chem Mineral 21:387–391

Valley JW, Bohlen SR, Essene EJ, Lamb W (1990) Metamorphism in the Adirondacks. II. The role of fluids. J Petrol 31:555–596

Wang W, Takahashi E (1999) Subsolidus and melting experiments of a K-rich basaltic composition to 27 GPa: implication for the behavior of potassium in the mantle. Am Mineral 84:357–361

Yagi A, Akimoto S (1976) Direct determination of coesite-stishovite transition by in situ X-ray measurements. Tectonophys 35:259–586

Yagi A, Suzuki T, Akaogi M (1994) High pressure transitions in the system $KAlSi_3O_8$ – $NaAlSi_3O_8$. Phys Chem Minerals 21:12–17

Yamada H, Matsui Y, Ito E (1984) Crystal–chemical characterization of $KAlSi_3O_8$ with hollandite structure. Mineral J 12:29–34

Yoshida D, Hirajima T, Ishiwatari A (2004) Pressure-temperature path recorded in the Yangkou garnet peridotite, in Su-Lu ultrahigh-pressure metamorphic belt, eastern China. J Petrol 45:1125–1145

Zhang J, Ko J, Hazen RM, Prewitt CT (1993) High–pressure crystal chemistry of $KAlSi_3O_8$ hollandite. Am Mineral 78:493–499

Zhang J, Li B, Utsumi W, Liebermann RC (1996) In Situ X-ray observations of the coesite-stishovite transition: reversed phase boundary and kinetics. Phys Chem Minerals 23:1–10

CHAPTER III

HEAT CAPACITY AND PHASE EQUILIBRIA OF WADEITE-TYPE $K_2Si_4O_9$

ABSTRACT

The low-temperature heat capacity (C_p) of Si-wadeite ($K_2Si_4O_9$) synthesized with a piston cylinder device was measured over the range of 5–303 K using the heat capacity option of a physical properties measurement system. The entropy of Si-wadeite at standard temperature and pressure calculated from the measured heat capacity data is 253.8 ± 0.6 $Jmol^{-1}K^{-1}$, which is considerably larger than some of the previous estimated values. The calculated phase transition boundaries in the system K_2O-Al_2O_3-SiO_2 are generally consistent with previous experimental results. Together with our calculated phase boundaries, seven multi-anvil experiments at 1400 K and 6.0–7.7 GPa suggest that no equilibrium stability field of kalsilite + coesite intervenes between the stability field of sanidine and that of coesite + kyanite + Si-wadeite, in contrast to previous predictions. First-order approximations were undertaken to calculate the phase diagram in the system $K_2Si_4O_9$ at lower pressure and temperature. Large discrepancies were shown between the calculated diagram compared with previously published versions, suggesting that further experimental or/and calorimetric work is needed to better constrain the low pressure

phase relations of the $K_2Si_4O_9$ polymorphs.

INTRODUCTION

Kinomura et al. (1975) first reported that a new crystalline phase of $K_2Si_4O_9$, isostructural with wadeite ($K_2ZrSi_3O_9$), would form as one of the decomposition products of potassium feldspar with increasing pressure. Inoue et al. (1998) showed that $K_2Si_4O_9$ wadeite (Si-wadeite) was one of the decomposition products of K-amphibole ($K_2CaMg_5Si_8O_{22}(OH)_2$) at 14–16 GPa and above 1473 K. Tronnes (2002) also reported Si-wadeite was one of the decomposition products of K-richterite ($KNaCaMg_5Si_8O_{22}(OH)_2$) at 1773 K above 10 GPa. Similar to the Zr atoms in wadeite ($K_2ZrSi_3O_9$), one-fourth of the Si atoms in Si-wadeite are in octahedral sites (Kinomura et al. 1975). These octahedral Si atoms serve as the bridge to connect the three-membered rings of SiO_4 tetrahedra, while the K atoms occupy the large cages between the layers of those rings (Kinomura et al. 1977; Swanson and Prewitt 1983). Experimental studies by Urakawa et al. (1994) and Yagi et al. (1994) confirmed the report by Kinomura et al. (1975) that potassium feldspar transforms to Si-wadeite, kyanite (Al_2SiO_5) and coesite (SiO_2) at about 6 GPa and at 1300 K, and these three phases reunite together into $KAlSi_3O_8$ hollandite when pressure increases to 9 GPa. With all the Si atoms in octahedral sites, the structure of $KAlSi_3O_8$ hollandite can be viewed as the K atoms occupying the large tunnel formed by the double chains of edge-sharing $(Si,Al)O_6$ octahedra (Ringwood et al. 1967; Yamada et al. 1984; Zhang et al. 1993).

Geisinger et al. (1987) performed calorimetric measurements on Si-wadeite and $K_2Si_4O_9$ glass. Fasshauer et al. (1998) measured the heat capacity data of Si-wadeite in the temperature range 195–598 K. They also generated an internally consistent thermodynamic data set that suggested sanidine would decompose first into kalsilite ($KAlSiO_4$) + coesite at about 5 GPa when temperature is higher than 823 K. Akaogi et al. (2004) measured the enthalpies of Si-wadeite and $KAlSi_3O_8$ hollandite using high-temperature solution calorimetry, based on which the enthalpy of formation ($H^\circ_{f,\,298}$) of Si-wadeite was derived by Xu et al. (2005) as −4288.7 ± 5.1 kJmol^{-1}. The heat capacity of $KAlSi_3O_8$ hollandite was measured by differential scanning calorimetry (DSC) from 160 K to 700 K (Akaogi et al. 2004) and by PPMS from 5 K to 303 K (Yong et al. 2006). However, the low temperature heat capacity of Si-wadeite had not been measured, and therefore the entropy of Si-wadeite could not be calculated, although several estimates have been proposed (Geisinger et al. 1987; Fasshauer et al. 1998; Yong et al. 2006; cf. Table 3.1). Due to the lack of entropy data for Si-wadeite, an evaluation of phase equilibrium relations totally independent of high temperature and high pressure phase equilibrium experiments has not been applied in the system K_2O–Al_2O_3–SiO_2. In this study, the heat capacity of Si-wadeite was measured from 5 K to 303 K by a physical properties measurement system (PPMS, produced by Quantum Design®), and the standard entropy of Si-wadeite was calculated from the measured heat capacity data. The phase relations in the system K_2O–Al_2O_3–SiO_2 were studied including the new thermodynamic data and some additional experiments were undertaken in this system

with a multi-anvil device.

EXPERIMENTAL PROCEDURES

Sample Synthesis and Phase Equilibrium Experiments

The Si-wadeite, $KAlSi_3O_8$ sanidine and $KAlSiO_4$ kalsilite were synthesized using an end-loaded piston cylinder apparatus with 12.7 mm furnace assemblies and pistons. In each case, a single experimental run produced enough material for all of the phase equilibrium experiments, and an additional run was taken to make Si-wadeite for the calorimetric measurement. About 30 mg powdered starting material was put into 4 mm Pt capsule, which was inserted into a graphite furnace and $BaCO_3$ pressure medium. The temperature was controlled by a $W_3Re_{97}/W_{25}Re_{75}$ thermocouple, which was located above the sample capsule and was isolated from the capsule by a 1 mm disk of low density MgO extrusion. Details of pressure and temperature calibrations for this apparatus are given in Xirouchakis et al. (2001). The pressure and temperature uncertainties are believed to be ±0.1 GPa and ±12 ºC, respectively (Xirouchakis et al. 2001). The run products of these experiments were examined by a Scintag Powder XRD machine, and their average compositions were determined using a Cameca SX-100 electron microprobe (EMP) and given in Table 3.2. It is very common to find crystals of the synthesized phases larger than 5×5 μm^2, even as large as 20×20 μm^2, which should be large enough for reliable EMP analyses. The column conditions for the EMP were: accelerating voltage 15 kV, beam current 10 nA or 4 nA, peak counting time 10 s,

background counting time 5 s, beam scan area 2×2 μm^2. Natural K-feldspar (K, Al) and Tuburon albite (Si) were used as standards in the analyses.

The starting material for Si-wadeite was $K_2Si_4O_9$ glass, prepared from a homogenized mixture of K_2CO_3 and SiO_2 at 1:4 molar ratio. The mixture was first heated at 973 K for 5 days and then kept at 1173 K for 24 hours before quenching to glass. The glass starting material was held in the piston cylinder at 3 GPa and 1273 K for 6 days, quenched at 3 GPa, and recovered to ambient pressure. The run product was confirmed as Si-wadeite by powder X-ray diffraction and EMP analysis (Table 3.2). The hexagonal lattice parameters of the synthesized Si-wadeite were determined using the Scintag Crystallography program as a = 6.6102(4) Å and c = 9.5061 (7) Å, which are comparable to the values of a = 6.6126(9) Å and c = 9.5101 (6) Å by Fasshauer et al. (1998) and a = 6.614(1) Å and c = 9.512 (1) Å, by Akaogi et al. (2004).

The sanidine used for the phase equilibrium experiments was synthesized from powdered $KAlSi_3O_8$ glass provided by Craig Manning at UCLA. The powdered glass was held at 3.2 GPa and 1473 K for 48 hours before it was quenched at 3.2 GPa. Powder X-ray diffraction and EMP analysis (Table 3.2) confirmed that the synthetic material is pure sanidine.

The starting material for $KAlSiO_4$ kalsilite was made from a mixture of K_2CO_3, Al_2O_3 and SiO_2 at 1:1:2 molar ratio. The mixture was finely powdered and then heated at 973 K for 6 days for decarbonation. This mixture was held at 3.2 GPa and 1273 K for 69 hours for complete reaction. The run product was examined by powder X-ray diffraction

and EMP analysis (Table 3.2), confirming kalsilite phase of $KAlSiO_4$ composition with a small amount of corundum (<5%). The unit cell parameters of the hexagonal kalsilite synthesized in this study were determined as a = 5.1614(3) Å and c = 8.7071 (9) Å, comparable to the values of a = 5.1627(3) Å and c = 8.7115 (6) Å by Fasshauer et al. (1998).

Coesite was synthesized using the 1000-ton Walker-type multi-anvil (MA) device at the University of Minnesota. In order to produce sufficient quantities of coesite for the phase equilibrium experiments in a single synthesis run, the standard "12-TEL" assembly used at the University of Minnesota was modified to include a 4.8 mm diameter graphite heater, in which it is possible to fit a capsule with a larger diameter than the usual 1.5 or 2 mm. The assembly consisted of tungsten carbide anvils with 12 mm truncations, a cast MgO-Al_2O_3-SiO_2-Cr_2O_3 octahedron with integral gaskets, a 4.8 mm diameter graphite heater, 3 mm Au capsule and a $W_3Re_{97}/W_{25}Re_{75}$ thermocouple. About 35 mg of pure quartz powder (99.995% SiO_2) was used as the starting material, which was subjected to 6 GPa and 1573 K for 6 hours. Powder X-ray diffraction study confirmed single phase coesite in the run product.

A natural white kyanite sample from Central Alps, Styria, Austria, was used for the phase equilibrium experiments.. Powder X-ray diffraction analyses of the kyanite revealed very weak peaks belonging to chlorite or muscovite; however, back scattered electron (BSE) image and EMP analyses didn't reveal any chlorite or muscovite. The slight amount of chlorite or muscovite in kyanite is assumed negligible and should not

affect the results of the phase equilibrium experiments. The average composition of this kyanite is given in Table 3.2.

The aforementioned MA device was used to perform the phase equilibrium experiments. The experimental assemblage was the same as that described above, except that the heater and capsule diameters were 4 mm and 1.6 mm, respectively. The force–pressure relationship for this 12-TEL assembly was determined using 298 K fixed points of the Bi I–II and Bi III–V transitions (Piermarini and Block 1975) and by multiple reversed brackets of high temperature phase transitions. The fixed points that define the force pressure curve used in this study are those of quartz–coesite at 973, 1273 and 1473 K (Bose and Ganguly 1995), Fe_2SiO_4 olivine–spinel at 1273 K (Yagi et al. 1987), $CaGeO_3$ garnet–perovskite at 1273 K (Susaki et al. 1985), and coesite–stishovite at 1273, 1373 and 1473 K (Zhang et al. 1993). Multiple 15-20 tonne brackets of these phase transitions define a self-consistent calibration curve (Dasgupta et al. 2004), on the basis of which we estimate uncertainty in pressure to be ±0.3 GPa. The thermal profile of the 12-TEL assembly has been evaluated using enstatite-diopside thermochemistry (Carlson and Lindsley 1988). At a nominal experimental temperature of 1773 K a total variation of 36 K was measured throughout a 2 mm diameter Pt capsule. An additional series of experiments to determine the melting point of titanite indicate that at >1973 K, less than 40 K increase in nominal experimental temperature was required to transform the entire contents of a 2 mm capsule from solid to liquid, in good agreement with the thermometry results. We therefore estimate that temperature gradients are < 20 K/mm.

Two sets of starting materials were used in this study. The first one is a mixture of sanidine, kalsilite and coesite at 1:1:2 nominal molar ratio, and the second one is a mixture of kalsilite, coesite, Si-wadeite and kyanite with a molar ratio of ~ 2:3:1:1. Due to the limitations of precision in weighing, both mixtures included a slight excess of coesite. The starting material was homogenized by grinding under ethyl alcohol in an agate pestle and mortar and examined by powder X-ray diffraction before loading into the capsule. About 4−5 mg starting material was loaded into the capsule for each experiment. After being held at the desired P-T condition for 12−96 hours, experiments were terminated by turning off the power supply to the heater and slowly depressurized to ambient pressure. Capsules were retrieved and opened from the end that was adjacent to the thermocouple junction during the experiment. Run products were extracted from the part of the capsule that was closest to the thermocouple junction and examined by powder X-ray diffraction. Since the analyzed run products were located with 1 mm of the thermocouple junction we expect the uncertainty in temperature to be better than ±20 K.

Heat Capacity Measurement

The heat capacity at constant pressure (C_p) of Si-wadeite in the temperature range of 5–303 K was measured at 1 atm using the heat capacity option of the PPMS at Salzburg University in Austria. A powdered Si-wadeite sample (21.4 mg) was sealed into a small Al pan with a lid and placed on a 4×4 mm^2 wide sapphire platform that has a thermometer and a heater attached to the lower side. Two runs were undertaken to collect

the C_p data from 5 K to 303 K. In the first run, C_p data were collected at 60 different temperatures with a logarithmic spacing whereas a linear spacing was used in the second run. Three measurements were performed at each temperature. Since it has been demonstrated that heat capacity values measured with the PPMS upon cooling compared well to those measured upon heating (Dachs and Bertoldi 2005), the C_p data were measured only upon cooling. More detailed descriptions of the method including discussions of the precision and accuracy of the C_p measurement by PPMS are given by Lashley et al. (2003) and Dachs and Bertoldi (2005). Other C_p data obtained in the same facility have been used to calculate phase equilibria at high pressures and temperatures (Yong et al. 2006, 2007; Manon et al. 2007).

RESULTS AND DISCUSSION

Heat Capacity and Entropy of Si-wadeite

The measured heat capacity (C_p) data of Si-wadeite as a function of temperature are listed in eTable 1 and shown in Table 3.3 and Fig. 3.1. The C_p data of Si-wadeite from 195 K to 598 K by Fasshauer et al. (1998) are also plotted in Fig. 3.1 for comparison. The two sets of data generally agree with each other in the overlapping region. The entropy of Si-wadeite at standard temperature and pressure (STP) was obtained by fitting the C_p data in Table 3.3 as a general polynomial, $C_p = k_0 + k_1T^{-0.5} + k_2T^{-2} + k_3T^{-3} + k_4T + k_5T^2 + k_6T^3$ using the function LinearFit of the Experimental Data Analyst Package of Mathematica®. The C_p data were split into three temperature regions with some overlaps

and each region was fitted slightly differently in terms of the C_p polynomial. The complete polynomial given above was only used for fitting the intermediate temperature region while $C_p = k_4T + k_6T^3$ and $C_p = k_0 + k_1T^{-0.5} + k_2T^{-2} + k_3T^{-3}$ were used for fitting the low temperature and high temperature regions, respectively. The C_p data were evaluated below 5 K by extrapolation from 5 to 0 K in the form of $C_p = k_6T^3$. The fitted C_p coefficients and the interval temperature boundaries are given in Table 3.4, and the entropy of Si-wadeite at STP was calculated to be 253.8 ± 0.6 $Jmol^{-1}K^{-1}$ (error is two standard deviations) by integration of these fitted polynomials. It was shown that the entropy at STP varies insignificantly (only in the second digit of the decimal) upon choosing different splitting temperatures for the C_p data (Yong et al. 2006). The uncertainty in the entropy at STP was estimated by a Monte Carlo technique; a detailed description of error estimation was given by Dachs and Geiger (2006).

As shown in Table 3.1, the entropy of Si-wadeite calculated from the C_p data is in excellent agreement with the estimated value of 251 ± 8 $Jmol^{-1}K^{-1}$ by Yong et al. (2006), strongly supporting the reliability of the entropy estimation method used by Holland (1989). However, the calorimetrically determined entropy of Si-wadeite in this study is considerably larger than the entropy value of 198.9 ± 4.0 $Jmol^{-1}K^{-1}$ calculated from spectroscopic data (Geisinger et al. 1987). It is also larger than the estimated value of 232 ± 10 $Jmol^{-1}K^{-1}$ based on an internally consistent thermodynamic data base by Fasshauer et al. (1998). The good agreement of our C_p data with that of Fasshauer et al. (1998) in the overlapping region and with entropy estimates made by Yong et al. (2006)

provides reasonable support for the calculated entropy value of Si-wadeite in this study.

Phase Equilibria in K_2O-Al_2O_3-SiO_2 System

The computer program Perple_x (Connolly and Kerrick 1987; Connolly 1990) was used to calculate the phase boundaries. A modified Holland and Powell (1998) data base is used for the well established phases, and the thermodynamic data and their sources for $KAlSi_3O_8$ hollandite and Si-wadeite are given in Table 3.5. The transition boundary of a certain reaction is defined by the following equation:

$$\Delta G(P,T) = \Delta G_T^\circ + \int_{1atm}^{P} \Delta V(P',T)dP' = 0 \qquad (1)$$

where $\Delta G(P,T)$ and $\Delta V(P,T)$ are Gibbs free energy and molar volume change of reaction at pressure P and temperature T, respectively. ΔG_T° is the Gibbs free energy change at 1 atm and temperature T, and its temperature dependence is corrected using the heat capacity data of the relevant phases. The temperature dependence of the molar volume, $V^\circ(T)$, is given by

$$V^\circ(T) = V_{298}^\circ\left(1 + \int_{298}^{T} \alpha dT\right) \qquad (2)$$

where V_{298}° and α are the molar volume at standard state and thermal expansion, respectively. The pressure dependence of the molar volume was expressed by the Murnaghan equation of state:

$$V(T,P) = V^\circ(T)\left(1 + \frac{K'}{K_T}P\right)^{-\frac{1}{K'}} \qquad (3)$$

where K_T and K' are the isothermal bulk modulus and its pressure derivative at

temperature *T*, respectively.

The upper stability of sanidine and the lower stability of $KAlSi_3O_8$ hollandite are defined by reaction (4) and (5), respectively. Fig. 3.2 shows the calculated phase boundaries for these two reactions:

2 sanidine = Si-wadeite + kyanite + coesite (4)

Si-wadeite + kyanite + coesite/stishovite = 2 $KAlSi_3O_8$ hollandite (5)

Compared to the experimentally determined phase boundaries by Yagi et al. (1994, dashed lines in Fig. 3.2, after pressure recalibration by Akaogi et al. 2004) and by Urakawa et al. (1994, dotted lines in Fig. 3.2), our calculated transition boundary (solid lines in Fig. 3.2) for reaction (4) has a much steeper slope and is consistent with their boundaries within ±0.8 GPa. The phase boundary by Akaogi et al. (2004, lower dash-dot line in Fig. 3.2) has a very similar slope to that of our study, and only differs in its locus by ~0.1 - 0.2 GPa. Our calculated phase transition boundary of reaction (5) is slightly above the coesite–stishovite transition boundary, 0.2~0.4 GPa higher than the experimental studies by Yagi et al. (1994) and Urakawa et al. (1994). The differences between this study and previous experiments can be explained by the pressure and temperature uncertainties of those experiments as well as the uncertainties of the thermodynamic data, especially the relatively large uncertainties of the enthalpy values. Fig. 3.3 shows the experimental data of Yagi et al. (1994, after pressure recalibration by Akaogi et al. 2004) and Urakawa et al. (1994) as well as the uncertainties of enthalpy data (Akaogi et al. 2004). As shown in Fig. 3.3, all the experimental syntheses of Yagi et

al. (1994) and the reversals of Urakawa et al. (1994) for reaction (4) agree with our calculation within one standard deviation (lighter shaded area). For reaction (5), except for one experimental run by Urakawa et al. (1994), all the other results are consistent with our calculated phase boundary within one standard deviation. That exceptional experiment at 1573 K and 9.49 GPa of Urakawa et al. (1994) is located inside the two standard deviation region of our calculation (darker shaded area, Fig. 3.3). Therefore, the thermodynamic data on Si-wadeite is considered to be in agreement with currently available experimental studies on its stability.

Fasshauer et al. (1998) suggested a stable region of kalsilite + coesite at temperature above 823 K located between the field of sanidine and that of Si-wadeite + coesite + kyanite (Fig. 3.4). They suggested that sanidine would decompose into kalsilite + coesite instead of Si-wadeite + coesite + kyanite at lower pressures, which is in disagreement with our calculations. One reason that may account for this discrepancy is the different entropy values of Si-wadeite between these two studies. A much lower entropy value for Si-wadeite derived from an internally consistent thermodynamic data set, 232.1 ± 10.4 $Jmol^{-1}K^{-1}$, was used in their study. As our entropy value for Si-wadeite is determined from much more precise calorimetric measurements, we doubt the existence of the narrow stability field for kalsilite + coesite. In addition, seven MA experiments ranging from 6.0 GPa to 7.7 GPa were undertaken to examine this stability field (Table 3.6, Fig. 3.4). The starting material in the seven MA experiments contains kalsilite and coesite, and the low pressure and the high pressure phases are also included

in the starting material for reversal purposes. None of the run products of these experiments contains the assemblage kalsilite + coesite, suggesting no stability field for this assemblage in the pressure range 6.0 - 7.7 GPa at 1400 K. The run products of the two experiments at 6.9 GPa (M 314 and M 315), indicate that at temperature of 1400 K, the phase boundary of reaction (4) is exactly located at 6.9 GPa, which is 0.2 GPa higher than our calculated phase boundary of reaction (4) at 1400 K. Considering the 0.3 GPa uncertainties in these MA experiments and the errors in thermodynamic data, this small discrepancy is acceptable.

Besides Si-wadeite, $K_2Si_4O_9$ has two low-pressure polymorphs, which display an inversion similar to that of α-β quartz at 865 K and atmospheric pressure (Kracek et al. 1929; Goranson and Kracek 1932). A crystallographic study of the low-temperature phase shows that it has a unique sheet-type structure (Schweinsberg and Liebau 1974). For the purpose of simple notation, instead of distinguishing between the two low-pressure polymorphs, a single name of sheet-type $K_2Si_4O_9$ is used to represent both of the phases. It was suggested that sheet-type $K_2Si_4O_9$ has a very limited stability field, decomposing into $K_2Si_2O_5$ + quartz above 0.125 GPa (Fig. 3.5A), and it melts at 1038 K at atmospheric pressure (Goranson and Kracek 1932). The calculated phase boundary (Fig. 3.5A) is only an approximation, because the thermodynamic properties of sheet-type $K_2Si_4O_9$ and $K_2Si_2O_5$ needed for an accurate calculation were not available. The enthalpy and entropy for sheet-type $K_2Si_4O_9$ are still not available, although some indirect estimates were obtained from optimization of the K_2O-SiO_2 system (Wu et al.

1993; Forsberg 2002). Due to the absence of thermal expansion and bulk modulus data for sheet-type $K_2Si_4O_9$ and $K_2Si_2O_5$, only a first-order approximation was undertaken to calculate the phase boundaries in the system $K_2Si_4O_9$ (Figs. 3.5B, 3.5C). The thermodynamic data for quartz are from Holland and Powell (1998) and the thermodynamic data for Si-wadeite are given in Table 3.5. The resultant phase diagrams vary widely due to the different estimates of thermodynamic data for sheet-type $K_2Si_4O_9$ and $K_2Si_2O_5$ (Fig. 3.5B uses the estimation of Wu et al. 1993 and Fig. 3.5C uses the estimation of Forsberg 2002). Both of the calculated phase boundaries of sheet-type $K_2Si_4O_9$ decomposition reaction in Fig. 3.5B and Fig. 3.5C strongly disagree with that of Goranson and Kracek (1932) in Fig. 3.5A. These large discrepancies suggest that further experimental and calorimetric studies are needed to better constrain the phase relations for $K_2Si_4O_9$ polymorphs at low pressures. Experimental determination of the sheet-type $K_2Si_4O_9$ decomposition reaction may be very difficult due to a slow reaction rate below 1000 K. Calorimetric studies seem to be more promising in this case.

Liu (1987) reported that leucite ($KAlSi_2O_6$) composition breaks down into kalsilite + kyanite + Si-wadeite at 1273 K in the pressure range of 6–12 GPa through the reaction:

3 leucite = kalsilite + kyanite + Si-wadeite (6)

This three-phase assemblage was also found in the system $CaMgSi_2O_6$-$KAlSi_2O_6$ at 7 GPa probably due to reaction (6) (Safonov et al. 2003). It is well known that at lower pressures (below 3 GPa), leucite turns to decompose into kalsilite + sanidine (Liu 1987;

Fasshauer et al. 1998) by the reaction:

2 leucite = kalsilite +sanidine (7)

Therefore, reaction (6) is probably due to a combination effect. Indeed Fasshauer et al. (1998) and Yong et al. (2006) suggested the possibility of another reaction,

kalsilite + 2 sanidine = 2 kyanite + 2 wadeite (8)

which is located 0.2 GPa lower than reaction (4) (Yong et al. 2006). Reaction (6) can be obtained from combination of reactions (7) and (8). Here it is concluded that reaction (7) and (8) are stable, and (6) is metastable.

Despite its occasional appearance in experimental studies, Si-wadeite has not been found in nature, probably due to the extremely high pressures required for its formation. The pressure range where Si-wadeite has been reported experimentally is 5–16 GPa (Kinomura et al. 1975; Liu 1987; Urakawa et al. 1994; Yagi et al. 1994; Inoue et al. 1998; Tronnes 2002; Safonov et al. 2003, 2005), suggesting it might occur in metapelites and metagranitoids that are subducted into the earth's upper mantle at depths in excess of 170-200 km. However, almost all of the ultra-high pressure (UHP) rocks of continental origin that are recovered on the earth's surface do not show convincing evidence of exceeding 5 GPa (Withers et al. 2003; Liou et al. 2004). It seems unlikely that Si-wadeite would be found in those associations.

Peak metamorphic conditions were estimated as in the range of ca. 6-7 GPa (Ogasawara et al. 2000) and 6-9 GPa (Ogasawara et al. 2002) in UHP marbles from Kokchetav massif, northern Kazakhstan. However, Si-wadeite has not been observed in

those rocks, whereas K-feldspar was identified as part of the UHP assemblage, suggesting that the pressure was not high enough for K-feldspar to dissociate and form Si-wadeite (~6.4 GPa at 1273 K, Fig. 3.2). The presence of abundant K-feldspar also suggests that the fluid composition was not H_2O-rich, because K-cymrite would have formed instead of sanidine (Yong et al. 2006). Ogasawara et al. (2000) concluded that temperature at the peak pressure was 1253-1523 K, although few data constrain those temperatures. Ogasawara et al. (2002) described titanite with exsolved coesite in Kokchetav marbles, which they inferred exsolved from 5.5-14.5% $CaSi_2O_5$ solid solution in the titanite. Decomposition of supersilicic titanite to coesite requires formation of an additional Ca phase as they noted, but very little calcite was found in the titanite. Supersilicic titanite may have reacted with CO_2 to form titanite + coesite + aragonite, where most of the carbonate formed externally (and now is inverted to calcite). If so, reintegrations of titanite with exsolved coesite are suspect as sufficient Ca was not included. Ogasawara et al. (2002) concluded from the phase equilibria of Knoche et al. (1998) at 1623 K that the rocks attained at least 6 GPa, but conceded that the effect of T on the equilibria was unknown. The effect of 7-8% $CaAlSiO_4F$ solid solution in the titanite was also neglected in their analysis. The fluid composition was inferred to be CO_2-poor and H_2O-rich in these diamond-bearing marbles by Ogasawara et al. (2002), who did not address the potential dilution by CH_4. Sanidine may well be stable with supersilicic titanite at 1173-1273 K and ca. 5 GPa in the absence of fluid, but the lack of K-cymrite remains difficult to explain in the presence of H_2O-rich fluid. Previously

formed K-cymrite or Si-wadeite may have totally back-reacted during decompression. Careful study of inclusions in zircon if present in the Kokchetav marble may be of interest in further addressing the nature of the potassium assemblages at or near peak P-T. Additional consideration of the fluid composition and its evolution in the Kokchetav marbles during metamorphism may also prove fruitful.

ACKNOWLEDGMENTS

The authors are grateful to C.E. Manning of UCLA for providing sanidine glass that was used in this study. They also thank C.E. Henderson for help in EMP analysis and R.C. Rouse with XRD measurements. The authors acknowledge C. Ballhaus, S. Klemme and another reviewer for their constructive reviews of the manuscript. They also thank Y. Zhang, R.C. Ewing and L.P. Stixrude for ongoing commentary on this research. M. Hirschmann generously has continued to provide access to his high-pressure facility at the University of Minnesota for the PhD research of the senior author. This work was supported by Scott Turner Research Grant by the Department of Geological Sciences, University of Michigan to the senior author, NSF grants EAR 96-28196, 99-11352, 00-87448 and 05-37068 to E.J. Essene, NSF grant EAR 04-56405 to M. Hirschmann, and grant P15880-N11 of the Austrian Science Fund to E. Dachs at the University of Salzburg.

Table 3.1 Reported entropy and enthalpy data for Si-wadeite

Reference	S°_{298} (J mol^{-1}K^{-1})	$H^{\circ}_{f,298}$ (kJ mol^{-1})
Geisinger et al. (1987)	198.9(4.0)	–
Fasshauer et al. (1998)	232(10)	–4301.2(5.7)
Xu et al. (2005)	–	–4288.7(5.1)
Yong et al. (2006)	251(8)	–
This study	253.8(0.6)	–

The numbers in parentheses are 2 standard deviations.

Table 3.2 Average compositions of the phases in this study

Phase	Si-wadeite	kyanite	kalsilite	sanidine
SiO_2 (wt%)	71.42(0.55)	37.19(0.21)	37.51(0.34)	64.15(0.29)
K2O	28.70(0.23)	–	29.46(0.34)	16.85(0.16)
Al2O3	–	62.40(0.43)	32.71(0.39)	18.80(0.23)
Total	100.12	99.59	99.68	99.80
Number of analyses	12	8	13	13
Cations per given O				
O	9	5	4	8
Si	3.989	1.007	0.992	2.979
K	2.045	–	0.989	0.998
Al	–	1.990	1.017	1.029
Total	6.034	2.997	2.998	5.006

Table 3.3 Measured heat capacity of Si-wadeite

T (K)	Cp ($Jmol^{-1}K^{-1}$)	T (K)	Cp ($Jmol^{-1}K^{-1}$)	T (K)	Cp ($Jmol^{-1}K^{-1}$)	T (K)	Cp ($Jmol^{-1}K^{-1}$)
5.12	0.056(1)	40.60	28.10(18)	5.12	0.054(1)	156.58	155.13(54)
5.13	0.051(1)	40.61	28.13(18)	5.13	0.055(1)	156.66	155.36(50)
5.13	0.054(1)	40.65	28.29(19)	5.13	0.051(1)	156.66	155.20(46)
5.49	0.070(1)	43.52	32.04(21)	10.19	0.577(3)	161.68	159.75(54)
5.49	0.069(1)	43.52	32.03(20)	10.20	0.584(3)	161.75	159.66(50)
5.50	0.069(1)	43.57	32.17(22)	10.20	0.586(4)	161.77	159.77(59)
5.88	0.084(1)	46.63	36.33(23)	15.20	2.035(11)	166.73	163.88(51)
5.89	0.084(1)	46.64	36.35(23)	15.21	2.059(9)	166.81	163.90(47)
5.89	0.087(1)	46.69	36.48(24)	15.22	2.062(9)	166.81	163.80(49)
6.30	0.113(1)	49.98	40.86(26)	20.26	4.864(25)	171.73	168.67(55)
6.31	0.110(1)	49.98	40.85(27)	20.28	4.888(25)	171.81	168.03(47)
6.31	0.110(1)	50.04	40.98(27)	20.29	4.924(24)	171.82	168.41(63)
6.77	0.149(1)	53.56	45.54(28)	25.35	9.315(55)	176.84	172.97(54)
6.77	0.148(1)	53.57	45.56(29)	25.36	9.313(52)	176.92	172.65(49)
6.78	0.146(1)	53.63	45.70(29)	25.36	9.242(54)	176.92	172.97(49)
7.21	0.182(2)	57.41	50.68(32)	30.40	14.776(87)	181.84	176.71(52)
7.21	0.182(1)	57.42	50.66(31)	30.40	14.796(85)	181.90	176.94(47)
7.22	0.182(1)	57.47	50.86(32)	30.40	14.777(89)	181.91	176.49(65)
7.72	0.228(2)	61.54	56.10(35)	35.43	21.19(14)	186.94	180.41(53)
7.73	0.228(2)	61.54	55.97(32)	35.45	21.25(13)	187.03	180.59(45)
7.73	0.228(2)	61.61	56.00(36)	35.45	21.23(13)	187.03	179.89(47)
8.28	0.288(2)	65.96	61.72(34)	40.50	28.01(19)	191.94	184.07(54)
8.28	0.286(2)	65.97	61.77(37)	40.50	28.03(18)	192.02	183.98(54)
8.29	0.288(2)	66.04	61.99(39)	40.50	28.00(18)	192.02	183.70(52)
8.87	0.367(3)	70.70	67.68(36)	45.46	34.43(23)	197.06	187.93(55)
8.87	0.366(3)	70.72	67.66(37)	45.55	34.87(22)	197.14	187.91(51)
8.88	0.367(2)	70.73	69.84(45)	45.55	34.87(22)	197.14	187.50(50)
9.50	0.463(4)	75.72	73.80(37)	50.51	41.21(21)	202.04	191.72(77)
9.51	0.462(3)	75.73	74.14(41)	50.60	41.66(26)	202.13	191.68(54)
9.51	0.463(3)	75.81	74.06(42)	50.60	41.66(26)	202.14	191.62(48)
10.18	0.584(4)	81.16	80.52(42)	55.57	47.99(26)	207.16	194.95(51)
10.19	0.580(4)	81.16	80.92(41)	55.66	48.34(30)	207.24	195.06(49)
10.19	0.583(4)	81.24	80.98(46)	55.66	48.38(30)	207.25	194.93(52)
10.92	0.729(5)	86.97	87.20(41)	60.63	54.53(28)	212.14	198.25(74)
10.92	0.729(4)	86.97	87.72(43)	60.72	55.01(35)	212.22	198.42(53)
10.93	0.729(4)	87.06	87.66(47)	60.72	55.02(34)	212.23	198.75(50)
11.70	0.915(7)	93.21	93.81(42)	65.69	61.07(31)	217.26	202.28(81)
11.70	0.909(6)	93.21	93.65(43)	65.78	61.57(37)	217.35	202.66(51)
11.71	0.912(5)	93.30	93.74(44)	65.78	61.58(36)	217.36	202.61(53)
12.53	1.141(8)	99.91	101.09(39)	70.75	67.09(33)	222.31	205.61(76)
12.54	1.135(6)	99.92	101.38(40)	70.83	67.74(35)	222.40	204.75(48)
12.54	1.136(6)	100.01	101.60(45)	70.84	67.85(39)	222.41	206.25(50)
13.43	1.425(10)	107.09	108.67(43)	75.80	73.23(34)	227.35	208.11(77)
13.43	1.420(8)	107.09	108.61(40)	75.88	74.00(38)	227.45	208.71(53)
13.44	1.425(7)	107.19	109.15(47)	75.89	74.23(41)	227.46	208.68(51)
14.39	1.758(10)	114.79	117.14(46)	80.85	80.26(39)	232.40	211.22(78)
14.40	1.765(12)	114.79	117.10(46)	80.93	80.10(40)	232.49	211.77(55)
14.40	1.757(9)	114.88	117.56(47)	80.93	80.14(43)	232.51	212.09(73)
15.42	2.173(11)	123.03	125.54(42)	85.89	85.68(48)	237.38	215.79(73)
15.43	2.183(15)	123.04	125.13(44)	85.98	86.34(45)	237.47	216.01(52)

15.43	2.178(11)	123.13	125.59(49)	85.98	86.48(49)	237.48	215.95(55)
16.53	2.692(14)	131.88	133.63(43)	90.93	90.27(48)	242.52	219.89(70)
16.53	2.692(14)	131.88	133.23(40)	91.01	91.38(40)	242.60	220.31(55)
16.54	2.707(18)	131.97	133.77(46)	91.02	91.23(44)	242.61	220.43(55)
17.72	3.316(18)	141.36	142.98(46)	95.99	96.07(49)	247.48	223.73(69)
17.72	3.313(18)	141.37	142.85(46)	96.07	96.77(44)	247.56	223.59(53)
17.73	3.326(22)	141.46	144.13(52)	96.07	96.91(47)	247.57	223.78(52)
18.98	4.066(21)	151.52	152.16(45)	101.04	102.09(49)	252.59	226.28(81)
18.98	4.054(21)	151.52	152.15(44)	101.12	102.29(45)	252.68	226.77(56)
19.00	4.082(25)	151.62	151.99(52)	101.13	102.25(52)	252.70	227.16(77)
20.34	4.983(26)	162.43	161.57(42)	106.09	107.49(51)	257.64	228.55(73)
20.34	4.981(31)	162.43	161.47(44)	106.17	107.95(44)	257.72	228.61(56)
20.37	5.024(29)	162.51	161.83(50)	106.18	107.46(42)	257.74	228.85(81)
21.80	6.046(34)	174.13	172.85(48)	111.15	112.39(49)	262.61	232.19(72)
21.80	6.063(33)	174.14	172.75(47)	111.23	112.92(46)	262.69	231.80(58)
21.83	6.090(36)	174.21	172.90(55)	111.23	112.86(47)	262.69	231.68(58)
23.35	7.347(44)	186.63	181.96(45)	116.20	118.50(50)	267.72	234.90(79)
23.35	7.351(41)	186.63	181.83(48)	116.28	118.70(41)	267.81	235.26(58)
23.39	7.399(43)	186.70	182.29(50)	116.29	118.74(48)	267.83	235.71(84)
25.03	8.974(50)	200.02	192.31(48)	121.22	123.01(51)	272.76	237.36(79)
25.03	8.981(52)	200.02	191.98(46)	121.30	123.84(47)	272.85	237.78(56)
25.06	9.038(56)	200.08	192.65(57)	121.30	123.72(48)	272.87	238.25(83)
26.82	10.805(62)	214.36	202.76(51)	126.27	127.81(54)	277.72	240.12(76)
26.82	10.821(70)	214.36	202.56(50)	126.35	128.09(47)	277.80	240.24(59)
26.85	10.767(77)	214.39	202.85(55)	126.35	127.95(45)	277.82	240.93(87)
28.73	12.873(76)	229.74	211.91(56)	131.36	132.25(51)	282.84	242.70(82)
28.73	12.846(79)	229.75	211.66(47)	131.44	132.52(46)	282.93	243.27(60)
28.78	12.951(89)	229.75	211.46(50)	131.45	132.91(55)	282.96	243.66(89)
30.79	15.207(95)	246.20	223.80(58)	136.42	137.26(57)	287.90	245.35(78)
30.79	15.203(96)	246.25	223.87(53)	136.50	137.47(45)	287.98	245.47(60)
30.83	15.30(10)	246.25	223.76(51)	136.50	137.21(45)	287.99	245.54(60)
32.99	17.93(11)	263.79	233.18(74)	141.44	141.98(50)	292.86	249.15(71)
32.99	17.96(11)	263.89	233.24(53)	141.51	142.10(46)	292.93	249.21(69)
33.04	18.04(12)	263.90	232.82(56)	141.52	141.98(54)	292.93	249.13(66)
35.36	20.98(14)	282.64	243.79(73)	146.53	146.41(46)	297.98	251.62(76)
35.36	20.99(13)	282.81	243.81(61)	146.60	147.60(45)	298.06	251.91(61)
35.40	21.14(15)	282.82	243.55(62)	146.61	147.38(44)	298.08	251.97(91)
37.89	24.43(16)	302.79	256.88(72)	151.58	151.08(52)	303.02	254.56(70)
37.89	24.40(16)	302.99	256.13(79)	151.65	151.07(44)	303.10	254.53(59)
37.94	24.56(16)	303.04	255.55(88)	151.66	151.40(56)	303.12	255.22(85)

Table 3.4 Coefficients of the C_p polynomial $C_p = k_0 + k_1T^{-0.5} + k_2T^{-2} + k_3T^{-3} + k_4T + k_5T^2 + k_6T^3$ derived by fitting the PPMS C_p data of wadeite given in Table 3.3. At the bottom of the table, heat capacity at 298.15 K and standard entropy S°_{298} are additionally given (numbers in parenthesis is one standard deviation and apply to the last digits). Different parts of the general C_p polynomial are relevant in different temperature intervals, defined by temperatures T_1 up to T_{ref}. At these temperatures, adjacent fits yield identical C_p. The final S°_{298}, derived by stepwise analytical integration, is not dependent on how the data set has been split.

Formula weight	334.535 g/mol
Sample weight	21.38 mg
k_6	4.0870E-04
T_1	4.83
k_0	4.0297E+00
k_1	-5.8806E+00
k_2	-5.6272E+00
k_3	3.3976E+01
k_4	-3.9081E-01
k_5	2.1525E-02
k_6	1.5306E-04
T_2	26.59
k_0	-3.7695E+02
k_1	1.7839E+03
k_2	-8.4735E+04
k_3	8.8530E+05
k_4	4.8894E+00
k_5	-2.3597E-02
k_6	5.4414E-05
T_3	140.01
k_0	6.3533E+02
k_1	-7.1269E+03
k_2	2.9642E+06
k_3	-1.1829E+08
T_{ref}	298.15
C_p at 298.15	251.1(7)
S°_{298}	253.8(3)

Table 3.5 Phase property data used for phase boundary calculation. The numbers in parentheses are 2 standard deviations.

Phase*	$H^\circ_{f,298}$	S°_{298}	$C_p=c_1+c_2T^{-0.5}+c_3T^{-2}+c_4T^{-3}$ (J mol^{-1}K^{-1})			
	(kJmol^{-1})	(Jmol^{-1}K^{-1})	$c_1 \times 10^{-2}$	$c_2 \times 10^{-3}$	$c_3 \times 10^{-6}$	$c_4 \times 10^{-8}$
$KAlSi_3O_8$ (hol)	−3801.0[a]	166.2(0.4)[c]	3.896	-1.823	-12.934	16.307[e]
$K_2Si_4O_9$ (wd)	−4288.7(5.1)[b]	253.8(0.6)[d]	4.991	-4.350	0	0[f]

Phase*	V°_{298}	$\alpha=a_0+a_1T$ (K^{-1})		K_{0T}	K'_{0T}
	(cm^3 mol^{-1})	$a_0 \times 10^5$	$a_1 \times 10^8$	(GPa)	
$KAlSi_3O_8$ (hol)	71.28[g]	3.320	1.09[i]	183 – 0.033T[i]	4[l]
$K_2Si_4O_9$ (wd)	108.44[h]	2.950	0[j]	90[k]	4[l]

[a] Akaogi et al. (2004);
[b] Xu et al. (2005);
[c] Yong et al. (2006);
[d] This study;
[e] Akaogi et al. (2004);
[f] Fasshauer et al. (1998);
[g] Yamada et al. (1984);
[h] Swanson and Prewitt (1983);
[i] Nishiyama et al. (2005);
[j] Swanson and Prewitt (1986);
[k] Geisinger et al. (1987);
[l] Assumed.

* The thermodynamic data for sanidine, quartz, coesite, kyanite and stishovite are from a modified Holland and Powell (1998) data base, called hp02ver.dat. More detailed information about hp02ver.dat can be found in http://www.perplex.ethz.ch/. The thermodynamic data for $K_2Si_2O_5$ and $K_2Si_4O_9$ (sheet) are from Forsberg (2002) and Wu et al. (1993). See text for details.

Table 3.6 Experimental data on kalsilite + coesite stability.

Run #	*P* (GPa)	*T* (K)	Run time (h)	Starting material	Run products
M 307	6.0	1400	12	San + Ks + Coe	San + slight amount of Coe
M 323	6.5	1400	96	San + Ks + Coe	San + slight amount of Coe
M 308	6.8	1400	12	Ks + Coe + Wd + Ky	San + small amount of Ks
M 314	6.9	1400	24	Ks + Coe + Wd + Ky	San + small amount of Ks
M 315	6.9	1400	96	San + Ks + Coe	Wd + Ky + Coe
M 327	7.0	1400	96	Ks + Coe + Wd + Ky	Wd + Ky + slight amount of Coe
M 322	7.7	1400	96	Ks + Coe + Wd + Ky	Wd + Ky + slight amount of Coe

The slight amount of coesite in the run products of M307, M322, M323, M327 is due to the small excess coesite in the starting materials. The small amount of kalsilite in the run products of M308 and M314 results from the molar ratio of kalsilite vs. coesite in the starting material of 2:3, which is higher than that needed for the reaction Ks + 2Coe = San

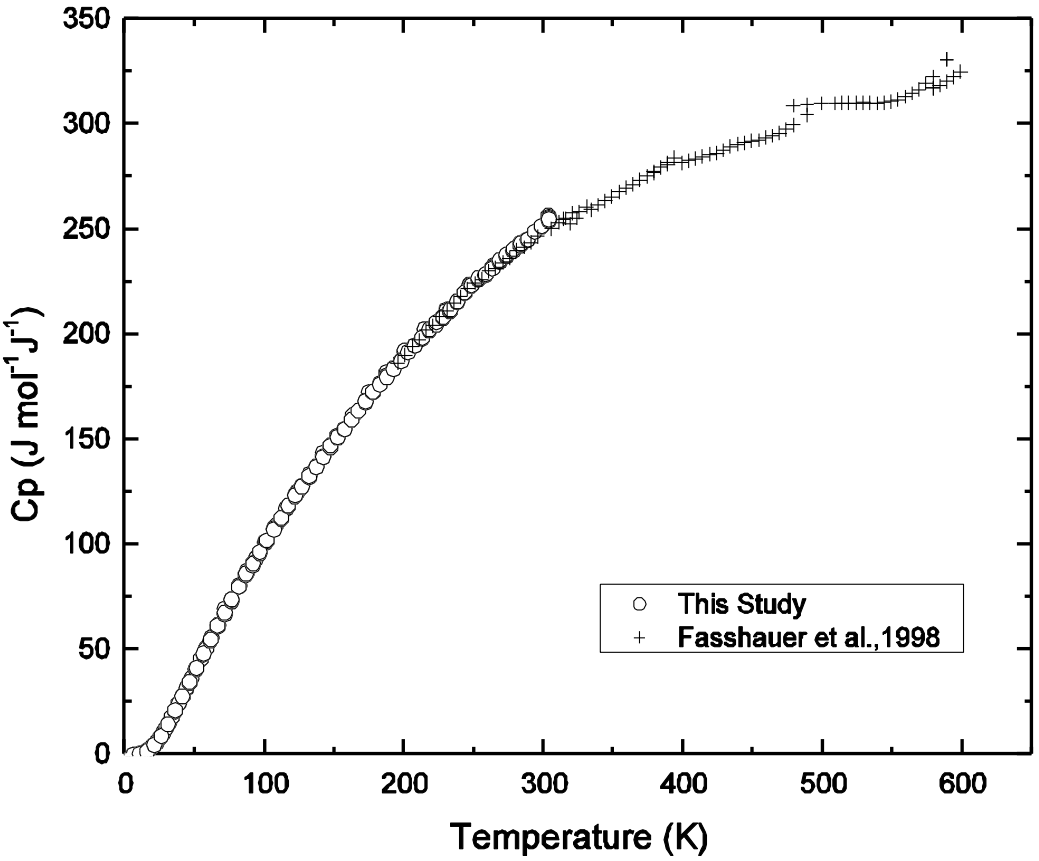

Fig. 3.1 Comparison of the heat capacity data of Si-wadeite measured by PPMS (circles) with those measured by DSC (crosses)

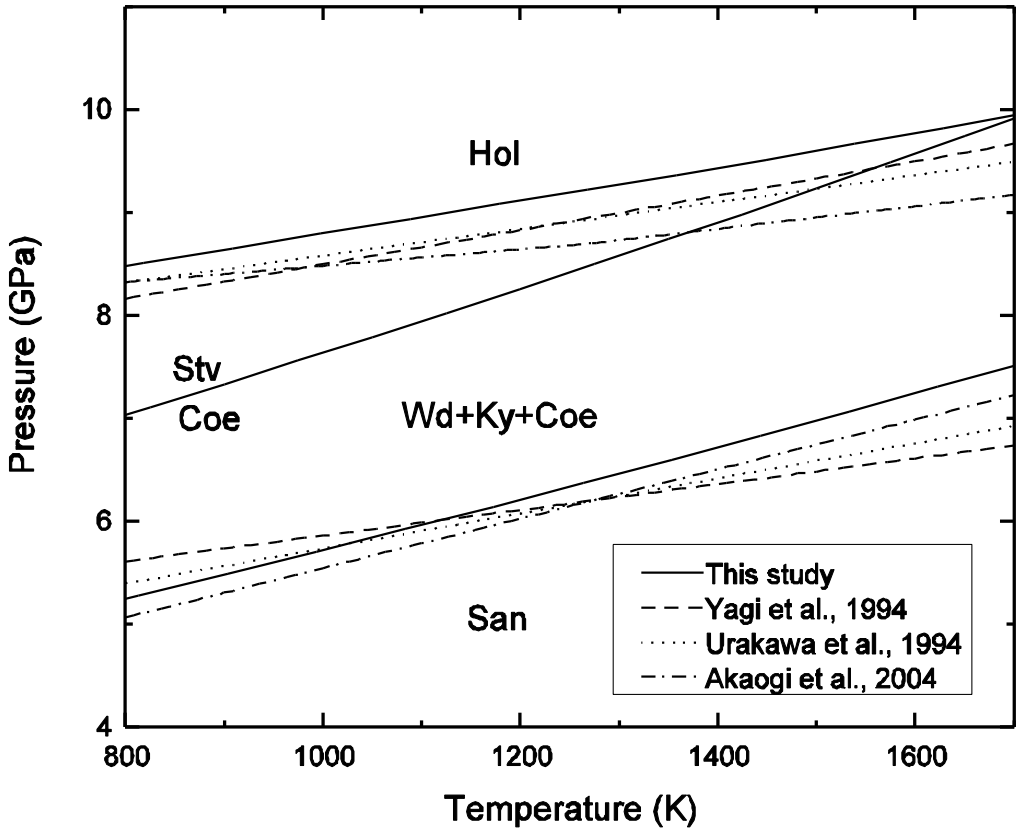

Fig. 3.2 Phase diagrams in the system $KAlSi_3O_8$. Solid lines are our calculated phase boundaries while dashed, dotted, and dash-dotted lines represent those by Yagi et al. (1994), Urakawa et al. (1994) and Akaogi et al. (2004), respectively. *San* sanidine; *Wd* Si-wadeite; *Coe* coesite; *Stv* stishovite; *hol* $KAlSi_3O_8$ hollandite

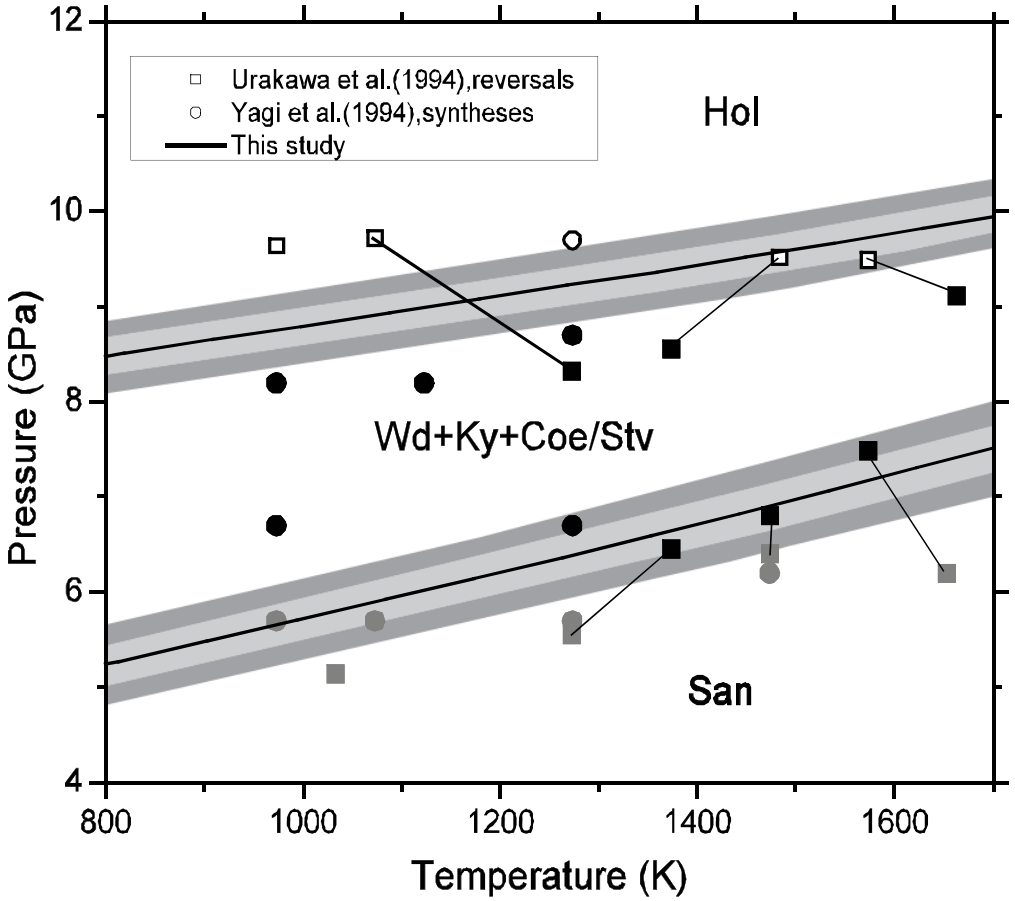

Fig. 3.3 Comparison of calculated phase boundaries with experimental data points of Urakawa et al. (1994) and Yagi et al. (1994). The light- and dark-shaded regions show the uncertainties of the phase boundaries due to one standard deviation and two standard deviations of the enthalpy data, respectively. Open, closed and shaded symbols represent hollandite, Si-wadeite+kyanite+coesite/stishovite, and sanidine, respectively

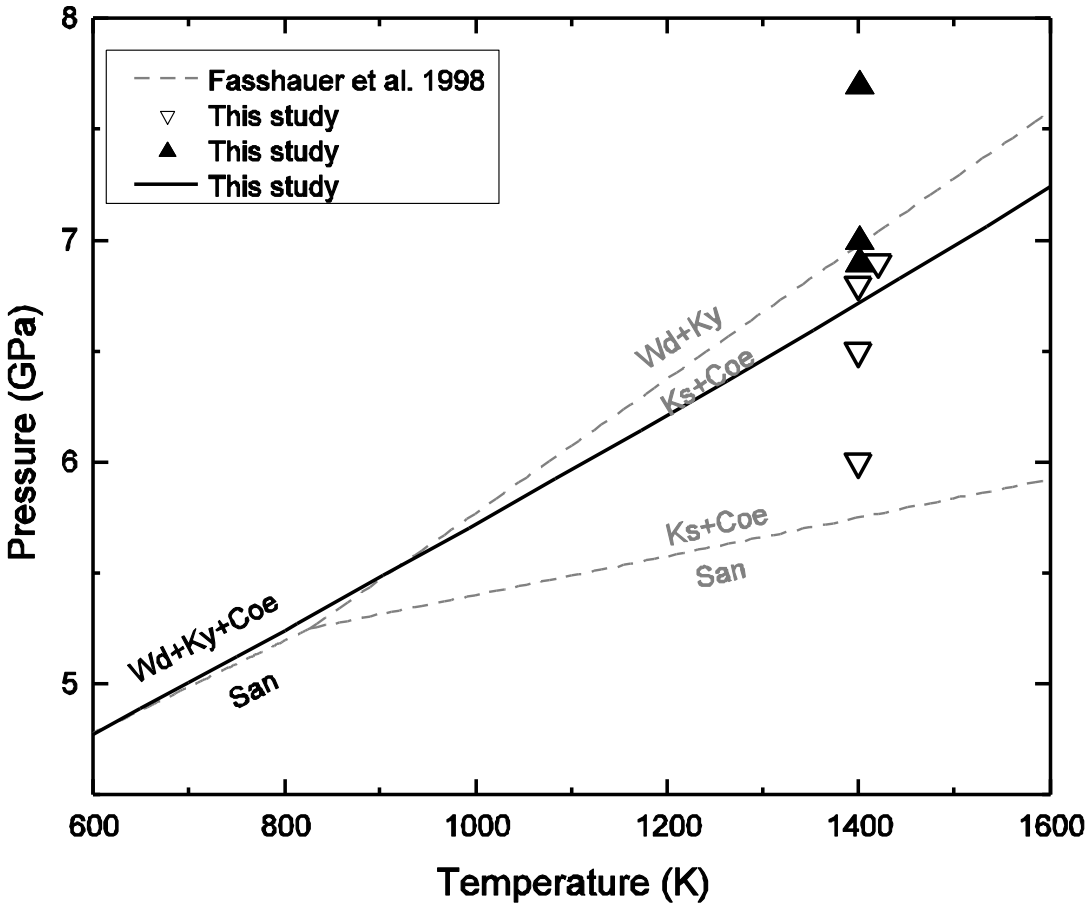

Fig. 3.4 Stability field of kalsilite + coesite proposed by Fasshauer et al. (1998) (grey dashed lines). The solid line is the calculated phase boundary for reaction (4). Triangles are the seven experimental runs in this study. Open triangles indicate sanidine is the stable phase, while solid triangles indicate Si-wadeite + kyanite + coesite is the stable assemblage. The position of the open triangle at 6.9 GPa offset by 20 K to avoid overlap of symbols. *Ks* kalsilite

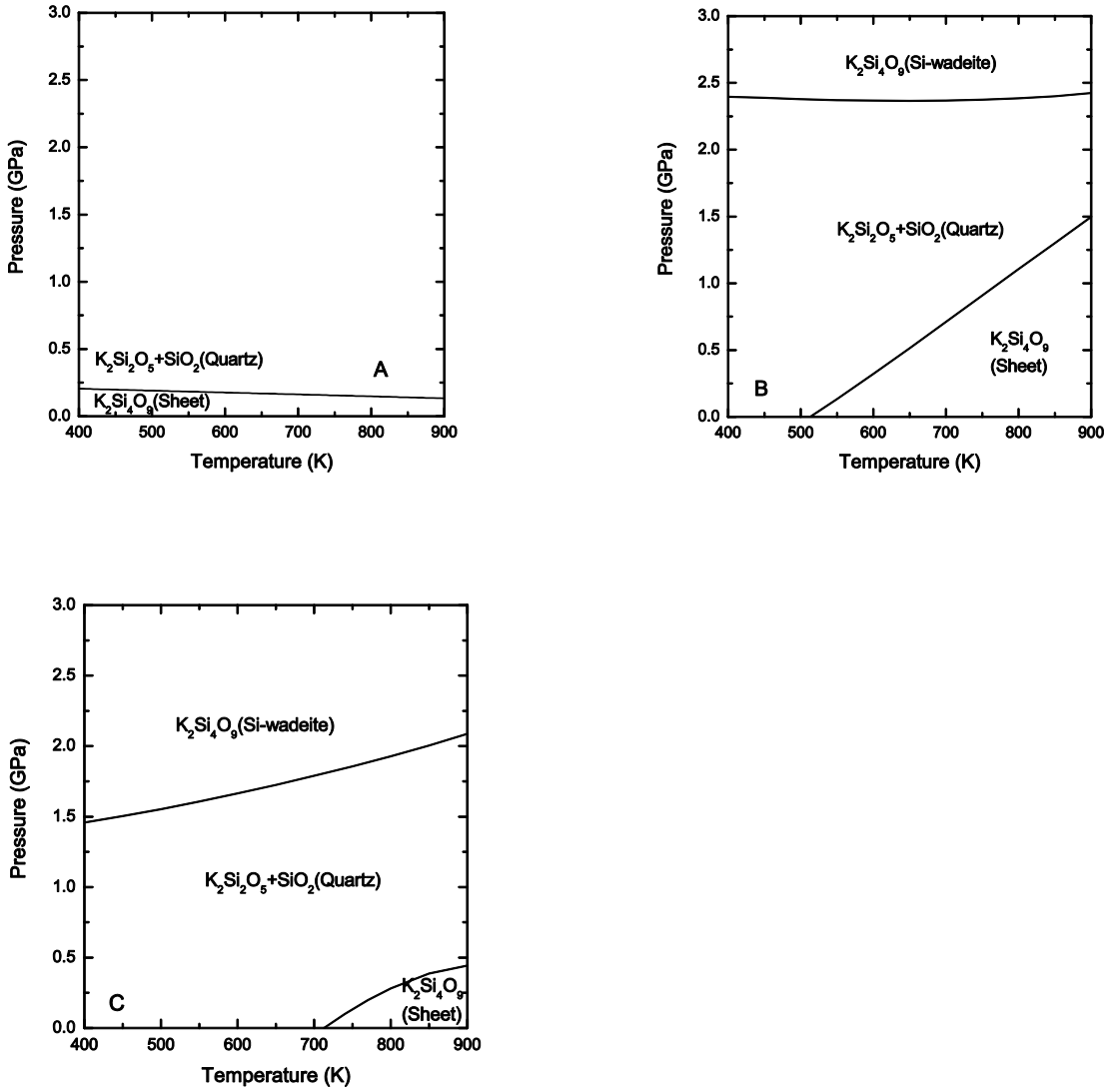

Fig. 3.5 Phase diagrams in the system $K_2Si_4O_9$. Fig. 3.5A is the calculated phase equilibrium diagram by Goranson and Kracek (1932). Fig. 3.5B and Fig. 3.5C were calculated with a first-order approximation neglecting thermal expansion and compressibility terms. Thermodynamic data for $K_2Si_2O_5$ and $K_2Si_4O_9$ (sheet) are from Wu et al. (1993) (Fig. 3.5B) and Forsberg (2002) (Fig. 3.5C)

REFERENCES

Akaogi M, Kamii N, Kishi A, Kojitani H (2004) Calorimetric study on high–pressure transitions in $KAlSi_3O_8$. Phys Chem Minerals 31:85–91

Bose K, Ganguly J (1995) Quartz-coesite transition revisited: reversed experimental determination at 500-1200 °C and retrieved thermochemical properties. Am Mineral 80:231–238

Carlson WD, Lindsley DH (1988) Thermochemistry of pyroxenes on join $Mg_2Si_2O_6$-$CaMgSi_2O_6$. Am Mineral 73:242–252

Connolly JAD (1990) Multivariable phase diagrams: an algorithm based on generalized thermodynamics. Am J Sci 290:666–718

Connolly JAD, Kerrick DM (1987) An algorithm and computer program for calculating composition phase diagrams. CALPHAD 11:1–55

Dachs E, Bertoldi C (2005) Precision and accuracy of the heat–pulse calorimetric technique: low temperature heat capacities of milligram–sized synthetic mineral samples. Eur J Mineral 17:251–259

Dachs E, Geiger CA (2006) Heat capacities and entropies of mixing of pyrope-grossular ($Mg_3Al_2Si_3O_{12}$-$Ca_3Al_2Si_3O_{12}$) garnet solid solutions: a low-temperature calorimetric and a thermodynamic investigation. Am Mineral 91:894–906

Dasgupta R, Hirschmann MM, Withers AC (2004) Deep global cycling of carbon constrained by the solidus of anhydrous, carbonated eclogite under upper mantle conditions. Earth Planet Sci Lett 227:73–85

Fasshauer DW, Wunder B, Chatterjee ND, Höhne GWH (1998) Heat capacity of wadeite–type $K_2Si_4O_9$ and the pressure–induced stable decomposition of K–feldspar. Contr Mineral Petrol 131:210–218

Forsberg S (2002) Optimization of thermodynamic properties of the K_2O-SiO_2 system at high temperatures. J Phase Equil 23:211–217

Geisinger KL, Ross NL, McMillan P, Navrotsky A (1987) Potassium silicate ($K_2Si_4O_9$): energetics and vibrational spectra of glass, sheet silicate, and wadeite–type phases. Am Mineral 72:984–994

Goranson RW, Kracek FC (1932) An experimental investigation of phase relations of $K_2Si_4O_9$ under pressure. J Phys Chem 36:913–926

Holland TJB (1989) Dependence of entropy on volume for silicate and oxide minerals: a review and a predictive model. Am Mineral 74:5–13

Holland TJB, Powell R (1998) An internally consistent thermodynamic data set for phases of petrological interest. J Metam Geol 16:309–343

Inoue T, Irifune T, Yurimoto H, Miyagi I (1998) Decomposition of K-amphibole at high pressures and implications for subduction zone volcanism. Phys Earth Planet Int 107:221–231

Kinomura N, Koizumi M, Kume S (1977) Crystal structures of phases produced by disproportionation of K–feldspar under pressure. In: Manghnani MH, Akimoto S (eds) High–Pressure Research: Application in Geophysics. Academic Press, New York, pp 183–189

Kinomura N, Kume N, Koizumi M (1975) Stability of $K_2Si_4O_9$ with wadeite type structure. Proc 4th Inter Conf High Pressure Sci Tech, pp 211–214

Knoche R, Angel RJ, Seifert F, Fliervoet TF (1998) Complete substitution of Si for Ti in titanite $Ca(Ti_{1-x}Si_x)^{vi}Si^{iv}O_5$. Am Mineral 83:1168–1175

Kracek FC, Bowen NL, Morey GW (1929) The system potassium metasilicate-silica. J Phys Chem 33:1857–1879

Lashley JC, Hundley MF, Migliori A, Sarrao JL, Pagliuso PG, Darling TW, Jaime M, Cooley JC, Hults WL, Morales L, Thoma DJ, Smith JL, Boerio-Goates J, Woodfield BF, Stewart GR, Fisher RA, Phillips NE (2003) Critical examination of heat capacity measurements made on a Quantum Design physical property measurement system. Cryogenics 43:369–378

Liou JG, Tsujimori T, Zhang RY, Katayama I, Maruyama S (2004) Global UHP metamorphism and continental subduction/collision: the Himalayan model. Int Geol Rev 9:1–27

Liu L (1987) High-pressure phase transitions of potassium aluminosilicates with an emphasis on leucite. Contr Mineral Petrol 95:1–3

Manon MR, Dachs E, Essene EJ (2007) Low temperature measurements of heat capacity and new entropy data for titanite: implications for thermobarometry of high pressure rocks. Contr Mineral Petrol, in revision.

Nishiyama N, Rapp RP, Irifune T, Sanehira T, Yamazaki D, Funakoshi K (2005) Stability and P-V-T equation of state of $KAlSi_3O_8$-hollandite determined by in situ X-ray observations and implications for dynamics of subducted continental crust material. Phys Chem Minerals 32:627–637

Ogasawara Y, Ohta M, Fukasawa K, Katayama I, Maruyama S (2000) Diamond-bearing and diamond-free metacarbonate rocks from Kumdy-Kol in the Kokchetav Massif, northern Kazakhastan. Isl Arc 9:400–416

Ogasawara Y, Fukasawa K, Maruyama S (2002) Coesite exsolution from supersilicic titanite in UHP marble from Kokchetav Massif, northern Kazakhstan. Am Mineral 87:454–461

Piermarini GJ, Block S (1975) Ultrahigh pressure diamond-anvil cell and several semiconductor phase transition pressures in relation to fixed point pressure scale. Rev Sci Instrum 46:973–979

Ringwood AE, Reid AF, Wadsley AD (1967) High–pressure $KAlSi_3O_8$, an alumino-silicate with sixfold coordination. Acta Cryst 23:1093–1095

Safonov OG, Litvin YA, Perchuk LL, Bindi L, Menchetti S (2003) Phase relations of potassium-bearing clinopyroxene in the system $CaMgSi_2O_6$-$KAlSi_2O_6$ at 7GPa. Contr Mineral Petrol 146:120–133

Safonov OG, Perchuk LL, Litvin YA, Bindi L (2005) Phase relations in the $CaMgSi_2O_6$-$KAlSi_3O_8$ join at 6 and 3.5 GPa as a model for formation of some potassium-bearing deep-seated mineral assemblages. Contr Mineral Petrol 149:316–337

Schweinsberg VH, Liebau F (1974) Die Kristallstruktur des $K_4[Si_8O_{18}]$: ein neuer Silikat-Schichttyp. Acta Cryst B30:2206–2217

Susaki J, Akaogi M, Akimoto S, Shimomura O (1985) Garnet-perovskite transformation in $CaGeO_3$: in situ X-ray measurements using synchrotron radiation, Geophys Res Lett 12:729–732

Swanson DK, Prewitt CT (1983) The crystal structure of $K_2Si^{VI}Si^{IV}{}_3O_9$. Am Mineral 68:581–585

Swanson DK, Prewitt CT (1986) Anharmonic thermal motion in $K_2Si^{VI}Si^{IV}{}_3O_9$. Eos 67:369

Tronnes RG (2002) Stability range and decomposition of potassic richterite and phlogopite end members at 5–15 GPa. Miner Petrol 74:129–148

Urakawa S, Kondo T, Igawa N, Shimomura O, Ohno H (1994) Synchrotron radiation study on the high-pressure and high-temperature phase relations of $KAlSi_3O_8$. Phys Chem Minerals 21:387–391

Withers AC, Essene EJ, Zhang Y (2003) Rutile/TiO_2II phase equilibria. Contr Mineral Petrol 145:199–204

Wu P, Eriksson G, Pelton AD (1993) Optimization of the thermodynamic properties and phase diagrams of the Na_2O-SiO_2 and K_2O-SiO_2 systems. J Am Ceram Soc 76:2059–2064

Xirouchakis D, Hirschmann MM, Simpson JA (2001) The effect of titanium on the silica content and on mineral-liquid partitioning of mantle-equilibrated melts. Geochim Cosmochim Acta 65:2201–2217

Xu H, Navrotsky A, Balmer ML, Su Y (2005) Crystal-chemical and energetic systematics of wadeite-type phases $A_2BSi_3O_9$ (A = K, Cs; B = Si, Ti, Zr). Phys Chem Minerals 32:426–435

Yagi T, Akaogi M, Shimomura O, Suzuki T, Akimoto S (1987) In situ observation of the olivine-spinel phase transition in Fe_2SiO_4 using synchrotron radiation. J Geophys Res 92:6207–6213

Yagi A, Suzuki T, Akaogi M (1994) High pressure transitions in the system $KAlSi_3O_8$ – $NaAlSi_3O_8$. Phys Chem Minerals 21:12–17

Yamada H, Matsui Y, Ito E (1984) Crystal–chemical characterization of $KAlSi_3O_8$ with hollandite structure. Mineral J 12:29–34

Yong W, Dachs E, Withers AC, Essene EJ (2006) Heat capacity and phase equilibria of hollandite polymorph of $KAlSi_3O_8$. Phys Chem Minerals 33:167–177

Yong W, Dachs E, Withers AC, Essene EJ (2007) Low-temperature heat capacity and thermodynamic properties of γ-Fe_2SiO_4. Phys Chem Minerals 34:121–127

Zhang J, Ko J, Hazen RM, Prewitt CT (1993) High–pressure crystal chemistry of $KAlSi_3O_8$ hollandite. Am Mineral 78:493–499

Zhang J, Liebermann RC, Gasparik T, Herzberg CT (1993) Melting and subsolidus relations of SiO_2 at 9-14 GPa. J Geophys Res 98:19,785–19,793

CHAPTER IV

HEAT CAPACITY OF γ-Fe_2SiO_4 BETWEEN 5 AND 303 K AND DERIVED THERMODYNAMIC PROPERTIES

ABSTRACT

A multi-anvil device was used to synthesize 24 mg of pure γ-Fe_2SiO_4 crystals at 8.5 GPa and 1273 K. The low-temperature heat capacity (C_p) of γ-Fe_2SiO_4 was measured between 5 and 303 K using the heat capacity option of a physical properties measurement system (PPMS). The measured heat capacity data show a broad λ-transition at 11.8 K. The difference in the C_p between fayalite and γ-Fe_2SiO_4 is reduced as the temperature increases in the range of 50-300 K. The gap in C_p data between 300 K and 350 K of γ-Fe_2SiO_4 is an impediment to calculation of a precise C_p equation above 298 K that can be used for phase equilibrium calculations at high temperatures and high pressures. The C_p and entropy of γ-Fe_2SiO_4 at standard temperature and pressure ($S°_{298}$) are 131.1 ± 0.6 $Jmol^{-1}K^{-1}$ and 140.2 ± 0.4 $Jmol^{-1}K^{-1}$, respectively. The Gibbs free energy at standard pressure and temperature ($\Delta G°_{f,298}$) is calculated to be 1369.3 ± 2.7 $Jmol^{-1}$ based on the new entropy data. The phase boundary for the fayalite–γ-Fe_2SiO_4 transition at 298 K based on current thermodynamic data is located at 2.4 ± 0.6 GPa with a slope of 25.4 bars/K, consistent with extrapolated results of previous experimental studies.

INTRODUCTION

Calorimetric measurements of the heat capacity (C_p) of many high-pressure phases are incomplete. The entropy value is critical to thermodynamic calculations of the phase equilibrium relations, and the most precise way to obtain the entropy value is by measuring the heat capacity as a function of temperature. However, high pressure phases must be synthesized experimentally in a multi-anvil device, and the minimum amount of sample needed for low-temperature heat capacity measurement by conventional low-temperature adiabatic calorimetry (low-TAC, e.g. Robie and Hemingway 1972), which is 10-30 grams in general, would take hundreds of experimental runs just to make enough sample, hence prohibiting the heat capacity measurement in practice. Recently, the heat capacity option of the Physical Properties Measurement System (PPMS, produced by Quantum Design®), based on heat-pulse calorimetry (HPC), has been shown to give precise low-temperature heat capacity measurements of milligram-sized samples (e.g. Dachs and Bertoldi 2005; Yong et al. 2006).

Fayalite (Fe_2SiO_4) is one end-member of olivine, the most abundant mineral in the earth's upper mantle. Numerous experimental studies on Fe_2SiO_4 have shown that fayalite transforms into a phase with a spinel structure (γ-Fe_2SiO_4) at pressures higher than 4-5 GPa at 700-1300 K (e.g. Akimoto et al. 1965, 1967; Inoue 1975; Sung and Burns 1976; Furnish and Bassett 1983; Yagi et al. 1987). The natural occurrence of γ-Fe_2SiO_4 with Fe/(Fe+Mg) ratios ranging from 0.62 to 0.99 has also been reported in a

shocked chondrite meteorite (Xie et al. 2002; Xie and Sharp 2004). The transition in $(Mg,Fe)_2SiO_4$ is regarded to play an important role in the formation of seismic discontinuities. Therefore, direct measurement of the thermodynamic properties of γ-Fe_2SiO_4 and fayalite is of great importance in terms of understanding geophysical applications at mantle conditions. Although the thermodynamic properties of fayalite have been well characterized, those of γ-Fe_2SiO_4 are still in need of characterization. The enthalpy and high-temperature heat capacity of γ-Fe_2SiO_4 were measured by Akaogi et al. (1989) and Watanabe (1982), respectively. However, for the aforementioned reason, the low-temperature heat capacity and thus entropy value of γ-Fe_2SiO_4 was not determined calorimetrically. In this study, the heat capacity data of γ-Fe_2SiO_4 were measured between 5 and 303 K using the PPMS machine at Salzburg, and the entropy and Gibbs free energy at standard temperature and pressure (STP) were calculated from the measured heat capacity data.

EXPERIMENTAL PROCEDURES

Sample Synthesis and Characterization

Fayalite was synthesized from a stoichiometric mixture of Fe_3O_4 and SiO_2. After mixing in an agate pestle and mortar, the starting material was reacted at 1200 °C for 48 hours in a CO–CO_2 gas stream, adjusted to buffer oxygen fugacity at a value of two log units below fayalite–magnetite–quartz equilibrium. A 3 mm diameter Au capsule was loaded with more than 30 mg of fayalite powder and sealed by welding. The γ-Fe_2SiO_4

used in this study was synthesized from pure fayalite starting material in a 1000-ton Walker-type multi-anvil device at the University of Minnesota. The experimental assemblage consisted of tungsten carbide anvils with 12 mm truncations, a cast MgO–Al_2O_3–SiO_2–Cr_2O_3 octahedron, straight-walled graphite heater and internal MgO spacers. The temperature was controlled using a $W_3Re_{97}/W_{25}Re_{75}$ thermocouple, which was located on top of the Au capsule with a 0.35 mm disk of MgO extrusion for electrical isolation. The sample was pressurized to 8.5 GPa before heating at 1273 K for 12 hours. The experiment was quenched by turning off the power to the heater and then slowly depressurized to ambient pressure. The run product was examined by powder X-ray diffraction and electron microprobe (EMP) analysis, and single phase γ-Fe_2SiO_4 was confirmed.

Heat Capacity Measurement

The molar heat capacity at constant pressure (C_p) of γ-Fe_2SiO_4 in the temperature range of 5–303 K was measured at 1 atm using the heat capacity option of the PPMS at Salzburg University in Austria. A powdered sample of γ-Fe_2SiO_4 (24.0 mg) was sealed into a small Al pan with a lid and placed on a 4×4 mm wide sapphire platform that has a thermometer and a heater attached to the lower side. The C_p data were first collected at 60 different temperatures from 5 K to 303 K with a logarithmic spacing, and three measurements were performed at each temperature. More C_p data were collected around 12 K and from 50 K to 303 K with a linear spacing in a second run. A brief summary of

this technique is given by Yong et al. (2006), and a more detailed description including discussions of the precision and accuracy of the C_p measurement by PPMS is in Lashley et al. (2003) and Dachs and Bertoldi (2005).

RESULTS AND DISCUSSION

The measured molar heat capacity (C_p) data of γ-Fe_2SiO_4 are listed in Table 4.1 and plotted in Fig. 4.1. A C_p polynomial of the general form $C_p = k_o + k_1T^{-0.5} + k_2T^{-2} + k_3T^{-3} + k_4T + k_5T^2 + k_6T^3$ was used to fit the measured molar C_p data, which were split into several temperature regions due to the λ-anomaly. The C_p data below 5 *K* were estimated from a plot of C_p/T versus T^2 and a linear extrapolation to 0 *K*. The entropy of γ-Fe_2SiO_4 at STP is calculated from analytical and stepwise integration of the smoothed C_p data and was found to be identical within error when calculated by numerical integration. The resulting entropy value is 140.2 ± 0.4 $Jmol^{-1}K^{-1}$ (error is two standard deviations). The uncertainty in the entropy is estimated as described by Dachs and Geiger (2006).

In comparison with the C_p data of fayalite (Fig 4.2. triangles), which has a very sharp λ-transition at 64.9 K as well as a small rounded hump near 16 K (Robie et al. 1982), the C_p data of γ-Fe_2SiO_4 (Fig. 4.2. circles) exhibit a broad maximum (λ-transition) at 11.8 K and a weak shoulder around 7 K, possibly related to a Schottky-anomaly (e.g. Gopal 1966) arising from the Fe^{2+} 3d orbitals. The broad λ-transition is likely due to a paramagnetic-antiferromagnetic transition just as the 65 K transition in fayalite (Santoro

et al. 1966; Ehrenberg and Fuess 1993). The C_p of γ-Fe_2SiO_4 measured by PPMS is generally lower than that of fayalite (Robie et al. 1982) in the temperature range of 50-300 K (Fig 4.2). However, the difference of C_p between the two polymorphs decreases with increasing temperature. As a result, the C_p data of γ-Fe_2SiO_4 and fayalite differ less than 1 $Jmol^{-1}K^{-1}$ at 300 K. If this trend continues to high temperatures, the entropy difference (ΔS) and enthalpy difference (ΔH) for the fayalite–γ-Fe_2SiO_4 transition will approach constant values, which means the only cause that can change the slope of the transition boundary will be a difference in volume. However, this situation is not supported by the C_p data of fayalite and γ-Fe_2SiO_4 measured between 350 K and 700 K by Watanabe (1982), who showed there is a 4–6 $Jmol^{-1}K^{-1}$ difference between the C_p values of these two phases in the range of 350–700 K. Unfortunately, the C_p of γ-Fe_2SiO_4 between 300 K and 350 K has not yet been measured and the PPMS routinely measures the C_p data only in the range 2–303 K. Therefore a reasonable and precise fitting of C_p polynomial above 298 K cannot be undertaken until the discrepancy between the available DSC data and the result of this study is resolved. Until then, an accurate representation of the phase boundary for the fayalite–γ-Fe_2SiO_4 transition at high pressures and temperatures is cumbersome.

The entropy of γ-Fe_2SiO_4 at standard pressure and temperature ($S°_{298}$) calculated from integration of the C_p data in this study may be compared with estimates from previous studies. The available estimates of the $S°_{298}$ of γ-Fe_2SiO_4 range from 134 $Jmol^{-1}K^{-1}$ to 146 $Jmol^{-1}K^{-1}$ (e.g. Fei and Saxena 1986; Fei et al. 1991; Fabrichnaya 1998;

Jacobs et al. 2001; Jacobs and de Jong 2005). The $S°_{298}$ value of γ-Fe_2SiO_4 calculated from the measured C_p data in this study, 140.2 ± 0.4 $Jmol^{-1}K^{-1}$, in the midpoint of the range of estimates, will serve as a strong constraint and substantial improvement for the thermodynamic data base of the Fe_2SiO_4 system. The enthalpy of the fayalite–γ-Fe_2SiO_4 transition at standard pressure and temperature ($\Delta H°_{tr,298}$) is given by Akaogi et al. (1989) as 6.6 ± 2.4 $kJmol^{-1}$. The enthalpy of formation at 298 K ($\Delta H°_{f,298}$) of fayalite from elements is given by Robie and Hemingway (1995) as –1478.2 ± 1.3 $kJmol^{-1}$. By combining these two studies, the $\Delta H°_{f,298}$ of γ-Fe_2SiO_4 is calculated to be –1471.6 ± 2.7 $kJmol^{-1}$, which together with our new entropy value, results in the value of Gibbs free energy at standard pressure and temperature ($\Delta G°_{f,298}$), –1369.3 ± 2.7 kJ mol^{-1}.

The fayalite–γ-Fe_2SiO_4 transition boundary at 298 K can be calculated using the equation defined as follows:

$$\Delta G(P,298) = \Delta H^{\circ}_{tr,298} - 298.15\Delta S^{\circ}_{tr,298} + \int_0^P \Delta V(P',298)dP' = 0 \qquad (1)$$

where $\Delta H^{\circ}_{tr,298}$ and $\Delta S^{\circ}_{tr,298}$ are enthalpy and entropy changes, respectively, for the fayalite–γ-Fe_2SiO_4 transition at standard temperature and pressure, and $\Delta V(P,298)$ is the volume change at pressure P and at 298 K. The pressure dependence of the molar volume was expressed by the Birch-Murnaghan equation of state:

$$P = \frac{3}{2}K_0\left[\left(\frac{V^{\circ}}{V}\right)^{7/3} - \left(\frac{V^{\circ}}{V}\right)^{5/3}\right]\left\{1 - \frac{3}{4}\left(4 - K'_0\right)\left[\left(\frac{V^{\circ}}{V}\right)^{2/3} - 1\right]\right\} \qquad (2)$$

where K_0 and K'_0 are the isothermal bulk modulus and its pressure derivative,

respectively. The fayalite–γ-Fe_2SiO_4 transition at 298 K is calculated to be at 2.4 ± 0.6 GPa based on current thermodynamic data given in Table 4.2. The error of the calculated pressure mainly results from the uncertainties of measured enthalpy change of the transition (Akaogi et al. 1989), with a small contribution from the uncertainties of measured entropies of fayalite and γ-Fe_2SiO_4 by Robie et al. (1982) and this study, respectively.

The slope of the fayalite–γ-Fe_2SiO_4 transition at 298 K is also calculated using the Clausius-Clapeyron equation:

$$\frac{dP}{dT} = \frac{\Delta S(P,298)}{\Delta V(P,298)} \qquad (3)$$

where the entropy values at high pressure are corrected with a second order approximation using thermal expansion data at 298 K (Table 2) in the following way:

$$S(P,298) = S^{\circ}_{298} - \Delta P \alpha V^{\circ}_{298} \qquad (4)$$

Substituting P = 2.4 GPa into equation (2), (3) and (4), the slope of the fayalite–γ-Fe_2SiO_4 transition at 298 K is calculated to be 25.4 bars/K.

Experimental determinations of the fayalite–γ-Fe_2SiO_4 transition are plotted and extrapolated to 298 K for comparison with our calculated phase boundary location at 298 K in Fig. 4.3. Even though most of these experiments were undertaken at high temperatures, between 1000 K and 1500 K, the extrapolated locations of the transition boundaries by Akimoto et al. (1967) and Yagi et al. (1987) at 298 K agree with our calculation within 0.4 GPa, whereas the extrapolated position of the transition by

Akimoto et al. (1977) lies at higher pressure. Moreover, the calculated slope of the fayalite–γ-Fe_2SiO_4 transition, 25.4 bars/K, is in excellent agreement with these experimental studies (Fig. 4.3), where the slope was given by either 25 bars/K (Akimoto et al. 1977, Yagi et al. 1987) or 26 bars/K (Akomoto et al. 1967). Because of the missing C_p data of γ-Fe_2SiO_4 between 300 and 350 K, a precise calculation of the phase boundary above 298 K cannot be completed at present.

ACKNOWLEDGMENTS

The authors are grateful to C. Henderson for his help in EMP analysis, and R.C. Rouse for his help with XRD measurements. We gratefully acknowledge the constructive reviews of K.-D. Grevel and one anonymous reviewer, which improved the quality of the manuscript. This work was supported by Scott Turner Research Grant by the Department of Geological Sciences, University of Michigan to the senior author, NSF grants EAR 96-28196, 99-11352, 00-87448 and 05-37068 to E.J. Essene, NSF grants EAR 03-10142 and 00-79827 to M. Hirschmann at University of Minnesota, and grant P15880-N11 of the Austrian Science Fund to E. Dachs at the University of Salzburg.

Table 4.1 Measured heat capacity data of γ-Fe_2SiO_4

T (K)	C_p ($Jmol^{-1}K^{-1}$)	T (K)	C_p ($Jmol^{-1}K^{-1}$)	T (K)	C_p ($Jmol^{-1}K^{-1}$)	T (K)	C_p ($Jmol^{-1}K^{-1}$)
5.14	1.863(9)	49.98	17.48(13)	12.05	13.181(41)	143.42	72.03(25)
5.14	1.856(9)	50.03	17.53(13)	12.06	13.192(33)	143.43	71.97(23)
5.14	1.852(9)	53.56	18.97(14)	12.06	13.204(32)	148.50	74.54(27)
5.51	2.289(11)	53.56	18.96(14)	12.27	13.072(40)	148.57	74.81(23)
5.51	2.286(11)	53.62	19.04(14)	12.28	13.064(32)	148.57	74.88(21)
5.51	2.303(11)	57.41	20.83(16)	12.29	13.059(31)	153.60	77.38(28)
5.90	2.855(14)	57.41	20.84(16)	12.50	12.897(34)	153.68	77.28(23)
5.90	2.865(14)	57.47	20.87(16)	12.51	12.893(30)	153.69	77.34(31)
5.91	2.885(13)	61.53	22.98(17)	12.51	12.889(29)	158.80	79.71(27)
6.32	3.588(17)	61.53	22.95(16)	12.73	12.700(35)	158.88	79.78(22)
6.32	3.591(16)	61.61	22.93(18)	12.74	12.702(30)	158.88	79.71(23)
6.32	3.621(18)	65.95	25.41(17)	12.74	12.700(29)	163.96	82.21(28)
6.77	4.424(21)	65.97	25.36(17)	12.96	12.500(38)	164.04	82.15(23)
6.77	4.421(21)	66.04	25.54(20)	12.97	12.497(29)	164.05	82.27(30)
6.77	4.458(21)	70.70	28.14(18)	12.97	12.489(29)	169.06	84.59(26)
7.22	5.248(23)	70.71	28.12(19)	13.19	12.288(34)	169.14	84.61(23)
7.22	5.253(24)	70.79	28.28(20)	13.19	12.287(28)	169.14	84.60(23)
7.22	5.284(23)	75.78	31.31(20)	13.19	12.292(28)	174.27	87.38(27)
7.74	6.144(26)	75.78	31.27(18)	13.41	12.090(31)	174.35	87.30(24)
7.74	6.117(26)	75.85	31.24(27)	13.42	12.087(27)	174.36	87.44(30)
7.74	6.112(25)	81.16	35.01(23)	13.42	12.086(26)	179.37	89.43(26)
8.29	7.005(29)	81.16	35.07(19)	13.64	11.905(31)	179.45	89.55(23)
8.29	6.987(27)	81.24	35.12(25)	13.65	11.896(26)	179.45	89.36(22)
8.29	6.992(27)	86.98	38.55(23)	13.65	11.893(25)	184.57	91.87(26)
8.88	7.936(31)	86.98	38.58(21)	13.87	11.716(31)	184.66	91.95(32)
8.88	7.917(28)	87.07	38.58(23)	13.88	11.713(25)	184.66	91.65(24)
8.88	7.927(28)	93.21	42.28(22)	13.88	11.714(25)	189.74	93.76(26)
9.52	8.988(31)	93.22	42.17(22)	14.10	11.564(31)	189.82	93.51(23)
9.52	8.994(31)	93.31	42.41(25)	14.11	11.560(25)	189.82	93.63(22)
9.52	9.014(35)	99.92	46.81(23)	14.11	11.565(24)	194.90	96.38(25)
10.20	10.339(35)	99.92	46.67(21)	14.32	11.436(30)	194.98	96.22(24)
10.20	10.342(35)	100.01	46.70(24)	14.33	11.439(25)	194.99	96.01(22)
10.20	10.356(37)	107.09	50.98(22)	14.33	11.438(24)	200.06	98.49(26)
10.93	12.135(42)	107.09	50.84(22)	14.55	11.314(30)	200.14	98.32(23)
10.94	12.138(39)	107.19	50.98(24)	14.56	11.326(24)	200.15	98.25(22)
10.94	12.143(39)	114.79	56.07(23)	14.56	11.321(22)	205.22	100.45(26)
11.70	13.176(39)	114.79	55.81(24)	14.77	11.234(31)	205.30	100.17(24)
11.71	13.208(35)	114.88	56.21(27)	14.78	11.240(24)	205.30	100.11(25)
11.71	13.211(34)	123.03	60.83(22)	14.79	11.238(23)	210.36	101.73(39)
12.53	12.869(37)	123.03	60.86(24)	15.00	11.151(30)	210.45	101.72(24)
12.55	12.863(30)	123.13	60.94(26)	15.01	11.160(24)	210.47	101.89(34)
12.55	12.870(30)	131.88	65.61(23)	15.01	11.157(23)	215.52	103.82(40)
13.42	12.084(36)	131.88	65.53(22)	15.22	11.040(28)	215.62	103.91(23)
13.44	12.077(26)	131.97	65.78(24)	15.22	11.059(25)	215.62	103.89(37)
13.44	12.077(25)	141.36	70.90(22)	15.23	11.071(27)	220.62	105.60(34)
14.38	11.408(33)	141.36	71.03(24)	50.53	17.65(13)	220.70	105.63(25)
14.40	11.411(24)	141.45	71.81(27)	50.60	17.74(13)	220.71	105.86(24)

14.40	11.411(23)	151.51	76.47(24)	50.60	17.73(13)	225.83	107.59(37)
15.42	11.082(27)	151.51	76.37(23)	55.67	19.85(13)	225.92	107.43(25)
15.43	11.081(21)	151.61	76.34(27)	55.76	19.99(15)	225.93	107.64(23)
15.43	11.086(21)	162.40	81.91(22)	55.76	19.99(15)	230.91	109.16(33)
16.53	11.009(24)	162.41	81.85(22)	60.83	22.43(14)	231.00	109.39(23)
16.53	11.014(21)	162.49	81.75(27)	60.92	22.62(17)	231.01	109.54(34)
16.53	11.018(22)	174.08	87.70(25)	60.93	22.56(17)	236.14	111.70(36)
17.71	11.076(21)	174.08	87.68(23)	66.00	25.28(16)	236.23	111.76(24)
17.71	11.082(20)	174.15	87.83(29)	66.09	25.48(19)	236.24	111.92(25)
17.71	11.077(22)	186.65	94.28(23)	66.09	25.47(18)	241.31	113.72(35)
18.97	11.167(23)	186.65	94.25(23)	71.16	28.26(17)	241.39	114.19(28)
18.98	11.170(29)	186.72	94.25(27)	71.25	28.60(20)	241.40	114.00(27)
18.98	11.170(21)	200.04	100.10(23)	71.25	28.45(20)	246.45	115.75(42)
20.34	11.294(19)	200.04	100.19(22)	76.31	31.21(23)	246.54	116.30(25)
20.34	11.291(21)	200.09	100.20(27)	76.40	31.81(18)	246.55	116.13(24)
20.34	11.297(21)	214.38	105.70(24)	76.40	31.89(21)	251.61	117.74(33)
21.79	11.413(21)	214.38	105.74(26)	81.46	35.16(23)	251.69	118.14(25)
21.79	11.421(22)	214.41	105.57(29)	81.55	35.22(22)	251.70	117.85(23)
21.80	11.414(21)	229.76	110.36(26)	81.56	35.10(23)	256.67	118.97(31)
23.35	11.552(23)	229.76	110.34(23)	86.58	38.29(21)	256.75	119.20(23)
23.35	11.552(23)	229.77	110.23(23)	86.66	38.43(21)	256.77	119.24(36)
23.36	11.542(20)	246.24	116.64(29)	86.67	38.29(21)	261.89	120.81(39)
25.02	11.742(35)	246.27	116.49(23)	91.75	41.30(26)	261.98	121.45(27)
25.02	11.734(26)	246.28	116.48(24)	91.84	41.49(22)	262.07	121.55(33)
25.04	11.732(25)	263.81	121.38(36)	91.85	41.55(25)	267.06	122.98(31)
26.81	11.910(30)	263.92	121.30(26)	96.91	44.59(25)	267.13	122.98(24)
26.81	11.898(27)	263.94	121.04(26)	97.00	44.71(23)	267.15	123.31(41)
26.83	11.959(32)	282.70	126.59(36)	97.00	44.83(25)	272.11	124.38(28)
28.73	12.070(35)	282.85	126.47(29)	102.07	48.10(24)	272.19	124.05(25)
28.73	12.064(35)	282.85	126.58(29)	102.16	47.88(24)	272.21	124.15(40)
28.75	12.086(33)	302.95	132.51(34)	102.16	48.12(25)	277.36	125.07(32)
30.78	12.293(43)	303.14	132.30(25)	107.22	50.93(26)	277.43	125.24(27)
30.78	12.296(50)	303.15	132.52(48)	107.31	51.29(23)	277.44	125.24(26)
30.81	12.311(50)			107.32	51.15(25)	282.51	126.28(30)
32.99	12.642(51)			112.35	54.25(26)	282.57	126.65(27)
32.99	12.644(51)	10.68	11.502(44)	112.43	54.54(24)	282.59	126.69(24)
33.02	12.664(60)	10.69	11.492(39)	112.44	54.41(24)	287.56	128.03(27)
35.35	13.090(62)	10.69	11.491(38)	117.51	57.51(26)	287.62	128.05(26)
35.35	13.089(60)	10.91	12.091(45)	117.59	57.70(22)	287.64	128.34(43)
35.39	13.121(68)	10.92	12.104(39)	117.60	57.84(26)	292.8	129.95(30)
37.89	13.739(75)	10.92	12.102(38)	122.70	60.65(26)	292.88	130.20(30)
37.89	13.728(73)	11.14	12.582(44)	122.78	60.73(22)	292.88	129.94(27)
37.92	13.756(75)	11.14	12.593(39)	122.79	60.86(27)	297.95	131.21(30)
40.60	14.33(85)	11.14	12.589(38)	127.86	63.53(25)	298.02	131.15(25)
40.60	14.326(86)	11.37	12.946(43)	127.94	63.61(21)	298.03	131.38(44)
40.64	14.364(85)	11.37	12.944(37)	127.95	63.86(28)	302.99	132.38(26)
43.51	15.14(10)	11.37	12.959(36)	133.02	66.05(28)	303.06	132.46(28)
43.51	15.14(10)	11.59	13.145(41)	133.10	66.23(22)	303.06	132.60(27)
43.56	15.18(10)	11.60	13.165(36)	133.10	66.22(25)		
46.63	16.20(11)	11.60	13.152(35)	138.14	69.07(28)		
46.63	16.20(11)	11.82	13.228(41)	138.22	69.16(24)		
46.68	16.25(11)	11.83	13.233(35)	138.22	69.02(21)		
49.98	17.45(13)	11.83	13.234(33)	143.34	71.84(28)		

Table 4.2 Thermodynamic properties used for phase boundary calculation

Phase	$H^\circ_{f,298}$	S°_{298}	V°_{298}	K_0	K'_0	$\alpha = a + bT + cT^{-2}$ $(K^{-1})^j$		
	(kJ mol^{-1})	(J $mol^{-1}K^{-1}$)	(cm^3mol^{-1})	(GPa)		a × 10^5	b × 10^9	c × 10
Fayalite	–1478.2±1.3[a]	151±0.2[c]	46.28[e]	134[g]	4[i]	2.66	8.736	-2.487
γ-Fe_2SiO_4	–1471.6±2.7[b]	140.2±0.4[d]	42.04[f]	197[h]	4[i]	2.455	3.591	-3.703

[a] Robie and Hemingway (1995)
[b] Calculated from Akaogi et al. (1989)
[c] Robie et al. (1982)
[d] This study
[e] Akimoto et al. (1976)
[f] Marumo et al. (1977)
[g] Kudoh and Takeda (1986)
[h] Sato (1977)
[i] Assumed
[j] Fei and Saxena (1986)

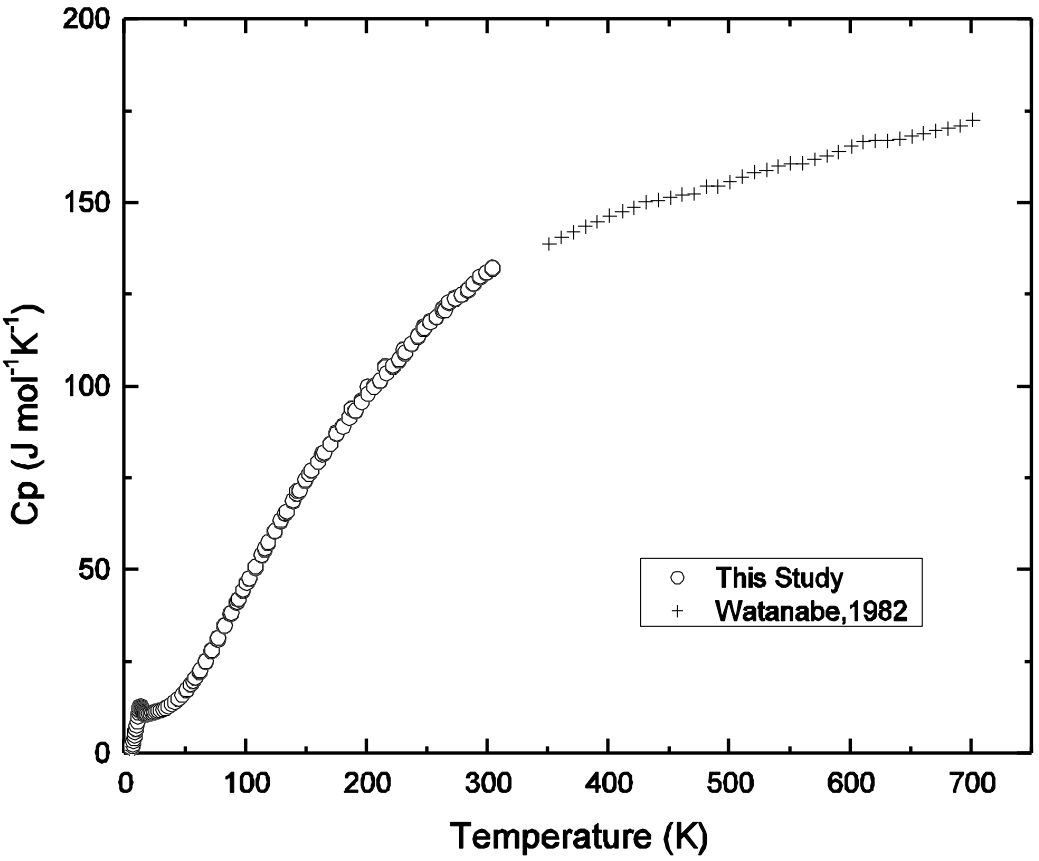

Fig. 4.1 Comparison of the heat capacity data of γ-Fe_2SiO_4 measured by PPMS (circles) with those measured by DSC (crosses).

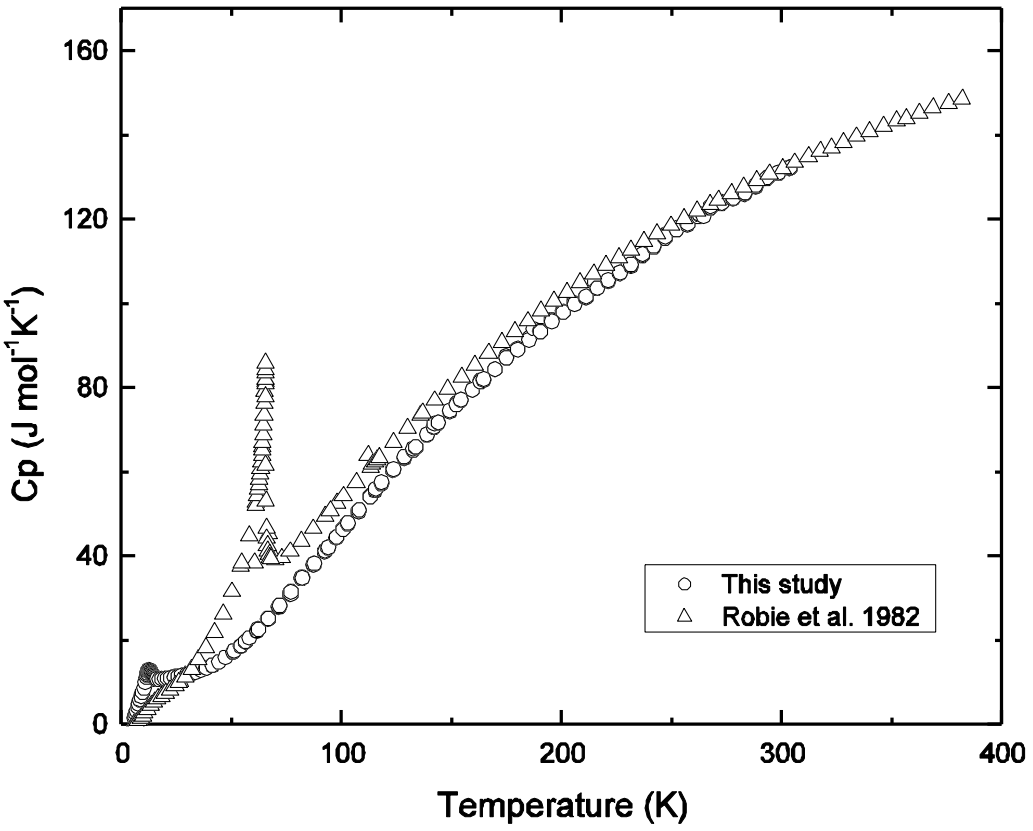

Fig. 4.2 Comparison of heat capacity data of γ-Fe_2SiO_4 (circles) with fayalite (triangles).

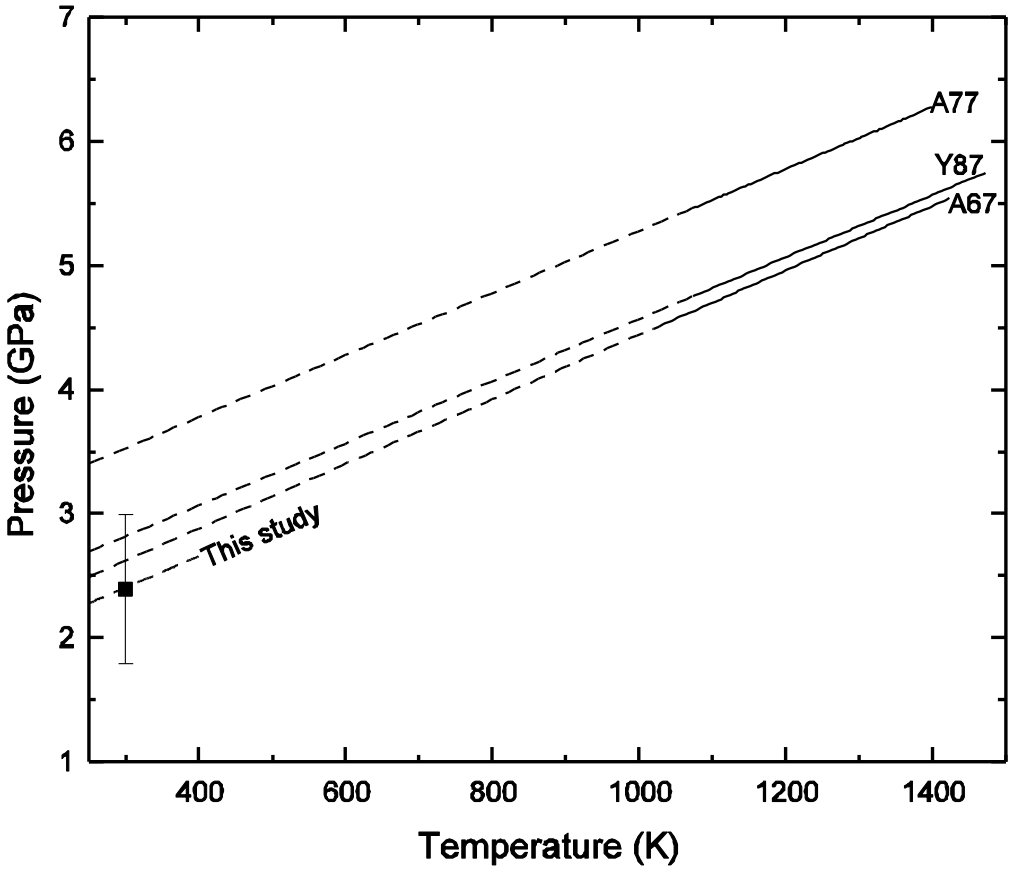

Fig. 4.3 Comparison of the phase transition boundary at 298 K calculated in this study with previous experimental studies. Black square represents our calculated location of phase transition boundary with two standard deviations. The calculated slope at 298 K is also plotted for comparison. A67 Akimoto et al. (1967); A77 Akimoto et al. (1977); Y87 Yagi et al. (1987)

REFERENCES

Akaogi M, Ito E, Navrotsky A (1989) Olivine-modified spinel-spinel transition in the system Mg_2SiO_4-Fe_2SiO_4: calorimetric measurements, thermochemical calculation, and geophysical application. J Geophys Res 94:15671–15685

Akimoto S, Fujisawa H, Katsura T (1965) Olivine-spinel transition in Fe_2SiO_4 and Ni_2SiO_4. J Geophys Res 66:1969–1977

Akimoto S, Komada E, Kushiro I (1967) Effect of pressure on the melting of olivine and spinel polymorphs of Fe_2SiO_4. J Geophys Res 68:679–686

Akimoto S, Matsui Y, Syono Y (1976) High-pressure crystal chemistry of orthosilicates and formation of the mantle transition zone. In: Strens RGJ (eds) The Physics and Chemistry of Minerals and Rocks. John Wiley, New York, pp 327–363

Akimoto S, Yagi T, Inoue K (1977) High temperature-pressure phase boundaries in silicate systems using in situ X-ray diffraction. In: Manghnani MH, Akimoto S (eds) High–Pressure Research: Application in Geophysics. Academic Press, New York, pp 585–602

Dachs E, Bertoldi C (2005) Precision and accuracy of the heat-pulse calorimetric technique: low temperature heat capacities of milligram-sized synthetic mineral samples. Eur J Mineral 17:251–259

Dachs E, Geiger CA (2006) Heat capacities and entropies of mixing of pyrope-grossular ($Mg_3Al_2Si_3O_{12}$-$Ca_3Al_2Si_3O_{12}$) garnet solid solutions: A low-temperature calorimetric and a thermodynamic investigation. Am Mineral 91:8894–9006

Ehrenberg H, Fuess H (1993) Analytical interpretation and simulation of the static magnetic properties of synthetic α-Fe_2SiO_4. J Phys Condens Matter 5:3663–3672

Fabrichnaya O (1998) The assessment of thermodynamic parameters for solid phases in the Fe-Mg-O and Fe-Mg-Si-O systems. Calphad 22:85–125

Fei Y, Mao H, Mysen BO (1991) Experimental determination of element partitioning and calculation of phase relations in the MgO-FeO-SiO_2 system at high pressure and high temperature. J Geophys Res 96:2157–2169

Fei Y, Saxena SK (1986) A thermochemical data base for phase equilibria in the system Fe-Mg-Si-O at high pressure and temperature. Phys Chem Minerals 13:311–324

Furnish MD, Bassett WA (1983) Investigation of the mechanism of the olivine-spinel transition in fayalite by synchrotron radiation. J Geophys Res 88:10333–10341

Gopal ESR (1966) Specific heats at low temperatures. Plenum Press, New York

Inoue K (1975) Development of high temperature and high pressure x-ray diffraction apparatus with energy dispersive technique and its geophysical applications. PhD thesis, Tokyo Univ., Tokyo

Jacobs MHG, de Jong BHWS (2005) An investigation into thermodynamic consistency of data for the olivine, wadsleyite and ringwoodite form of $(Mg,Fe)_2SiO_4$. Geochim Cosmochim Acta 69:4361–4375

Jacobs MHG, de Jong BHWS, Oonk HAJ (2001) The Gibbs energy formulation of α, γ, and liquid Fe_2SiO_4 using Grover, Getting and Kennedy's empirical relation between volume and bulk modulus. Geochim Cosmochim Acta 65:4231–4242

Kudoh Y, Takeda H (1986) Single crystal X-ray diffraction study on the bond compressibility of fayalite, Fe_2SiO_4 and rutile, TiO_2 under high pressure. Physica B 139-140:333–336

Lashley JC, Hundley MF, Migliori A, Sarrao JL, Pagliuso PG, Darling TW, Jaime M, Cooley JC, Hults WL, Morales L, Thoma DJ, Smith JL, Boerio-Goates J, Woodfield BF, Stewart GR, Fisher RA, Phillips NE (2003) Critical examination of heat capacity measurements made on a Quantum Design physical property measurement system. Cryogenics 43:369–378

Marumo F, Isobe M, Akimoto S (1977) Electron-density distributions in crystals of γ-Fe_2SiO_4 and γ-Co_2SiO_4. Acta Crystallogr Sect B 33:713–716

Robie RA, Finch CB, Hemingway BS (1982) Heat capacity and entropy of fayalite (Fe_2SiO_4) between 5.1 and 383 K: comparison of calorimetric and equilibrium values of the QFM buffer reaction. Am Mineral 67:463–469

Robie RA, Hemingway BS (1972) Calorimeters for heat of solution and low-temperature heat capacity measurement. U.S. Geol Surv Prof Paper 755, 32p

Robie RA, Hemingway BS (1995) Thermodynamic properties of minerals and related substances at 298.15 K and 1 bar (10^5 Pascals) pressure and at higher temperatures. US Geol Surv Bull 2131, 461 pp

Santoro RP, Newnham RE, Nomura S (1966) Magnetic properties of Mn_2SiO_4 and Fe_2SiO_4. J Phys Chem Solids 27:655–666

Sato Y (1977) Equation of state of mantle minerals determined through high-pressure X-

ray study. In: Manghnani MH, Akimoto S (eds) High–Pressure Research: Application in Geophysics. Academic Press, New York, pp 307–323

Sung CM, Burns RG (1976) Kinetics of high-pressure phase transformations: implications to the evolution of the olivine-spinel transition in the downgoing lithosphere and its consequences on the dynamics of the mantle. Tectonophys 31:1–32

Watanabe H (1982) Thermochemical properties of synthetic high-pressure compounds relevant to the earth's mantle. High-pressure research in geophysics (ed. Manghnani, M. H. and Akimoto, S.), Center for Academic Publications, Japan, pp 441–464

Xie, ZD, Sharp TG (2004) High-pressure phases in shock-induced melt veins of the Umbarger L6 chondrite: constraints of shock pressure. Meteoritics Planet Sci 39:2043–2054

Xie ZD, Tomioka N, Sharp TG (2002) Natural occurrence of Fe_2SiO_4-spinel in the shocked Umbarger L6 chondrite. Am Mineral 87:1257–1260

Yagi T, Akaogi M, Shimomura O, Suzuki T, Akimoto S (1987) In situ observation of the olivine-spinel phase transition in Fe_2SiO_4 using synchrotron radiation. J Geophys Res 92:6207–6213

Yong W, Dachs E, Withers AC, Essene EJ (2006) Heat capacity and phase equilibria of hollandite polymorph of $KAlSi_3O_8$. Phys Chem Minerals 33:167–177

CHAPTER V

CONCLUSIONS

This dissertation comprises a study of the thermodynamic properties of some high pressure phases and their phase equilibria under mantle conditions. Three phases were synthesized to undertake calorimetric measurements: K-hollandite ($KAlSi_3O_8$), Si-wadeite ($K_2Si_4O_9$) and γ-Fe_2SiO_4. The measured calorimetric results and their practical applications in mantle petrology and ultra-high pressure metamorphic petrology are presented in the corresponding three chapters (II, III and IV). The first thing that can be learned from these results is that the heat capacity option of Physical Properties Measurement System (PPMS) can routinely measure the heat capacity of milligram sized samples in the temperature range of 5-303 K, which is ideal for high pressure phases and synthetic materials. PPMS provides a powerful tool to study the high pressure mineralogy and petrology.

In Chapter II, the phase equilibria related to K-hollandite are calculated thermodynamically with the help of newly measured low-temperature heat capacity data using PPMS. The contribution of configurational entropy due to disorder of Al and Si atoms in the octahedral sites is incorporated in the entropy of K-hollandite at standard state, which is 166.2 ± 0.2 $Jmol^{-1}K^{-1}$. Although these calculations generally agree with

previous experimental results, a better constraint in terms of the slopes of phase transition boundaries was achieved. Three reactions that can lead to the formation of K-hollandite all suggest that K-hollandite can be formed at pressures above 9 GPa and will be stable until 22 GPa, where K-hollandite will transform to a new structure called hollandite II. Therefore, K-hollandite might be a possible host mineral for potassium in the earth's upper mantle and transition zone especially along the subduction slab. Three phase transitions that have not been discovered by experiments are also predicted after putting the thermodynamic data of K-hollandite and Si-wadeite into the current thermodynamic data base of $K_2O-Al_2O_3-SiO_2$ system. This demonstrates another merit of thermodynamic calculation. Not only can the existing phase transitions be calculated, but also the unknown phase transition can be predicted.

In Chapter III, the low-temperature heat capacity of Si-wadeite measured by PPMS is presented. From integration of the heat capacity data measured by PPMS, the entropy of Si-wadeite at standard pressure and temperature is calculated to be 253.8 ± 0.6 $Jmol^{-1}K^{-1}$. The phase transitions related to Si-wadeite were studied both thermodynamically and experimentally, which preclude the previous prediction that suggests a possible equilibrium stability field of kalsilite + coesite intervening between the stability field of K-feldspar and that of coesite + kyanite + Si-wadeite. The uncertainties of thermodynamic calculation are also examined and compared with the uncertainties of high pressure experiments. The essence of an experimental result related to kalsilite and Si-wadeite is displayed through thermodynamic calculation. These

calculations and previous experiments all suggest that Si-wadeite is possible to be as an index mineral for ultra-high pressure metamorphic rocks, and yet needed to be confirmed by field observations. Besides, like K-hollandite, Si-wadeite is also a possible host mineral for potassium along the subduction slab in the Earth's mantle.

In Chapter IV, the low-temperature heat capacity data of γ-Fe_2SiO_4 are reported for the first time. The entropy and Gibbs free energy at standard pressure and temperature are calculated to be 140.2 ± 0.4 $Jmol^{-1}K^{-1}$ and −1369.3 ± 2.7 $Jmol^{-1}K^{-1}$ based on the measured heat capacity data. Similar to other Fe-containing silicates, a broad λ-transition due to paramagnetic−antiferromagnetic transition is also exhibited in the low-temperature heat capacity of γ-Fe_2SiO_4. The transition temperature, also known as the Néel temperature, is located to be at 11.8 K by the low-temperature heat capacity data of γ-Fe_2SiO_4. The gap in the heat capacity data between 303 and 350 K of γ-Fe_2SiO_4 is an obstacle to calculate the phase transitions at high temperatures. However, the phase transition boundary of fayalite−γ-Fe_2SiO_4 at 298 K can be located at 2.4 ± 0.6 GPa and the slope of the phase transition boundary is calculated to be 25.4 bars/K, which is consistent with extrapolated results of previous experimental studies.

In conclusion, the major contribution of this dissertation is that the low temperature heat capacity data of these high pressure phases, which are critical to the thermodynamic modeling of phase relations that have direct application to mantle petrology and ultra-high pressure metamorphic petrology and yet not available previously due to practical reasons, are accurately measured for the first time. The

thermodynamic data of K-hollandite, Si-wadeite and γ-Fe_2SiO_4 would help us to better constrain and model the composition and structure of the Earth's mantle.

It is unlikely that much K-hollandite and Si-wadeite would survive in the Earth's upper mantle and transition zone because most potassium would probably be dissolved into pyroxene and/or garnet, and there may not be enough potassium that can form its own phase in the mantle. However, it is quite possible that either or both of them can be found locally in the mantle especially along the subduction slab where the concentration of potassium is relatively higher than the normal mantle so that even some potassium minerals such as K-feldspar and muscovite can be stable. This hypothesis is supported by high pressure high temperature experiments in which K-hollandite has been reported among the experimental run products at pressures higher than 8−11 GPa in bulk compositions corresponding to average continental crust, subducted terrigenous and pelagic sediments, basalts and metapelites (Irifune et al. 1994; Domanik and Holloway 1996, 2000; Schmidt 1996; Ono 1998; Wang and Takahashi 1999). Unlike K-hollandite whose experimental appearance can be found in various bulk compositions, Si-wadeite has only been reported experimentally in relatively simple systems in the pressure range of 5−16 GPa partly due to its high potassium concentration and its limited formation conditions compared to K-hollandite. Nonetheless it is still possible for Si-wadeite to occur in metapelites and metagranitoids that have been subducted at depths greater than 170 km. Neither of them has been discovered in UHP rocks probably because the UHP rocks that exceeded >6 GPa have not been recovered on the Earth's surface so far. This

doesn't necessarily mean that such high pressure UHP rocks do not exist. Three decades ago, people didn't recognize the existence of UHP rocks until coesite and diamond were found in supracrustal rocks. There is no reason to underestimate the possibility of further surprises. Sooner or later UHP rocks >6 GPa may be found on the Earth's surface and either K-hollandite or Si-wadeite, or their decompressed equivalents, might be recovered from these rocks.

The new thermodynamic data of γ-Fe_2SiO_4 will help to better constrain the 440 km, 520 km and 660 km seismic discontinuities. The exact depth and thickness of these seismic discontinuities as well as the exact compositions of the upper mantle and transition zone can only be accurately modeled with precise thermodynamic data of the $(Mg, Fe)_2SiO_4$ system. Given the thermodynamic data of the end-members of $(Mg,Fe)_2SiO_4$ system, a good solid solution model is then needed for the thermodynamic calculation. Measuring themodynamic data of the solid solution series in the system will help us to establish a better solid solution model. Like K-hollandite, γ-Fe_2SiO_4 has also been found in meteorites (Xie et al. 2002), suggesting its possible existence in other planets.

As with all techniques, thermodynamic calculations also have drawbacks. Several obstacles stand in the way of thermodynamic studies of phases under mantle conditions. For most mantle phases, the temperature dependence of bulk modulus is not available, which means the bulk modulus derived at room temperature is used for these high pressure phases, although the actual uncertainties may be more or less cancelled if the

lower pressure phases also use the bulk modulus at room temperature. The pressure dependence of bulk modulus is also not well studied for some mantle phases. This may cause unexpected error if the thermodynamic calculation is undertaken at higher pressures than the pressures at which the bulk modulus is derived. The thermal expansion of these high pressure phases is also derived at relatively limited temperature range, whereas the thermodynamic calculation is usually done at much high temperatures. The biggest challenge for thermodynamic calculation of minerals under mantle conditions probably comes from the extrapolation of the heat capacity data to high temperatures. For those high pressure phases, the heat capacity is usually measured up to 700 K. Above 700 K, it is very difficult to obtain high quality data because these high pressure phases will start reacting back to its corresponding low pressure phases. Most phases would not fully excite all the lattice vibrations at 700 K, therefore the heat capacity data are still not close to the Dulong and Petit limit ($C_v=3nR$) and huge error might be produced if the heat capacity data are not extrapolated in the right form. This problem will continue to exist until a machine is invented that can measure the heat capacity and enthalpy under high pressures. Tightly reversed experimental phase equilibria could be combined with current thermodynamic data to better constrain the entropy and volume of the phases at higher P-T. This alternative approach is one way to produce thermodynamic data at high P-T. The other approach is quantum mechanical calculations in order to better constrain these data in regions where it cannot be measured. Such alternatives may provide sufficient data to undertake more general calculations of deep mantle phase equilibria in the more general

system K_2O-Na_2O-FeO-MgO-Al_2O_3-SiO_2-H_2O and predict deep assemblage along the mantle geotherms for common rock compositions. Some of this work has been initiated by Stixrude and Lithogow-Bertelloni (2005) for basaltic and pyrolite bulk compositions.

REFERENCES

Domanik KJ, Holloway JR (1996) The stability and composition of phengitic muscovite and associated phases from 5.5 to 11 GPa: implications for deeply subducted sediments. Geochim Cosmochim Acta 60:4133–4150

Domanik KJ, Holloway JR (2000) Experimental synthesis and phase relations of phengitic muscovite from 6.5 to 11 GPa in a calcareous metapelite from the Dabie Mountains, China. Lithos 52:51–77

Irifune T, Ringwood RE, Hibberson WO (1994) Subduction of continental crust and terrigenous and pelagic sediments: and experimental study. Earth Planet Sci Lett 126:351–368

Ono S (1998) Stability limits of hydrous minerals in sediment and mid–ocean ridge basalt compositions: implications for water transport in subduction zones. J Geophys Res 103:18,253–18,267

Stixrude L, Lithgow-Bertelloni C (2005) Mineralogy and elasticity of the oceanic upper mantle: Origin of the low-velocity zone. J Geophys Res 110 B03204, doi:10.1029/2004JB002965

Wang W, Takahashi E (1999) Subsolidus and melting experiments of a K-rich basaltic composition to 27 GPa: implication for the behavior of potassium in the mantle. Am Mineral 84:357–361

Xie ZD, Tomioka N, Sharp TG (2002) Natural occurrence of Fe_2SiO_4-spinel in the shocked Umbarger L6 chondrite. Am Mineral 87:1257–1260

APPENDICES

APPENDIX A

RAMAN SPECTROSCOPIC STUDY OF GRAPHITE IN MARBLES: APPLICATION AS A NEW GEOTHERMOMETER

ABSTRACT

Organic matter originally present in the sedimentary rocks is progressively transformed into graphite during metamorphism. The degree of graphitization may be a reliable indicator of metamorphic grade, especially in terms of the peak metamorphic temperature and is not affected by retrogression. Raman spectroscopy is a rather good technique to characterize the degree of graphitization. The previously determined relationship between the Raman spectra of the graphite and the peak metamorphic temperature of the host rocks was applied in this paper to some marbles from the Elzevir Terrane of the Grenville Orogen in southern Ontario. Raman spectra of graphite were collected on 10 thin sections and more than 80 graphite grains. The peak metamorphic temperature calculated by the Raman spectrum geothermometer is 380°C to 510°C, more than 100°C lower than the results based on conventional thermobarometers. This discrepancy is likely partially, if not mainly, caused by the different analytical procedures in different labs as mentioned in previous studies. A standard analytical procedure of Raman spectroscopy measurements for graphite in metamorphic rocks is suggested to be established to obtain reproducible results from different laboratories. The relation

between the Raman spectra of the graphite and the peak metamorphic temperature of the host rocks should be recalibrated with standard analytical procedures.

INTRODUCTION

Carbonaceous material (CM) that forms from the organic material originally present is a widespread component of metamorphosed sediments. The CM materials range from kerogen to highly crystalline graphite, representing different degrees of graphitization and hence different degrees of crystallinity of graphite. The mechanisms of coalification from peat to anthracite are generally well understood by laboratory study, which shows that they have a time-temperature dependence. However, mechanisms of coalification from anthracite to graphite, which is commonly referred to as graphitization, remain unclear (Bustin et al. 1995a; Bustin et al. 1995b).

Many factors influence the degree of graphitization and the crystallinity of graphite: these include temperature, pressure, time, strain, original chemical composition and microtexture of the kerogen precursor (e.g., Bustin et al. 1995a). Landis (1971) tentatively concluded that graphitization is mainly controlled by metamorphic temperature, pressure and starting material. Itaya (1981) argued that graphitization is a rate process; the temperature of complete graphitization can vary between different metamorphic terranes due to different duration of metamorphism whereas the degree of graphitization is a useful indicator of relative metamorphic temperature in an individual metamorphic terrane. Buseck and Huang (1985) showed that the carbonaceous precursors in their study probably influence the graphitization. Pasteris and Wopenka (1991) showed that graphite structure records only the peak metamorphic temperature and therefore can

be used as a reliable indicator of metamorphic grade, and Wopenka and Pasteris (1993) correlated the degree of crystallinity of graphite with metamorphic grade. Wada et al. (1994) indicated that graphitization is mainly determined by temperature, duration of metamorphism and rock composition. Experiments of Bustin et al. (1995a, 1995b) indicated the high dependence on strain and strain energy in the formation of graphite under natural conditions. They also concluded that the crystallinity of graphite is a poor metamorphic index because graphitization is dependent on many factors. Suchy et al. (1997) further confirmed the importance of strain in the process of graphitization. The most important factor that influences the crystallinity of graphite is peak metamorphic temperature (Wada et al. 1994; Beyssac et al. 2002a, 2002b, 2003). Beyssac et al. (2002a) undertook experiments on the graphitization of CM and proposed a relationship of Raman spectra of graphite for use as a geothermometer in low to medium grade terranes.

Three analytical techniques are used to study the structural characterization of graphite: X-ray diffractometry (XRD), high resolution transmission electron microscopy (HRTEM), and Raman spectroscopy. The interplanar spacing (d value) can be quantitatively measured by XRD method which requires the disaggregation of the host rock as well as several mg of separated graphite (Landis 1971; Diessel et al. 1978; Itaya 1981; Bustin et al. 1995a, 1995b) . HRTEM can produce the images of the graphite and direct measurements of the dimension of stacks designated as Lc, the interplanar spacing d, and the lateral extent of carbon sheets, La (Buseck and Huang 1985; Bustin et al. 1995a, 1995b; Beyssac et al. 2002b, 2003). Raman study is a relatively new method that can provides information about the molecular bonds of the constituent structural units as well as the degree of crystalline order in solids. Thus, Raman spectra are used to reflect

the degree of crystallinity of graphite and turns out to be a more sensitive indicator of the metamorphic condition of the host rock than XRD or other types of studies (e.g., Pasteris and Wopenka 1991; Wopenka and Pasteris 1993; Beyssac et al. 2002a). Optical reflectivity measurements (vitrinite reflectance) have also used to characterize carbonaceous materials (Diessel and Offler 1975; Diessel et al. 1978; Okuyama-Kusunose and Itaya 1987)

The Raman spectrum of CM consists of two different spectral regions: the first between 1100 and 1800 cm^{-1} and the second between 2500 and 3100 cm^{-1} (Tuinstra and Koenig 1970; Nemanich and Solin 1979). They are usually referred to as "first-order" and "second-order" spectrum. In the first-order region, well-crystallized graphite has only one single peak at 1580 cm^{-1}, usually referred to as the G peak. However, for less-ordered CM three new peaks appear at 1350, 1620 and 1500 cm^{-1}, referred to as D1, D2 and D3 peak respectively (Tuinstra and Koenig 1970, Beyssac et al. 2002a) (Fig. A1). In the second-order region corresponding to combination and overtone scattering, four peaks are placed at 2450, 2735, 2940 and 3248 cm^{-1} (Wopenka and Pasteris 1993).

Beyssac et al. (2002a) identified a linear correlation between the R2 ratio and the peak metamorphic temperature in the temperature range of 330°C to 650°C:

$$T(°C) = -445R2 + 641 \quad (1)$$

where R2 represents the D1/(G+D1+D2) peak area ratio. Raman spectra of graphite therefore can be used as a geothermometer to determine the peak metamorphic temperature of metasediments. Rahl et al. (2005) extended this calibration down to 100°C by studying the Raman spectra of a suite of low-temperature meta-sediments from the Olympics Mountains in the state of Washington. The thermal history of these samples is

constrained by the apatite and zircon fission-track and (U-Th)/He ages.

Raman studies of graphite in metamorphic rocks have mainly focused on metapelites rather than marbles. The quantitative relationship between Raman spectra of graphite and the metamorphic grade of the host rocks especially marbles still needs to be further constrained. Graphitic marbles whose peak metamorphic temperatures are well-constrained will be used for this study to test the role of host rocks.

GEOLOGICAL BACKGROUND AND ANALYTICAL METHOD

Field Area

The Elzevir Terrane of the Grenville Orogen in southern Ontario (Fig. A2) is selected to be the field area of this study because of three great advantages. First, the Elzevir Terrane contains abundant graphitic marbles that were regionally metamorphosed from upper greenschist to upper amphibolite facies (Rathmell et al. 1999). Second, the peak metamorphic temperatures of these graphitic marbles were well studied and indicate a temperature range from 500-650°C by three conventional geothermometers (Rathmell et al. 1999). These well-constrained temperature conditions provide a good test for Raman-spectrometry. Third, mylonite marbles that occur in the Bancroft Shear zone (Carlson et al. 1990) can be used to study the influence of strain on the degree of crystallinity of graphite. Graphitic marbles were collected in several locations from this field area.

Experimental Procedures

Conventional petrographic thin sections are used to obtain the Raman spectra of

graphite contained in the black marble with two main advantages. First, in situ measurements can be performed and thus the relationship between CM and the surrounding mineral matrix can be carefully checked (Beyssac et al. 2002). A better heat removal can be obtained by the mineral matrix than similar grains laid on slides without matrix so that a higher signal to noise ratio can be achieved (Wopenka and Pasteris 1993). Thin sections were cut perpendicular to the foliation and parallel to the lineation whenever possible to avoid the orientation effects (Katagiri et al. 1988; Wang et al. 1989; Compagnini et al. 1997) except for the samples beginning with OODMC.

Graphite was identified using the petrological microscope and the scanning electron microscope (SEM). It can be recognized by its characteristic anisotropy under reflected light and its opacity in transmitted light (Fig. A3). Most of the graphite grains in the thin sections are elongate tablets. In cross-section, the length of these graphite plates is 6-30 μm and the width is less than 3 μm. Although these are small grains, they can be located by examining opaque areas in the marble at high magnification in reflected light. Although graphite exists separately as thin tablets in most cases, irregular graphite clusters were also identified.

Thin sections that contain graphite grains were chosen for Raman spectroscopic study. Different graphite grains in the same thin section were examined. Sometimes, even Raman spectra of different parts of the same big graphite grain were collected to test the homogeneity. Raman spectra were collected in the 1100−1800 cm^{-1} region which includes all the first-order peaks. Peak position, peak width and peak area are determined by fitting the spectrum with PseudoVoigts functions and the results are shown in Table A1. The minerals observed in each sample are shown in Table A2.

.

RESULTS AND DISCUSSION

In this study ten thin sections and more than 80 graphite grains were used to collect Raman spectra. The peak metamorphic temperatures of these graphitic marbles calculated using equation (1) are shown in Table 1. The average temperatures given by these Raman spectra of the thin sections range from 380 to 510°C, considerably lower than the peak metamorphic temperatures determined by three conventional geothermometers (Rathmell et al. 1999), which showed that the peak metamorphic temperatures of this region is in the range 500−650°C. If ignoring the results from those thin sections whose orientation has not been specially addressed (samples beginning with OODMC), the average temperatures given by the rest thin sections are even lower, ranging from 380 to 430°C.

Several factors may explain the difference of peak metamorphic temperature of these marbles between the Raman spectra geothermometer and the three traditional geothermometers for the Madoc-Bancroft transect. The first one is that equation (1) is not suitable for marbles, because it was generalized based mostly on mica schist and black shale by Beyssac et al. (2002a). Only two marble samples were applied in their study. This may lead to certain error when using equation (1) on marble samples. Rock composition and carbonaceous precursors may influence graphitization by a catalytic influence on the formation of graphite (Diessel et al. 1978; Buseck and Huang 1985). Wada et al. (1994) showed that the degree of graphitization is different in limestones and pelitic rocks from the Ryoke metamorphic terrane and it indicated that the graphitization advanced further in limestones than in pelitic rocks in the low temperature range. As a

result, two different linear correlations between the degree of graphitization and metamorphic temperature were proposed. However, according to their studies, higher temperatures would be gained if applying the linear relationship of pelitic rocks to marble, which is in contradiction with the results from this study, in which lower temperature values were obtained. Therefore, the composition of the host rock is unlikely to be the main reason of the difference between results derived from Raman spectra and that from traditional geothermometers based on the studies by Wada et al. (1994)..

The second factor that needs consideration is the graphite orientation effect of Raman spectrum. The effect of graphite orientation with respect to the incident laser beam on the recorded Raman spectrum is well known (Katagiri et al. 1988; Wang et al. 1989; Wopenka and Pasteris 1993; Compagnini et al. 1997). An (001) plane (or basal plane, which is perpendicular to the c axis of the graphite crystal) shows a very different Raman spectrum than the vertical plane (called edge plane in their papers) which includes the c axis of graphite crystal. The 1350 cm^{-1} (D1 peak) almost disappears in the near horizontal orientation whereas in the near vertical position the D1 peak is maximized (Katagiri et al. 1988; Wang et al. 1989; Compagnini et al. 1997). In other words, the D1 peak gradually changes from maximum to undetectable as the angle between the c axis of the crystal and the laser beam decrease from 90° to 0° (Wang et al. 1989). Beyssac et al. (2002a) cut their thin sections perpendicular to the foliation and parallel to the stretching lineation so that the graphite is in the near vertical plane, i.e., the c axis of the crystal is perpendicular to the laser beam. Hence equation (1) is based on near vertical plane, but a large error will ensue if equation (1) is used in a plane far from the near vertical plane. If the graphite is not in the near vertical plane, the D1 peak will be weaker than that in the

near vertical plane, thus the R2 value will be small, and hence the temperature calculated by equation (1) will be much higher. If the graphite is in the horizontal plane, equation (1) will almost gives the highest temperature value that it can ever provide, i.e. 641°C. The thin sections in this study were prepared in the same way as Beyssac et al. (2002a) except for samples beginning with OODMC. Therefore, the orientation effect should be negligible for most samples and would not cause the difference between results derived from the Raman spectra and that from the traditional geothermometers. The orientation effect should lead only to higher temperatures. This might be the cause of the high temperatures generated by nonoriented samples (Table A1, those beginning with OODMC). Those samples, generate Raman temperatures around 500°C, comparable to the results obtained by Rathmell et al. (1999).

The third factor that might result in different temperatures lies in the data analysis process. If different functions are selected to fit the background and the peaks, the parameters such as the peak high, peak area and even peak position will also be different, thus the temperature calculated based on these parameters will also be different. Beyssac et al. (2002a) used a flat background for the background. However, the background of the Raman spectra collected in this study is seldom flat. A tilted or curved background is found more commonly for the Raman spectra collected in this study. Wong et al. (2007) observed inclined backgrounds and examined the reproducibility of Raman spectroscopy measurements for carbonaceous material in metamorphic rocks. They reported that reproducible results are possible from different laboratories, but care must be taken with the background and the peak-fitting process. They found a second order polynomial is needed to fully remove the background and it was better to fit peaks to an

integrated spectrum of the individual spectra of a specific sample. Otherwise, significant bias in the results may be induced from laboratory to laboratory. The special treatment suggested by Wong et al. (2007) were not used by Beyssac et al. (2002a) in their derivation of equation (1), which means special care should be taken for other labs to collect Raman spectra and use equation (1) to calculate the peak metamorphic temperature. According to Wong et al. (2007), it is possible that quite different peak metamorphic temperatures for the same rock would be calculated using equation (1) in different laboratories, not to mention the comparison with other geothermometers. It is very likely that lower peak metamorphic temperatures of the marbles given by the Raman spectra in this study, are if not mainly, at least partially caused by the above analytical problems.

The signal-noise ratio or the resolution of the Raman spectra collected in this study is variable. For those Raman spectra with poor signal-noise ratio or resolution, the uncertainties of the peak parameters from fitting may lead to large errors in the Raman temperatures. Nonetheless even the spectra that do have good resolution produce lower temperatures, which suggest that the error of this study, if there is any, is systematic, not random. A standard analytical procedure of Raman spectroscopy measurements for graphite in metamorphic rocks will greatly reduce such errors and should be established first before any precise results can be obtained through equation (1), or maybe even equation (1) should be recalibrated in such standard analytical procedures.

The mylonite marbles shows no apparent difference compared to ordinary marble in terms of yielding temperatures from Raman spectra. Either strain doesn’t play a role in the graphitization process or its effect is too small to be detected. Considering the large

uncertainties in processing the Raman spectra of the aforementioned graphite samples, it's impossible to distinguish these two under current condition.

ACKNOWLEDGMENTS

We warmly thank Katie Davis, Ni Sun and Fuxiang Zhang for access to the Raman spectroscopic facilities in the Department of Geological Sciences and their assistance in operating the system. Professor Adam J. Matzger is also appreciated for providing access to the Raman spectroscopic facility in the Department of Chemistry.

Table A1 Parameters from decomposition of Raman spectra and calculated peak metamorphic temperature using equation (A1)

Slide number	Sample number	G position	D1 position	D2 position	R2 ratio	Temperature (°C)
BA-04-01-2	BA12-11	1582.65	1355.33	1623.42	0.47	428
(45’06623N	BA12-12	1582.50	1355.74	1623.30	0.43	444
77’82200W)	BA12-21	1583.41	1355.18	1623.77	0.53	399
	BA12-31	1582.91	1353.81	1623.78	0.43	444
	BA12-41	1582.80	1354.18	1622.95	0.52	407
	BA12-42	1582.70	1354.46	1622.99	0.45	435
	Average	1582.83	1354.78	1623.37	0.47	425
	1σ	0.32	0.75	0.36	0.04	19
BA-04-01-3	BA13-11	1582.82	1355.98	1622.04	0.57	381
(45’06623N	BA13-21	1583.11	1354.38	1622.63	0.55	391
77’82200W)	Average	1582.96	1355.18	1622.34	0.56	386
	1σ	0.21	1.13	0.42	0.02	7
KL-04-03	KL31-1	1582.84	1355.64	1622.76	0.59	372
(44’56065N	KL31-2	1582.79	1355.39	1622.79	0.60	368
77’24516W)	KL31	1582.86	1355.77	1622.91	0.60	369
	KL32-1	1582.38	1354.63	1621.97	0.56	387
	KL32-2	1582.97	1354.19	1622.84	0.39	464
	KL33-1	1582.53	1354.36	1623.01	0.52	406
	KL34-1	1582.21	1354.08	1623.11	0.45	434
	KL35-1	1581.77	1353.32	1622.46	0.35	484
	KL36-1	1582.16	1353.69	1623.22	0.45	435
	KL36-2	1582.37	1355.25	1623.40	0.57	380
	KL37-3	1582.78	1355.09	1621.45	0.58	376
	KL37-4	1583.25	1354.10	1622.71	0.59	375
	KL37-5	1582.66	1355.53	1621.07	0.58	376
	KL37-6	1582.74	1355.68	1622.42	0.59	372
	Average	1582.59	1354.77	1622.58	0.53	400
	1σ	0.38	0.81	0.67	0.08	39
KL-04-04	KL41-1	1586.28	1357.00	1625.91	0.50	414
(44’56065N	KL41-2	1586.36	1357.70	1625.77	0.50	415
77’24516W)	KL41-3	1587.44	1358.79	1629.16	0.60	369
	KL43-1	1586.63	1358.36	1625.89	0.57	381
	KL43-3	1586.18	1356.18	1616.56	0.50	416
	KL45-1	1586.63	1355.80	1630.62	0.49	417

	KL45-2	1587.80	1360.27	1627.27	0.57	383
	Average	1586.76	1357.73	1625.88	0.53	399
	1σ	0.62	1.56	4.51	0.05	21
SH-04-01	SH10-1	1583.31	1355.99	1622.00	0.59	375
(44’79494N	SH10-2	1582.76	1355.00	1622.75	0.54	396
76’69440W)	SH10-3	1583.15	1355.36	1621.86	0.60	370
	SH10-4	1582.76	1355.49	1622.92	0.58	378
	SH11-1	1587.05	1360.07	1626.24	0.59	371
	SH11-2	1586.84	1359.96	1627.67	0.55	391
	SH11-3	1586.65	1359.23	1626.41	0.54	397
	SH11-4	1586.77	1358.72	1628.25	0.48	423
	SH12-1	1587.42	1359.71	1622.30	0.59	374
	SH12-2	1587.42	1359.80	1625.14	0.57	384
	SH12-3	1587.31	1358.86	1627.30	0.59	375
	SH12-4	1588.00	1358.69	1631.37	0.58	376
	SH13-2	1587.70	1360.56	1630.92	0.58	379
	SH13-31	1583.17	1355.48	1618.87	0.50	415
	SH13-	1583.89	1356.07	1624.88	0.58	379
	SH14-1	1588.30	1358.66	1619.64	0.57	384
	SH14-2	1588.67	1359.66	1635.21	0.56	387
	SH15-1	1586.50	1359.38	1622.59	0.56	387
	SH15-2	1583.15	1354.68	1623.18	0.54	396
	SH15-3	1583.69	1354.89	1622.68	0.60	369
	SH15-4	1583.97	1354.63	1621.33	0.64	351
	SH16-1	1583.90	1355.03	1623.38	0.57	384
	SH16-2	1582.29	1354.06	1621.21	0.61	364
	SH17-2	1582.95	1355.86	1619.58	0.56	384
	SH17-3	1583.37	1355.18	1618.84	0.57	383
	SH18-1	1583.16	1355.92	1622.93	0.60	368
	SH18-2	1582.96	1355.86	1622.19	0.58	376
	SH19-1	1583.93	1352.92	1621.88	0.61	366
	SH19-2	1583.08	1355.12	1622.87	0.58	376
	SH	1583.00	1354.11	1619.33	0.58	379
	Average	1584.90	1356.83	1623.86	0.57	381
	1σ	2.13	2.29	3.90	0.03	14
TH-04-02	TH21-1	1583.61	1353.85	1624.62	0.50	415
(44’93493N	TH22-1	1584.18	1355.60	1624.42	0.58	377
78’30777W)	TH22-2	1583.35	1355.21	1622.59	0.51	408
	TH22-3	1583.93	1356.30	1624.69	0.50	415

	TH22-4	1584.54	1355.46	1624.25	0.57	384
	TH22-5	1584.32	1355.46	1619.47	0.58	379
	TH23-1	1584.57	1355.81	1623.69	0.57	383
	TH23-2	1583.56	1355.33	1624.38	0.62	360
	TH24-1	1583.84	1355.61	1623.40	0.53	398
	TH24-2	1584.12	1354.60	1624.18	0.48	421
	TH25-1	1584.17	1355.63	1620.86	0.53	401
	TH25-2	1583.82	1354.99	1620.79	0.51	410
	TH26-1	1580.33	1351.58	1620.19	0.47	429
	TH26-2	1580.94	1352.36	1620.14	0.55	392
	TH26-3	1582.04	1351.62	1620.00	0.59	371
	TH26-4	1581.78	1351.70	1618.07	0.60	369
	TH28-1	1581.58	1350.98	1618.58	0.62	361
	TH29-1	1581.45	1352.44	1620.26	0.49	416
	TH29-2	1580.09	1352.38	1618.88	0.47	429
	TH211-1	1579.12	1349.64	1617.49	0.54	394
	Average	1582.77	1353.83	1621.55	0.54	396
	1σ	1.69	2.02	2.48	0.05	22
OOMDC-19 (44’50344N, 77’50042W)	g64	1577.41	1351.02	1615.14	0.36	475
OOMDC-20 (44’50344N 77’50042W)	g103	1577.89	1353.44	1615.92	0.33	492
	g110	1578.57	1353.24	1617.05	0.39	465
	g119	1576.77	1353.17	1617.89	0.32	493
	g106	1570.44	1349.43	1609.01	0.09	601
	Average	1575.92	1352.32	1614.97	0.28	513
	1σ	3.73	1.93	4.05	0.13	60
OOMDC-24 (44’50344N 77’50042W)	g123	1578.74	1352.81	1619.70	0.35	481
	g129	1577.89	1351.50	1617.21	0.35	482
	g135	1575.85	1351.96	1614.94	0.29	511
	Average	1577.49	1352.09	1617.28	0.33	491
	1σ	1.49	0.66	2.38	0.04	17
OOMDC-34 (44’50344N 77’50042W)	g89	1578.89	1353.40	1620.40	0.32	497
	g93	1579.49	1352.77	1617.30	0.46	433
	Average	1579.19	1353.09	1618.85	0.39	465
	1σ	0.42	0.45	2.19	0.10	45

Table A2. Minerals observed in each sample

Sample	Minerals Observed
BA-04-01-2	talc, calcite/dolomite, graphite
BA-04-01-3	talc, calcite/dolomite, graphite
KL-04-03	tremolite, talc, calcite/dolomite, graphite
KL-04-04	tremolite, talc, calcite/dolomite, graphite
SH-04-01	talc, calcite/dolomite, graphite
TH-04-02	talc, calcite/dolomite, graphite
OOMDC-19	talc, calcite/dolomite, graphite
OOMDC-24	calcite/dolomite, graphite
OOMDC-34	calcite/dolomite, graphite

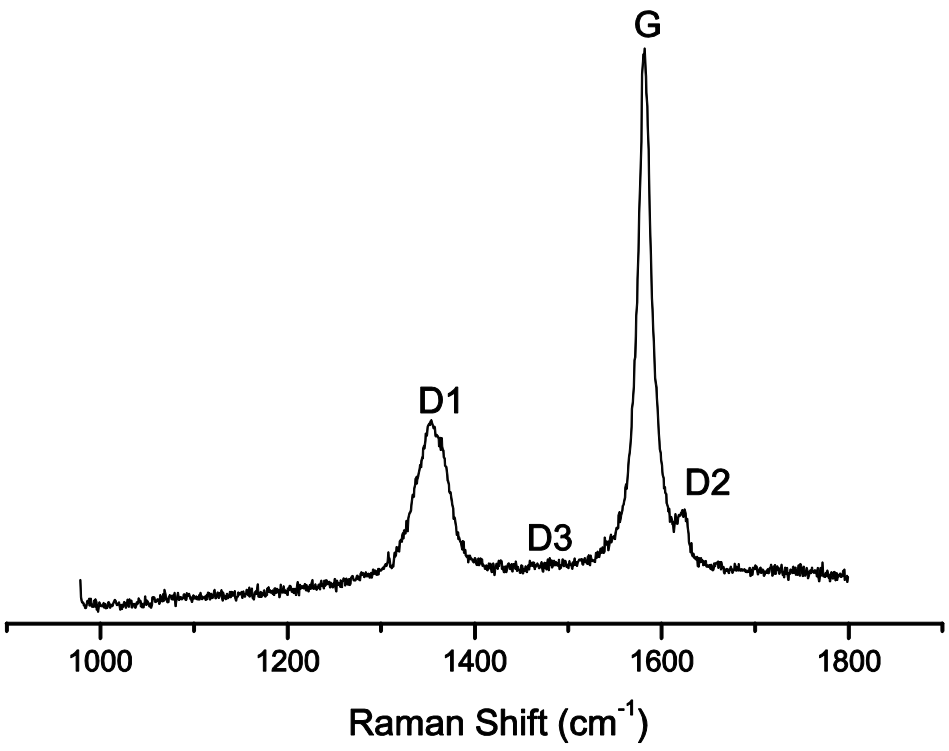

Fig. A1 Example of the first-order region of Raman spectrum of graphite. A linear function is used to fit the background. The Raman spectra are fitted with Pseudo Voigts functions to get the position and area parameters of the peaks.

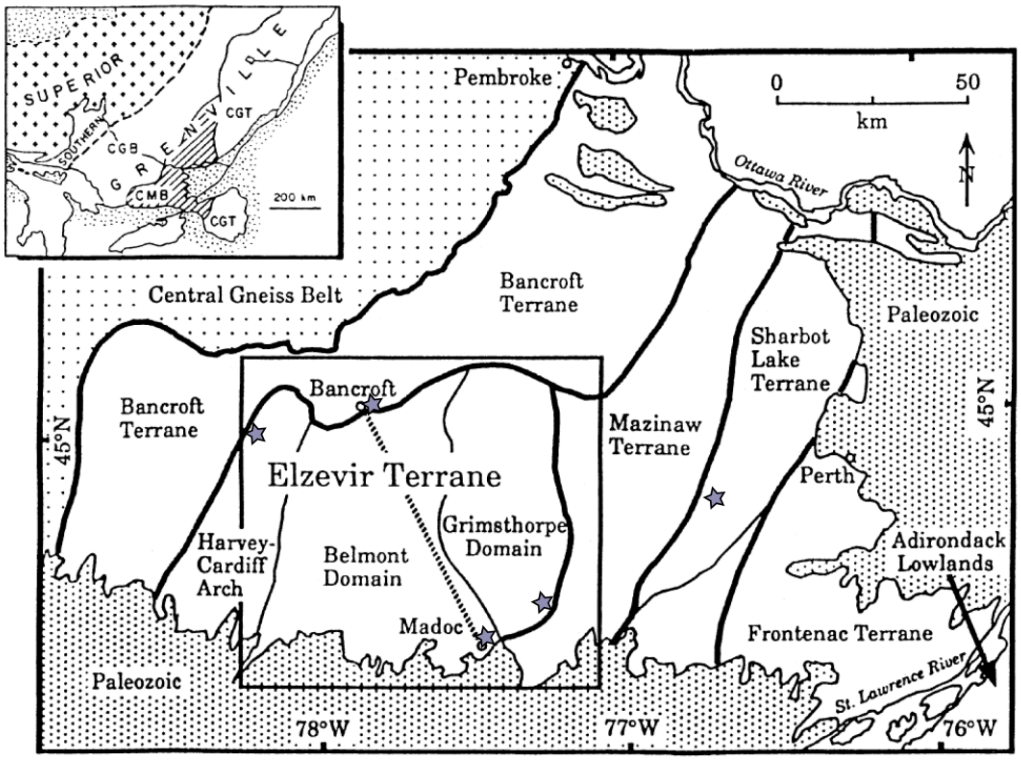

Fig. A2 Tectonic map of south-eastern Ontario, Canada (from Rathmell et al. 1999). Stars represent the locations of the samples.

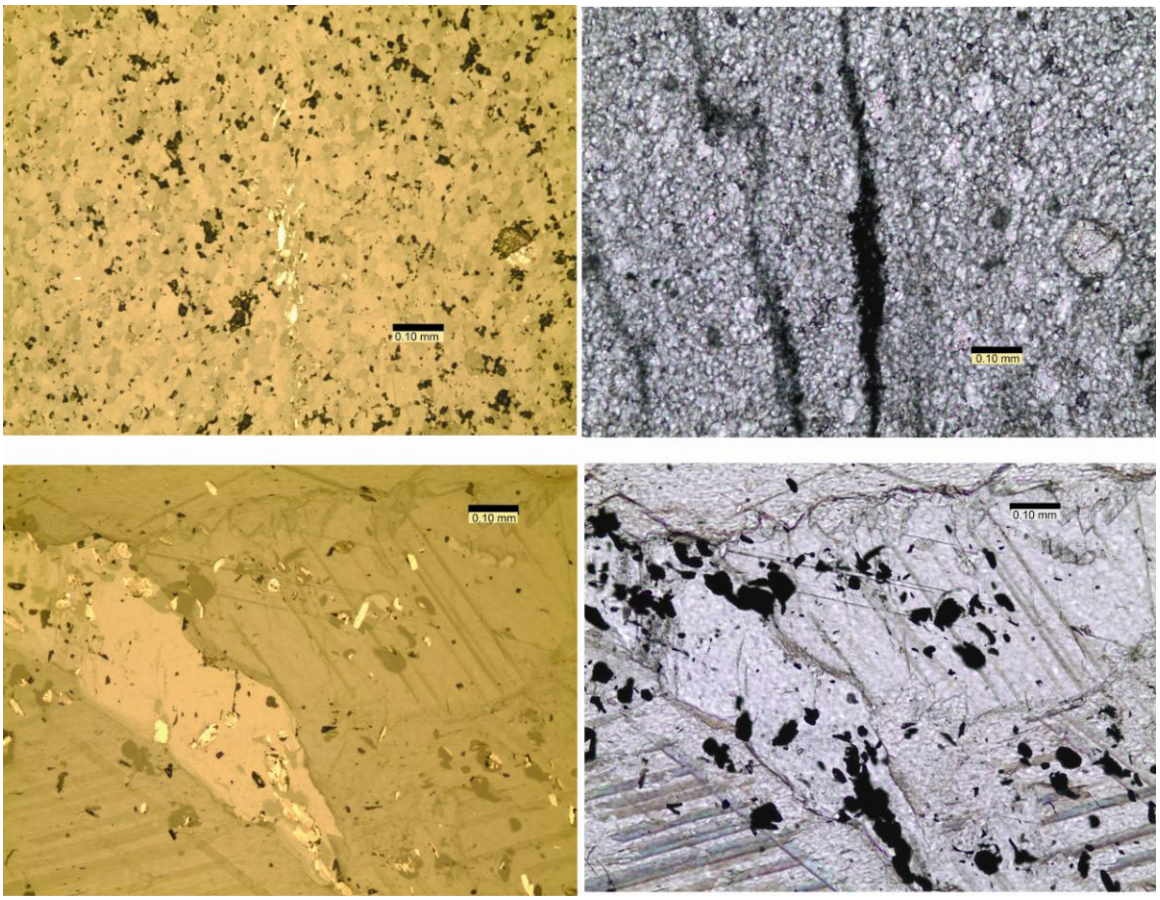

Fig. A3 Examples of graphite under microscope. Top photos: graphite in mylonite marbles. Bottom photo: graphite in ordinary marbles. Left photos: graphite under transmitted light. Right photos: graphite under reflected light.

REFERENCES

Beyssac O, Goffé B, Chopin C, Rouzaud JN (2002a) Raman spectra of carbonaceous material in metasediments: a new geothermometer. J Metam Geol 20:859–871

Beyssac O, Rouzaud JN, Goffé B, Brunet F, Chopin C (2002b) Graphitization in a high-pressure, low temperature metamorphic gradient: a Raman microspectroscopy and HRTEM study. Contr Mineral Petrol 143:19–31

Beyssac O, Brunet F, Petitet JP, Goffé B, Rouzaud JN (2003) Experimental study of the microtextural and structural transformations of carbonaceous materials under pressure and temperature. Eur J Mineral 15:937–951

Buseck P, Huang B (1985) Conversion of carbonaceous material to graphite during metamorphism. Geochim Cosmochim Acta 49:2003–2016

Bustin RM, Ross JV and Rouzaud JN (1995a) Mechanisms of graphite formation form kerogen: experimental evidence. Internat J of Coal Geol 28:1–36

Bustin RM, Rouzaud JN, Ross JV (1995b) Natural graphitization of anthracite: experimental considerations. Carbon 33:679–691

Carlson KA, van der Pluijm BA, Hanmer S (1990) Marble mylonites of the Bancroft shear zone: evidence for extension in the Canadian Grenville. Geol Soc Am Bull 102:174–181

Cesare B, Maineri C (1999) Fluid-present anatexis of metapelites at EI Joyazo (SE Spain): constraints from Raman spectroscopy of graphite. Contr Mineral Petrol 135:41–52

Compagnini G, Puglisi O, Foti G (1997) Raman spectra of virgin and damaged graphite edge planes. Carbon 35:1793–1797

Diessel CFK, Offler R (1975) Change in physical properties of coalified and graphitized phytoclasts with grade of metamorphism. Neues Jb Mineral Monatsh 1975: 11–26

Diessel CFK, Brothers RN, Black PM (1978) Coalification and graphitization in high-pressure schists in New Caledonia. Contr Mineral Petrol 68:63–78

Itaya T (1981) Carbonaceous material in pelitic schists of the Sanbagawa metamorphic belt in central Shikoku, Japan. Lithos 14:215–224

Katagiri G, Ishida H, Ishitani A (1988) Raman spectra of graphite edge planes. Carbon 26:565–571.

Landis CA (1971) Graphitization of dispersed carbonaceous material in metamorphic rocks. Contr Mineral Petrol 30:34–45

Nemanich RJ, Solin SA (1979) First- and second-order Raman scattering from finite-size crystals of graphite. Phys Rev B 20:392–401

Okuyama-Kusunose Y, Itaya T (1987) Metamorphism of carbonaceous material in the Tono contact aureole, Kitakami Mountains, Japan. J Metam Geol 5:121–139

Pasteris JD, Wopenka B (1991) Raman spectra of graphite as indicators of degree of metamorphism. Can Mineral 29:1–9

Rahl JM, Anderson KM, Brandon MT, Fassoulas C (2005) Raman spectroscopic carbonaceous material thermometry of low-grade metamorphic rocks: calibration and application to tectonic exhumation in Crete, Greece. Earth Planet Sci. Lett.

240:339–354

Rathmell MA, Streepey MM, Essene EJ, van der Pluijm BA (1999) Comparison of garnet-biotite, calcite-graphite, and calcite-dolomite thermometry in the Grenville Orogen; Ontario, Canada. Contr Mineral Petrol 134:217–231

Suchy V, Frey M, Wolf M (1997) Vitrinite reflectance and shear-induced graphitization in orogenic belts: a case study from the Kandersteg area, Helvetic Alps, Switzerland. Internat J Coal Geol 34: 1–20

Tuinsra F, Koenig JL (1970) Raman spectrum of graphite. J Chem Phys 53:1126–1130

Wada H, Tomita T, Matsuura K, Iuchi K, Ito M, Morikiyo T (1994) Graphitization of carbonaceous matter during metamorphism with references to carbonate and politic rocks of contact and regional metamorphisms, Japan. Contr Mineral Petrol 118:217–228

Wang A, Dhamelincourt P, Duvessy J, Guerard D, Landais P, Lelaurain M (1989) Chacterization of graphite alteration in an uranium deposit by micro-Raman spectroscopy, X-ray diffraction, transmission electron microscopy and scanning electron microscopy. Carbon 27:209–218

Wong E, Brandon M, Pasteris J, Wopenka B, Dunn S, Karabinos P (2007) Reproducibility of Raman spectroscopy measurements for carbonaceous materials in metamorphic rocks. Eos Trans. AGU, 88(52), Fall Meet. Suppl., Abstract V13D–1587

Wopenka B, Pasteris JD (1993) Structural characterization of kerogens to granulite-facies

graphite: applicability of Raman microprobe spectroscopy. Am Mineral 78:533–557

APPENDIX B

THE $^{40}Ar/^{39}Ar$ CHRONOLOGY OF AKSU PRECAMBRIAN BLUESCHISTS IN WESTERN CHINA

ABSTRACT

Three metapelite samples from the world's best documented Precambrian blueschist terrane near Aksu, Xinjing, China, were dated by $^{40}Ar/^{39}Ar$ method on separated phengite grains. The resultant plateau ages are in the range of 740 to 760 (±5) Ma, which is in agreement with previous $^{40}Ar/^{39}Ar$ plateau age of 754±50 Ma measured on a Na-amphibole and about 20−40 Ma older than earlier K-Ar and Rb-Sr ages. Considering the ±20-30 Ma uncertainties of the K-Ar and Rb-Sr ages, the $^{40}Ar/^{39}Ar$ ages reported in this study are consistent with the K-Ar ages and Rb-Sr ages within the 2σ error region, and the $^{40}Ar/^{39}Ar$ ages of sample A-012 are in good agreement with their study within the 1σ error region. Due to the low peak metamorphic temperature of Aksu blueschist terrane (300−400°C), the $^{40}Ar/^{39}Ar$ plateau ages in this study are growth ages or very close to them, and they are inferred to represent approximately the timing of peak metamorphic temperatures. This is in good agreement with a previously proposed tectonic scenario that the Aksu region represents the collision zone between North and South Tarim blocks at

800−750 Ma based on geochronology and geochemistry on samples recovered from a deep well that reached a depth of >7000 m from the basement of the central Tarim basin.

INTRODUCTION

Although more than a dozen of Precambrian blueschist occurrences in the world have been reported (summarized by Liou et al. 1990), many of them have been shown to represent younger events. Only three Precambrian terranes may have experienced blueschist facies metamorphism in the Precambrian. The first one lies in the Western Africa along the Pan-Africa orogen, with the best documented area in northern Mali, where coesite inclusions were found in omphacite in an impure marble (Caby 1994). The estimated metamorphic condition is about 700−750°C and >27 GPa, representing eclogite facies and not a blueschist facices conditions. The peak metamorphic time was constrained by Rb-Sr and Sm-Nd mineral isochron age of about 620 Ma (Jahn et al. 2001). The evidence of a blueschist event is based solely on old reports of glaucophanitic amphiboles in the terrane (Kaiser 1926; Kröner 1974). However, Frimmel and Hartnady (1992) showed that these blue amphiboles are either magnesio-riebeckite or variable edenite, pargasite to barroisite composition. As a result, this proposed blueschist occurrence must be regarded as equivocal.

The second Precambrian blueschist terrane occurs along the Neo-Proterozoic Jiangnan belt of southeast China, where aragonite + jadeite + glaucophane schist and

schistose lawsonite marble have been described (Zhou 1989). The glaucophane schist was dated at 930 ± 34 Ma with a mineral Sm-Nd isochron (Xu and Qiao 1989), 866 ± 14 Ma for two K-Ar ages on glaucophane (Shu et al. 1994), and 901 ± 19 Ma for $^{40}Ar/^{39}Ar$ for the blue amphibole from the same area (Xu et al. 1992). The third occurrence, the best documented Precambrian blueschist terrane is near Aksu, in the northwest margin of the Tarim craton, western China. This terrane was described by Xiong and Wang (1986), Liou et al. (1989), Nakajima et al. (1990) and Liou et al. (1996), and it is the basis of the present study.

The 15×40 km Aksu Group is mainly composed of pelitic, psammitic, mafic, quartzose schists and lack of melange (Nakajima et al. 1990). The pelitic schist consisting of phengite, quartz, chlorite and albite, is commonly interlayered with quartz schist on a millimeter to centimeter scale, indicating frequent change of protoliths from mudstone to quartzose sandstone (Liou et al. 1996). The major minerals in the psammitic schist are quartz and feldspar. The mafic schist contains mainly Na-amphibole in the southern part whereas both winchite and Na-amphibole are found in the northern part. The typical mineral assemblage for the mafic schist is Na-amphibole (or winchite) + epidote + chlorite + albite + quartz ± actinolite (Nakajima et al. 1990). The peak metamorphic condition of Aksu blueschist terrane was suggested to be 4−6 kbar and 300−400°C based on mineral parageneses and composition of Na-amphibole (Liou et al. 1989). However, the peak metamorphic pressure was later suggested to be higher by Zhang et al. (1999). They described deerite assemblages in association with the Aksu blueschists and used

phase equilibria for deerite yielding greater than 10 kbar in the temperature range of 300−400°C. They inferred a cold geothermal gradient of 10°C/km, similar to that has been estimated for jadeite-quartz blueschists elsewhere.

Two distinct deformation episodes were recognized by Liou et al. (1989) for the Aksu blueschist terrane. The first episode D1, which was contemporaneous with the blueschist facies recrystallization, produced the predominant foliations and lineations in all rock types. The second episode D2, which was after the peak metamorphism, produced the map-scale NE-SW oriented folding. A series of subparallel Precambrian dikes that intruded the Aksu terrane after peak metamorphism were also documented by Liou et al. (1996).

The first evidence for the Precambrian age of the Aksu blueschist terrane comes from stratigraphy. Xiong and Wang (1986) concluded that the Aksu blueschist terrane is structurally coherent, lacks melange, and is unconformably overlain by Late Proterozoic age Sinian formations along its southern boundary. The age of these unbroken, unmetamorphosed Sinian rocks were considered to range from early to late Sinian based on paleontology and correlation with Late Proterozoic sections elsewhere (Gao et al. 1985). Geochronological studies by Nakajima et al. (1991) and Liou et al. (1996) supported the Precambrian age of the Aksu blueschist terrane. Two mica-schist samples were used by Nakajima et al. (1991) to determine the age using K-Ar and whole rock − phengite isochron Rb-Sr methods. The ages vary from 698 ± 26 Ma to 718 ± 22 Ma. A $^{40}Ar/^{39}Ar$ plateau age of 754 Ma was given by Liou et al. (1996) using the step-heating

technique to analyze the Na-amphibole, although the error of the plateau age was not given. Combining these two studies, the blueschist metamorphism of the Aksu terrane were concluded to occur at 700 to 750 Ma. The purpose of this study is to more precisely constrain the metamorphic time of Aksu blueschist terrane by applying the step-heating $^{40}Ar/^{39}Ar$ dating method on the separated phengite grains from three metapelite samples.

GEOCHEMISTRY

The main minerals for the three metapelites of Aksu Precambrian blueschist terrain are phengite, chlorite, quartz, calcite, albite, apatite, zircon, rutile and/or sphene. The chemical compositions of phengite and chlorite of all the three samples as well as the chemical composition of apatite of sample B-001 were analyzed with the electron microprobe (EMP). A Cameca SX-100 at the University of Michigan was used to perform such analyses. For phengite and chlorite analyses, the column conditions were: accelerating voltage 15 kV, beam current 4 nA, beam scan area 2×5 μm^2, peak counting time 10 s and background counting time 5 s. Topaz (F), synthetic plagioclase (Na, Si, Ca), pyroxene (Mg), zoisite (Al), synthetic alforsite (Cl, Ba), K-feldspar (K), synthetic geikielite (Ti), synthetic V_2O_5 (V), synthetic uvarovite (Cr), rhodonite (Mn) and synthetic $FeSiO_3$ (Fe) were used as the standards. The EMP results of phengite and chlorite are given in Table B1, respectively. For apatite analyses, the column conditions were: accelerating voltage 15 kV, beam current 4 nA, beam size 10 μm, peak counting time 10 s and background counting time 5 s. The standards used for the EMP analyses are Topaz

Mountain topaz (F), Tiburon albite (Na), synthetic $ScPO_4$ (P), alforsite (Cl), celestite (S, Sr), wollastonite (Ca), hematite (Fe), synthetic $CePO_4$ (Ce), synthetic $NdPO_4$ (Nd) and synthetic $LaPO_4$ (La). The EMP results of apatite are given in Table B2.

$^{40}Ar/^{39}Ar$ CHRONOLOGY

Three samples of pelitic schist from Aksu Precambrian blueschist terrane were selected for $^{40}Ar/^{39}Ar$ dating. The samples were first broken down with a jaw crusher and then separated with a 180 μm size sieve. After being washed with de-ionized water, the samples smaller than 180 μm were segregated with a magnetic separator and pure phengite particles were further handpicked under a binocular microscope. For each sample, about 5−16 mg phengite grains were wrapped in pure Al foil and placed in evacuated quartz tubes and sent for irradiation in the McMaster Nuclear Reactor at McMaster University in Hamilton, Ontario, Canada. The neutron flux gradient (*J*) was monitored using the MMhb-1 standard whose age (520.4 Ma) was determined previously (Samson and Alexander 1987).

The samples were unpacked after irradiation and loaded into 2 mm diameter wells in a copper disk. Absorbed atmospheric argon was removed by baking the samples at ~150°C over night before putting into the VG1200S mass spectrometer at university of Michigan to measure the argon isotopes. Each sample was individually step heated by an automated argon-ion laser extraction system until complete fusion was achieved. Each

step consisted of 60 s heating followed by 120 s gas cleanup using a liquid N_2 cold finger and two SAES 10 liters per second getters (alloy ST101). Fusion-system blanks were run after every five steps and corrected for all gas fractions. The blank levels were typically 8×10^{-19}, 2×10^{-18}, 2×10^{-19}, 8×10^{-19}, 1×10^{-16} mol for masses 36 through 40, respectively. Corrections due to interfering nucleogenic reactions as well as ^{37}Ar and ^{39}Ar decay were also applied to the data.

RESULTS

The age spectra and volumes of gas released from each sample are given by Fig. B1. Duplicate runs were analyzed for each sample to assess sample variability and the reproducibility of the results. Among the six analyses for the three samples, five yielded a $^{40}Ar/^{39}Ar$ plateau age (Fig. B1). The criteria used to determine whether an analysis yielded a plateau age are: (1) Plateau spectra represent >50% of the ^{39}Ar released in at least five consecutive heating steps. (2) Plateau spectra pass a chi-squared test of the squared weighted deviations from the weighted average age (McDougall and Harrison 1999). The plateau ages are calculated as the inverse variance weighted mean of the ages from the steps which comprise the plateau. The errors for the plateau are reported as 1σ, which is derived from the weighted errors of individual steps. A complete analytical data set and the inverse isochron diagrams are also given in Table B3 and Fig. B1. Due to the old ages of these samples, virtually all the points were plotted on the pure radiogenic axis, so little information about initial argon in these samples can be derived from these

inverse isochron diagrams.

DISCUSSION

The difference between the total gas age and the plateau age is within the 1σ error for the five analyses that yielded plateau ages. For sample A-012, the plateau age was given as 740.7 ± 2.5 Ma, whereas the total gas ages were given as 737.3 ± 2.4 Ma and 739.3 ± 2.4 Ma. For sample B-001 and A-014 that yielded both a plateau age and a total gas age in each analysis, slightly older ages in the range of 748−757 Ma were calculated. The ages yielded by duplicate analyses for each sample are the same within the 1σ error range, suggesting small grain variance and good reproducibility.

Nakajima et al. (1990) applied the K-Ar method to analyze two phengite samples from the Aksu blueschist terrane that yielded 718 ± 22 Ma and 710 ± 21 Ma. Their ages are ~20−40 Ma younger than both the $^{40}Ar/^{39}Ar$ plateau ages and total gas ages yielded in this study, although the total gas ages of $^{40}Ar/^{39}Ar$ method should be similar with the K-Ar age. Nakajima et al. (1990) also reported two phengite-whole rock Rb-Sr isochron ages (698 ± 26 and714 ± 24 Ma) that are similar to the K-Ar ages and much younger than the $^{40}Ar/^{39}Ar$ plateau ages of this study. Considering the large uncertainties of the ages reported in their study, the $^{40}Ar/^{39}Ar$ ages yielded in this study are much better in terms of precision. On the other hand, the $^{40}Ar/^{39}Ar$ ages reported in this study are consistent with the K-Ar ages and Rb-Sr ages by Nakajima et al. (1990) within the 2σ error, and the $^{40}Ar/^{39}Ar$ ages of sample A-012 are even in good agreement with their study within the

1σ error region. Liou et al. (1996) reported a $^{40}Ar/^{39}Ar$ plateau age of 754 Ma by analyzing the separated Na-amphibole (crossite) from the Aksu blueschist terrane. Although not given in their study, the uncertainty of the plateau age should be at least 50 Ma based on the shape of their plateau spectrum. The very low level of K substituted in glaucophane, crosstie and riebeckite indicates a potential problem with Ar ages on these minerals. The Ar is unsupported by K in the amphiboles and is likely derived either from fluid inclusions or solid phengite inclusions in most studies. Nonetheless the reported $^{40}Ar/^{39}Ar$ plateau age of Liou et al. (1996) is in agreement with the results of this study.

Excess argon has been well documented in phengite from HP and UHP rocks (e.g. Tilton et al. 1989; Li et al. 1994; Ruffet et al. 1995; Scaillet 1996; Boundy et al. 1997; Jahn et al. 2001; Sherlock and Kelley 2002; de Jong 2003). It only becomes apparent when phengite samples from the same location yielded considerably different $^{40}Ar/^{39}Ar$ ages or the $^{40}Ar/^{39}Ar$ ages significantly exceed Rb-Sr or Sm-Nd ages in the same samples. Boundy et al. (1997) identified domains of apparently old phengite in samples that contained high Na that may correspond to small paragonite domains that would provide access to excess ^{40}Ar. The problem of excess argon is difficult to evaluate when the difference between $^{40}Ar/^{39}Ar$ ages and Rb-Sr ages is small or the Rb-Sr ages are absent in the same samples. The $^{40}Ar/^{39}Ar$ ages reported in this study belong to the latter case. All the three samples yielded consistent $^{40}Ar/^{39}Ar$ plateau ages in the range of 740−760 Ma, and these ages are concordant with less precise Rb-Sr mineral isochron (Nakajima et al. 1990) within analytical error. Therefore, the excess argon, if any, doesn't seem to have

had much influence on the $^{40}Ar/^{39}Ar$ ages in this study.

Previous studies showed that the peak metamorphic temperature of Aksu blueschist terrane was about 300−400°C (Liou et al. 1989; Zhang et al. 1999), which is in the range of estimated closure temperature of the K-Ar system in muscovite: 350°C. Therefore, the yielded $^{40}Ar/^{39}Ar$ plateau ages in this study, which are in the range of 740−760 Ma, represent approximately last crystallization of the phengite, which is interpreted as the timing of peak metamorphism.

Liou et al. (1996) speculated that Aksu blueschist terrane may represent a remnant suture between the Tarim craton in the south and an unknown craton to the north. Guo et al. (2005) also proposed an Precambrian suture along the Aksu region, which represents the collision zone between North and South Tarim blocks at 800−750 Ma based on the geochronology and geochemistry studies on samples recovered from a deep well that reached a depth of >7000 m from the basement of the central Tarim basin. The $^{40}Ar/^{39}Ar$ plateau ages (740−760 Ma) yielded in this study fit reasonably well with the proposed tectonic sceneries of Tarim basin by Guo et al. (2005).

ACKNOWLEDGMENTS

The author is grateful to L Zhang of Peking University for providing the three metapelite samples used in this study. He also thanks A Andronikov and A Duvall for their help in mineral separation and C Hall for $^{40}Ar/^{39}Ar$ data analysis.

Table B1 Average compositions of phengite and chlorite

	phengite			chlorite		
Sample	B-001	A-012	A-014	B-001	A-012	A-014
SiO_2	48.67	48.55	49.65	25.19	24.62	24.77
TiO_2	0.09	0.14	0.14	0.03	0.04	0.05
Al_2O_3	30.53	30.69	28.04	21.68	21.73	20.37
Cr_2O_3	0.02	0.01	0.02	0.01	0.02	0.01
V_2O_3	0.03	0.02	0.01	0.02	0.02	0.01
FeO	1.70	1.93	3.17	25.24	28.46	30.12
MnO	0.11	0.03	0.06	1.12	0.49	0.88
MgO	2.18	1.99	2.42	13.15	11.06	9.75
BaO	0.24	0.18	0.21	0.02	0.03	0.02
CaO	0.02	0.01	0.01	0.02	0.02	0.04
Na_2O	0.37	0.36	0.17	0.01	0.02	0.03
K_2O	11.11	10.76	11.47	0.04	0.09	0.08
F	0.41	0.29	0.29	0.15	0.11	0.12
Cl	0.01	0.01	0.01	0.02	0.01	0.01
Total	95.49	94.97	95.68	86.70	86.71	86.27
Atom site distribution (12 tetrahedral and octahedral cations for phengite and 10 for chlorite basis)						
Si	6.52	6.51	6.68	2.72	2.71	2.77
Al^{IV}	1.48	1.49	1.32	1.28	1.29	1.23
Al^{VI}	3.35	3.36	3.13	1.49	1.52	1.46
Ti	0.01	0.01	0.01	0.00	0.00	0.00
Cr	0.00	0.00	0.00	0.00	0.00	0.00
V	0.00	0.00	0.00	0.00	0.00	0.00
Fe	0.19	0.22	0.36	2.28	2.62	2.82
Mn	0.01	0.00	0.01	0.10	0.05	0.08
Mg	0.44	0.40	0.49	2.12	1.81	1.63
Ba	0.01	0.01	0.01	0.00	0.00	0.00
Ca	0.00	0.00	0.00	0.00	0.00	0.01
Na	0.10	0.09	0.04	0.00	0.00	0.01
K	1.90	1.84	1.97	0.00	0.01	0.01
A site	2.00	1.94	2.01			
F	0.17	0.12	0.12	0.05	0.04	0.04
Cl	0.00	0.00	0.00	0.00	0.00	0.00

Table B2 Typical composition of apatite from Aksu blueschist terrane*

F	Na_2O	P_2O_5	Cl	SO_2	CaO	MnO	FeO	SrO	Ce_2O_3	Nd_2O_3	La_2O_3	Total
		43.60			53.54							101.45
3.95	0.01	0	0.01	0.01	4	0.06	0.06	0.17	0.01	0.02	0.01	5
Atom site distribution based on 5 large cations												
F	Na	P	Cl	S	Ca	Mn	Fe	Sr	Ce	Nd	La	
1.08	0.00	3.20	0.00	0.00	4.98	0.00	0.00	0.00				
4	2	4	1	1	0	4	4	9	0.001	0.001	0	

* This analysis was mainly intended to detect the Sr concentration in apatite. Major elements and F have not been optimized for element diffusion.

Table B3 Detailed $^{40}Ar/^{39}Ar$ isotope analyses of phengites from Aksu blueschist terrane

e4a A012 mass=1 J= 6.84E-03 ± 2.66E-05 tot.gas.age= 736.261 ± 2.378													
F39	LasPow (mW)	Vol36	Err36	Vol37	Err37	Vol38	Err38	Vol39	Err39	Vol40	Err40	Age(Ma)	AgeErr
0.0004	30	0.09	0.08	(0.58)	0.68	0.06	0.08	1.73	0.09	52.55	0.57	176.90	153.04
0.0028	80	0.40	0.08	3.17	1.07	0.34	0.09	11.64	0.14	541.31	1.01	399.52	20.90
0.0078	125	0.19	0.12	7.81	1.06	0.16	0.08	23.62	0.30	1370.58	1.21	582.02	14.56
0.0193	180	0.10	0.06	22.45	0.71	0.14	0.08	53.81	0.23	3428.91	2.26	647.66	3.71
0.0398	250	0.10	0.05	61.41	2.41	0.15	0.08	96.77	0.38	6513.30	4.95	680.40	2.59
0.0668	300	0.05	0.05	12.46	0.83	0.23	0.06	127.15	0.36	8986.41	1.65	710.11	1.93
0.1537	400	0.04	0.05	16.92	0.92	0.56	0.08	409.82	0.92	29996.58	9.22	731.68	1.40
0.2615	500	0.00	0.07	7.62	1.19	0.49	0.08	508.14	0.97	37645.45	9.71	739.25	1.21
0.3463	600	0.08	0.05	0.29	0.89	0.32	0.14	399.96	0.77	29654.44	5.88	739.23	1.22
0.4348	700	0.10	0.07	0.66	0.92	0.32	0.08	416.87	0.60	30929.42	9.14	739.58	0.97
0.5078	800	0.04	0.06	(0.84)	0.73	0.29	0.12	344.06	0.71	25513.86	8.96	739.59	1.34
0.6019	1000	0.18	0.10	(0.01)	0.74	0.55	0.08	443.73	0.70	33126.96	9.90	742.93	1.12
0.7129	1200	0.14	0.08	(0.20)	0.72	0.53	0.15	523.30	0.71	39095.73	10.67	743.74	0.92
0.8456	1600	0.14	0.07	(0.40)	0.77	0.38	0.17	625.32	0.51	46644.05	12.24	742.86	0.59
0.9615	2000	0.08	0.08	0.84	0.80	0.41	0.13	546.69	1.30	41015.98	6.86	746.58	1.50
0.9833	2500	0.03	0.05	0.96	1.04	(0.01)	0.07	102.63	0.27	7677.70	2.34	744.47	2.04
1.0000	3000	0.04	0.07	0.27	1.05	0.03	0.03	78.71	0.33	5849.76	2.94	739.93	3.43
e4b A012 mass=1J= 6.84E-03 ± 2.66E-05tot.gas.age= 739.373 ± 2.435													
F39	LasPow (mW)	Vol36	Err36	Vol37	Err37	Vol38	Err38	Vol39	Err39	Vol40	Err40	Age(Ma)	AgeErr
0.0002	30	(0.08)	0.09	2.06	1.12	0.33	0.11	0.44	0.08	7.41	1.25	707.49	487.86
0.0011	80	0.02	0.11	1.22	1.23	0.16	0.06	2.22	0.09	90.67	1.09	413.38	141.87
0.0029	125	(0.07)	0.08	(0.14)	1.23	0.16	0.07	4.27	0.12	227.37	1.11	600.76	49.62
0.0084	180	(0.09)	0.09	2.91	1.04	0.17	0.09	13.37	0.19	828.25	1.41	655.14	19.66

0.0197	250	(0.02)	0.08	9.23	1.11	0.18	0.09	27.45	0.25	1901.55	2.36	701.68	9.03
0.0311	300	(0.04)	0.05	3.35	0.61	0.20	0.08	27.51	0.17	1966.56	2.71	721.82	5.58
0.0610	400	0.13	0.13	16.64	0.62	0.10	0.09	72.30	0.22	5239.41	2.29	721.68	4.76
0.2002	500	(0.05)	0.12	14.52	0.99	0.63	0.11	336.91	0.76	25149.94	5.01	744.23	1.62
0.2710	600	0.04	0.07	42.41	1.30	0.33	0.10	171.41	0.69	12695.87	3.93	738.60	2.62
0.3421	700	(0.03)	0.04	3.17	0.82	0.07	0.07	172.05	0.24	12838.22	3.53	744.11	1.02
0.4133	800	0.01	0.07	(0.45)	0.83	0.09	0.08	172.29	0.45	12762.90	6.25	739.02	1.87
0.4892	1000	0.00	0.10	3.42	1.18	0.05	0.06	183.73	0.47	13550.80	3.70	736.48	2.06
0.6219	1200	0.22	0.10	9.76	0.96	0.29	0.11	321.02	0.71	23900.47	8.58	740.58	1.56
0.7597	1600	0.04	0.10	10.85	0.86	0.17	0.08	333.42	0.33	24790.16	7.46	741.12	0.96
0.9887	2000	0.14	0.08	4.24	0.97	0.47	0.13	554.20	1.16	41311.39	4.79	742.37	1.32
0.9977	2500	(0.23)	0.09	(0.52)	1.07	0.13	0.09	21.81	0.16	1606.65	2.23	760.96	10.74
1.0000	3000	(0.11)	0.10	1.20	1.00	0.22	0.08	5.53	0.14	412.48	1.25	791.63	43.78

e5a B001mass=1J= 6.81E-03 ± 2.70E-05tot.gas.age= 747.976 ± 3.278

F39	LasPow (mW)	Vol36	Err36	Vol37	Err37	Vol38	Err38	Vol39	Err39	Vol40	Err40	Age(Ma)	AgeErr
0.0004	30	0.01	0.05	0.94	0.81	0.06	0.06	0.14	0.09	1.30	0.57	(111.53)	1378.41
0.0017	80	0.19	0.05	1.04	0.99	0.13	0.07	0.50	0.12	32.51	0.52	(718.23)	565.99
0.0048	125	0.07	0.05	(0.50)	1.05	0.04	0.08	1.16	0.13	72.32	0.56	472.24	136.30
0.0125	180	(0.02)	0.04	0.05	1.05	0.00	0.04	2.85	0.14	221.69	0.55	787.07	47.47
0.0307	250	(0.06)	0.06	(0.11)	0.80	(0.04)	0.04	6.78	0.08	516.60	1.19	776.74	22.42
0.0515	300	(0.01)	0.07	(3.17)	1.17	(0.07)	0.10	7.76	0.14	562.91	0.75	727.73	24.97
0.1650	400	0.06	0.08	(2.93)	0.98	0.03	0.13	42.33	0.25	3173.58	2.69	741.06	5.79
0.2566	500	0.02	0.05	(3.28)	1.33	0.02	0.08	34.18	0.12	2596.05	2.65	750.95	4.33
0.3805	600	(0.05)	0.08	(2.91)	1.10	0.06	0.09	46.22	0.11	3542.48	3.03	760.17	4.29
0.4892	700	(0.13)	0.05	(4.32)	1.27	0.11	0.08	40.55	0.31	3054.52	2.03	754.55	5.65
0.5593	800	(0.02)	0.06	(0.90)	0.79	(0.08)	0.08	26.14	0.28	1986.95	2.22	754.41	8.46
0.6726	1000	0.11	0.06	0.58	0.71	0.02	0.07	42.24	0.30	3220.84	2.63	748.55	5.70

0.7212	1200	0.04	0.05	0.98	0.56	0.05	0.10	18.16	0.22	1387.45	1.80	750.34	9.74
0.7480	1600	0.11	0.09	(0.01)	0.49	0.05	0.07	9.97	0.12	730.38	1.34	702.51	24.03
0.8075	2000	0.09	0.03	(1.09)	0.92	0.02	0.08	22.21	0.32	1726.31	2.11	756.59	9.69
0.9200	2500	0.16	0.11	1.63	1.18	0.07	0.06	41.95	0.15	3183.56	2.33	742.33	6.53
1.0000	3000	0.05	0.08	(1.02)	1.02	(0.02)	0.09	29.84	0.14	2309.56	2.00	759.87	7.25

e5b B001 mass=1J= 6.81E-03 ± 2.70E-05tot.gas.age= 753.019 ± 2.755

F39	LasPow (mW)	Vol36	Err36	Vol37	Err37	Vol38	Err38	Vol39	Err39	Vol40	Err40	Age(Ma)	AgeErr
0.0001	30	0.06	0.07	1.05	1.12	0.09	0.10	0.10	0.09	9.38	0.92	(1351.80)	5625.41
0.0012	80	0.12	0.09	0.56	0.88	0.08	0.05	0.97	0.12	69.36	1.06	373.41	266.97
0.0030	125	(0.04)	0.16	(0.56)	1.15	0.09	0.07	1.70	0.11	108.61	1.23	715.96	237.81
0.0095	180	0.08	0.08	(0.22)	0.69	0.00	0.08	5.94	0.14	390.93	1.31	632.92	36.32
0.0235	250	0.04	0.08	0.48	0.82	0.05	0.07	12.73	0.22	906.22	1.71	705.62	18.39
0.0375	300	0.07	0.08	(1.14)	1.60	0.02	0.09	12.75	0.19	948.42	1.52	726.54	18.24
0.1462	400	(0.12)	0.07	(1.92)	1.25	0.13	0.08	99.21	0.23	7534.75	3.31	755.14	2.30
0.2390	500	0.18	0.06	(3.57)	1.17	0.16	0.09	84.72	0.42	6532.89	3.02	756.59	3.55
0.3250	600	0.20	0.10	(1.33)	1.87	0.11	0.09	78.44	0.44	6015.65	2.86	752.20	4.58
0.4533	700	0.01	0.06	(1.24)	1.45	0.21	0.10	117.10	0.53	8974.97	4.08	757.55	3.07
0.5613	800	0.10	0.07	0.92	1.09	0.17	0.11	98.63	0.19	7558.67	3.90	755.34	2.18
0.6414	1000	0.02	0.09	0.63	1.26	0.21	0.08	73.05	0.33	5561.17	3.16	753.04	4.07
0.7447	1200	(0.11)	0.06	1.06	1.38	0.19	0.08	94.31	0.41	7190.50	5.51	757.23	3.13
0.8437	1600	0.18	0.08	1.89	1.33	0.19	0.09	90.30	0.40	6956.49	3.80	756.24	3.49
0.9449	2000	0.25	0.07	0.58	1.28	0.15	0.07	92.36	0.40	7148.14	2.73	757.50	3.21
0.9968	2500	0.08	0.11	3.73	1.05	(0.14)	0.10	47.35	0.22	3629.68	2.80	753.62	6.13
1.0000	3000	0.17	0.10	0.48	0.95	(0.11)	0.09	2.95	0.13	250.01	0.93	682.03	90.36

e6a A014 mass=1 J= 6.80E-03 ± 2.73E-05 tot.gas.age=753.222 ± 2.549

F39	LasPow (mW)	Vol36	Err36	Vol37	Err37	Vol38	Err38	Vol39	Err39	Vol40	Err40	Age(Ma)	AgeErr
0.0006	30	0.15	0.09	(0.59)	0.84	0.14	0.07	1.74	0.12	56.30	0.46	77.28	171.09

0.0030	80	0.19	0.07	(0.34)	0.84	0.24	0.11	7.48	0.15	386.37	0.95	471.97	27.21
0.0072	125	0.09	0.08	(1.55)	0.71	0.21	0.07	12.89	0.16	846.95	1.20	648.13	17.12
0.0159	180	0.06	0.08	0.58	0.85	0.10	0.07	26.96	0.15	1899.01	2.62	700.49	7.67
0.0301	250	0.07	0.08	(1.42)	1.12	0.04	0.09	43.45	0.29	3192.95	2.91	727.28	6.19
0.0597	300	0.13	0.13	1.24	0.87	(0.08)	0.13	91.26	0.50	6789.07	2.91	734.99	4.83
0.2851	400	0.17	0.13	1.15	1.11	0.75	0.19	693.67	1.67	53144.89	11.70	755.83	1.55
0.4133	500	(0.01)	0.13	(0.28)	0.90	(0.03)	0.17	394.54	0.87	30074.13	9.64	753.35	1.57
0.4372	600	0.07	0.13	0.37	1.00	0.04	0.14	73.54	0.46	5598.12	1.85	750.13	5.71
0.5020	700	(0.05)	0.13	(0.09)	0.87	0.11	0.13	199.21	0.65	15274.22	8.15	757.49	2.56
0.5266	800	(0.19)	0.10	(1.07)	1.10	(0.09)	0.09	75.90	0.21	5749.39	0.94	755.46	3.66
0.6144	1000	0.08	0.14	1.33	0.81	0.12	0.11	269.96	0.58	20584.81	3.81	752.73	1.79
0.6802	1200	(0.02)	0.07	0.40	0.87	0.27	0.09	202.53	0.51	15516.56	6.13	756.63	1.79
0.8868	1600	(0.03)	0.07	5.44	0.89	0.67	0.11	635.82	0.73	48806.70	8.20	757.70	0.77
0.9693	2000	(0.01)	0.06	2.69	0.90	0.09	0.12	253.85	0.75	19490.27	7.26	757.80	1.92
0.9838	2500	(0.08)	0.10	(0.73)	0.63	0.06	0.07	44.74	0.35	3442.26	2.45	763.25	7.21
1.0000	3000	(0.04)	0.10	(0.02)	0.64	0.12	0.08	49.81	0.43	3876.66	3.13	768.02	7.17

e6b A014 mass=1 J= 6.80E-03 ±2.73E-05tot.gas.age= 752.159 ± 2.523

F39	LasPow (mW)	Vol36	Err36	Vol37	Err37	Vol38	Err38	Vol39	Err39	Vol40	Err40	Age(Ma)	AgeErr
0.0004	30	(0.10)	0.11	(0.41)	0.96	0.03	0.06	1.39	0.05	46.03	0.67	564.31	210.84
0.0020	80	0.06	0.10	(1.66)	0.91	0.07	0.07	6.54	0.15	326.90	1.52	501.19	44.07
0.0052	125	(0.19)	0.11	(1.92)	1.13	0.14	0.07	12.77	0.14	796.72	1.98	675.54	22.81
0.0119	180	(0.02)	0.14	(2.52)	1.34	(0.07)	0.07	26.60	0.26	1842.84	1.34	697.92	14.02
0.0240	250	(0.18)	0.11	(0.92)	1.27	(0.03)	0.06	48.14	0.42	3468.96	2.84	728.10	7.64
0.0384	300	0.02	0.11	(0.34)	1.28	0.19	0.09	57.22	0.30	4262.09	3.52	738.20	5.54
0.1312	400	(0.16)	0.11	(0.06)	1.38	0.45	0.12	369.39	0.90	28102.84	5.26	753.12	1.65
0.2085	500	(0.03)	0.11	(0.28)	1.14	0.55	0.12	308.04	0.71	23517.39	7.63	754.46	1.69

0.3660	600	0.03	0.10	(0.68)	1.65	0.72	0.15	626.94	1.21	47860.78	12.10	754.10	1.26
0.4708	700	0.08	0.12	3.05	1.10	0.79	0.15	416.94	0.70	31805.11	10.58	753.25	1.25
0.5670	800	0.27	0.10	2.68	0.68	0.19	0.15	382.93	0.86	29172.53	7.08	751.27	1.51
0.6867	1000	0.30	0.07	5.02	1.05	0.77	0.15	476.34	0.98	36498.39	9.29	755.00	1.33
0.7898	1200	0.05	0.05	3.55	0.86	0.36	0.13	410.67	0.88	31300.74	7.68	752.93	1.36
0.8997	1600	0.26	0.08	8.23	0.53	0.47	0.19	437.17	0.94	33527.77	7.63	755.63	1.41
0.9705	2000	0.31	0.08	2.68	0.81	0.34	0.11	282.18	0.84	21559.29	4.75	752.11	1.95
0.9841	2500	(0.00)	0.10	(0.18)	0.84	0.00	0.08	53.75	0.31	4111.91	2.83	755.66	5.82
1.0680	1992	0.04	0.05	(3.02)	0.64	0.33	164.39	490.86	1.20	36738.20	9.35	860.46	(19.10)

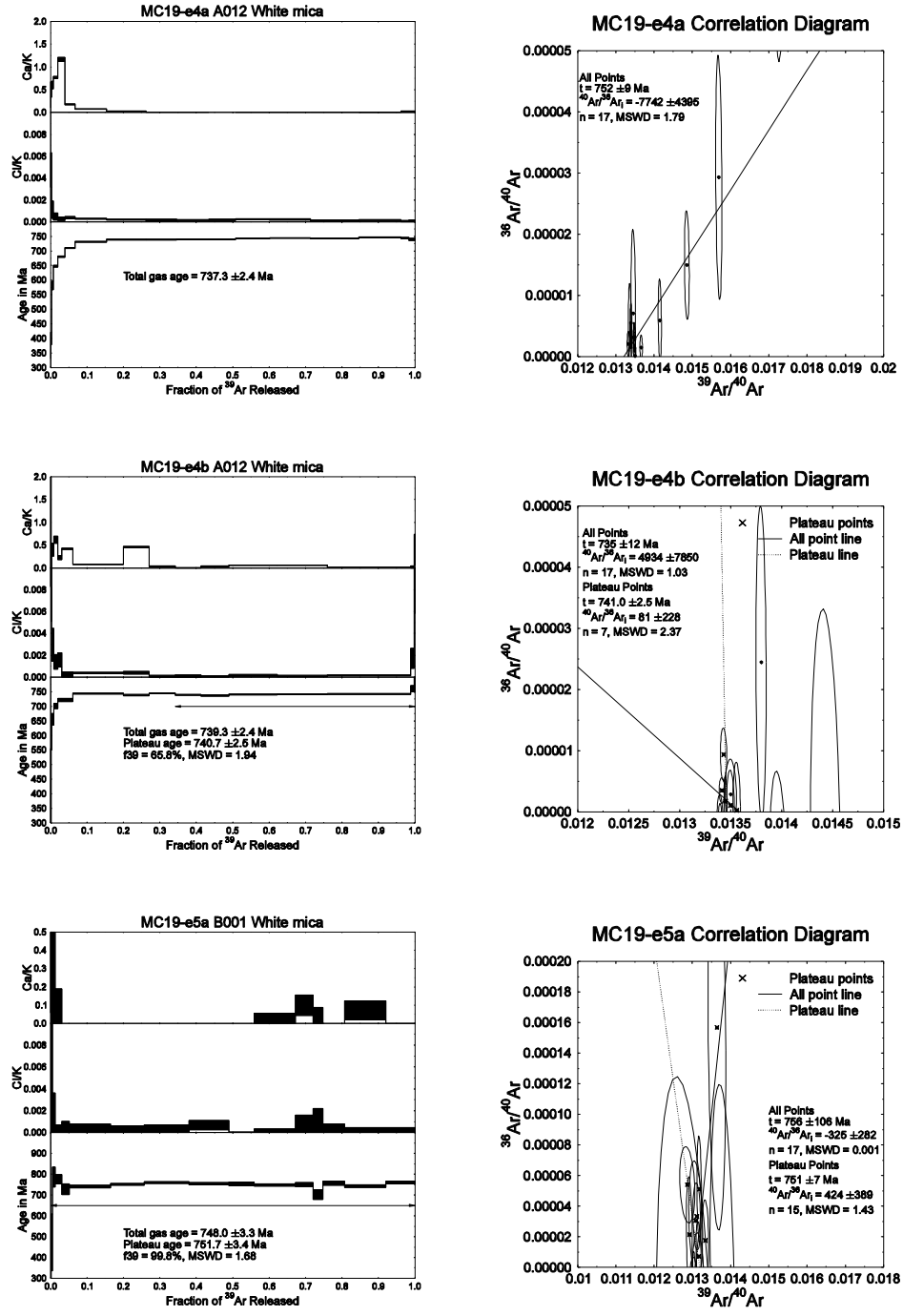

Fig. B1 Total gas and plateau spectra (left column) and inverse isochron diagrams (right column) for the Aksu blueschist samples.

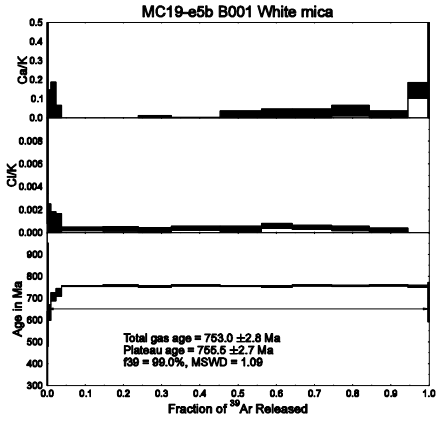

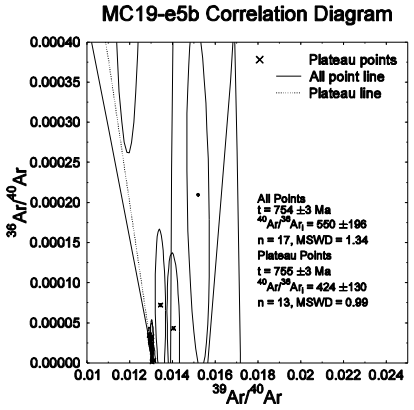

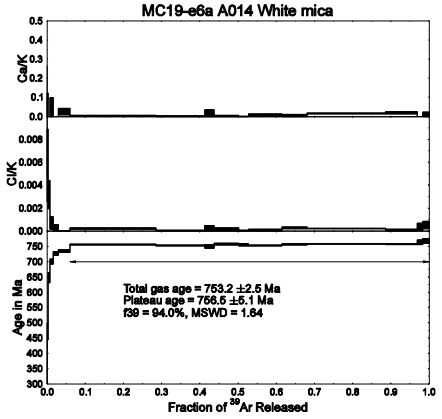

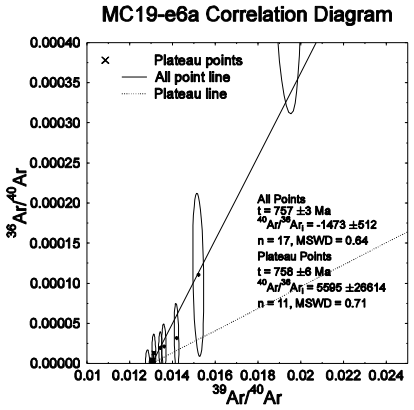

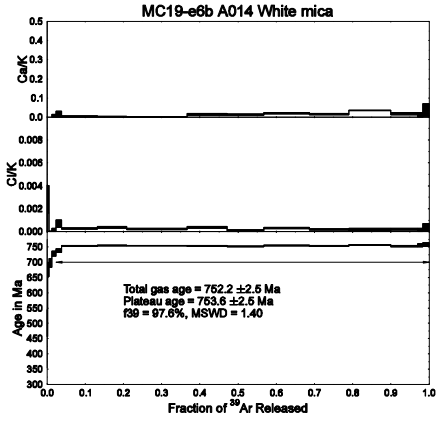

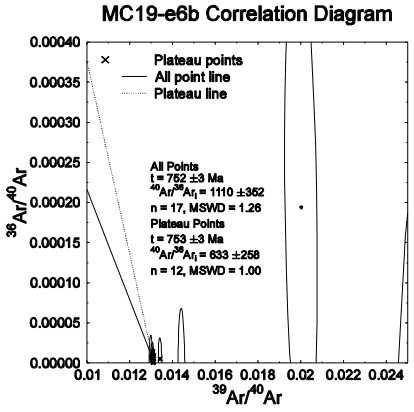

Fig. B1. Continued.

REFERENCES

Boundy TM, Hall CM, Essene EJ, Halliday AN, Peacor DR (1997) Fine-scale fluid distribution in the deep crust: a combined ^{40}Ar-^{39}Ar laser ablation and TEM study of single muscovites from a granulite-eclogite transition zone. Earth Planet Sci Lett 148:223-242.

Caby R (1994) Precambrian coesite from northern Mali: first record and implications for plate tectonics in the trans-Sahara segment of the Pan-African belt. Eur J Mineral 6:235−244

de Jong K (2003) Very fast exhumation of high-pressure metamorphic rocks with excess ^{40}Ar and inherited ^{87}Sr, Betic Cordilleras, southern Spain. Lithos 70:91−110

Frimmel HE, Hartnady JH (1992) Blue amphiboles and their significance for the metamorphic history of the Pan-African Gariep belt, Namibia. J Metamorph Geol 10:651−669

Gao Z, Wang W, Peng C, Li Y, Xiao B (1985) The Sinian system of Aksu-Wusi region, Xinjiang, China. Xinjiang Bureau of Geology and Mineral Resources, 184 pp (in Chinese, with English abstract)

Guo Z, Yin A, Robinson A, Jia C (2005) Geochronology and geochemistry of deep-drill-core samples from the basement of the central Tarim basin. J Asian Earth Sci 25:45−56

Jahn B, Caby R, Monie P (2001) The oldest UHP eclogites of the world: age of UHP metamorphism, nature of protoliths and tectonic implications. Chem Geol

178:143−158

Kaiser E (1926) Die Diamantenwüste Südwestafrikas. Band I. Dietrich Reimer, Berlin. pp 190−204

Kröner A (1974) The Gariep Group I. Late Precambrian formations in the western Richtersveld, Northern Capa Province. Precambrian Research Unit, University of Cape Town, Bulletin, 13, 115 pp

Li S, Wang S, Chen Y, Zhou H, Zhang Z, Liou D, Qiou J (1994) Excess argon in phengite of eclogite: evidence from dating of eclogite minerals by Sm-Nd, Rb-Sr and $^{40}Ar/^{39}Ar$ isotope methods. Chem Geol 112:343−350

Liou JG, Graham SA, Maruyama S, Wang X, Xiao X, Carroll AR, Chu J, Feng Y, Hendrix MS, Liang YH, Mcknight CL, Tang Y, Wang ZX, Zhao M, Zhu B (1989) Proterozoic blueschist belt in western China: best documented Precambrian blueschists in the world. Geology 17:1127−1131

Liou JG, Graham SA, Maruyama S, Zhang RY (1996) Characteristics and tectonic significance of the late Proterozoic Aksu blueschists and diabasic dikes, northwest Xinjiang, China. Int Geol Rev 38:228−244

Liou JG, Maruyama S, Wang X, Graham SA (1990) Precambrian blueschist terranes of the world. Tectonophysics 181:97−111

McDougall L, Harrison TM (1999) Geochronology and thermochronology by the $^{40}Ar/^{39}Ar$ method. Oxford University Press, Oxford, 269 pp

Nakajima T, Maruyama S, Uchiumi S, Liou JG, Wang X, Xiao X, Graham SA (1991) The

age of the oldest blueschist of the world−the Aksu Group of western China. Nature 346:263−265

Ruffét G, Féraud G, Balevre M, Kienast JR (1995) Plateau ages and excess argon in phengites: an $^{40}Ar/^{39}Ar$ laser probe study of Alpine micas (Sesia Zone, Western Alps, northern Italy). Chem Geol 121:327−343

Samson SD, Alexander EC (1987) Calibration of the interlaboratory $^{40}Ar/^{39}Ar$ dating standard, Mmhb-1. Chem Geol 66:27−34

Scaillet S (1996) Excess ^{40}Ar transport scale and mechanism in high-pressure phengites: a case study from an eclogitised metabasite of the Dora-Maira nappe, western Alps. Geochim Cosmochim Acta 60:1075−1090

Sherlock S, Kelley S (2002) Excess argon evolution in HP-LT rocks: a UVLAMP study of phengite and K-free minerals, NW Turkey. Chem Geol 182:619−636

Shu L, Zhou G, Shi Y, Yin J (1994) Study of the high pressure metamorphic blueschist and its late Proterozoic age in the eastern Jiangnan belt. Chin Sci Bull 39:1200−1204

Tilton GR, Schreyer W, Schertl HP (1991) Pb-Sr-Nd isotopic behavior of deeply subducted crustal rocks from the Dora-Maira Massif, Western Alps, Italy: II. What is the age of the ultrahigh-pressure metamorphism? Contrib Mineral Petrol 108:22−33

Xiong J, Wang W (1986) Preliminary research on Aksu Group of the pre-Sinian. Xinjiang Geology 4:33−46

Xu B, Guo L, Shi Y (1992) Proterozoic terranes and multiphase collision orogens in Anhui-zhejiang-Jiangxi areas. Geological Publishing House, Beijing, 112 pp (in Chinese, with English abstract)

Xu B, Qiao G (1989) Sm-Nd isotopic age and tectonic setting of the Late Proterozoic ophiolites in Northeastern Jiangxi Province. J Nanjing Univ 3:108−114 (in Chinese, with English abstract)

Zhang L, Jiang W, Wei C, Dong S (1999) Discovery of deerite from the Aksu Precambrian blueschist terrane and its geological significance. Sci China Ser D 42:233−239

Zhou G (1989) The discovery and significance of the northeastern Jiangxi Province ophiolite (NEJXO), its metamorphic peridotite and associated high temperature−high pressure metamorphic rocks. J SE Asian Earth 3:237−247